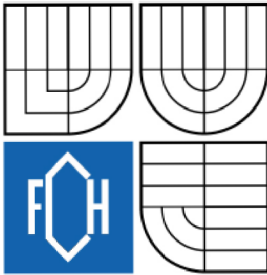


VYSOKÉ UČENÍ TECHNICKÉ V BRNĚ
BRNO UNIVERSITY OF TECHNOLOGY



FAKULTA CHEMICKÁ
ÚSTAV CHEMIE MATERIÁLŮ
FACULTY OF CHEMISTRY
INSTITUTE OF MATERIALS SCIENCE

PROCESSING AND MARTENSITIC TRANSFORMATIONS OF NiTi-BASED ALLOYS

PŘÍPRAVA A MARTENZITICKÉ TRANSFORMACE SLITIN NA BÁZI NiTi

DIZERTAČNÍ PRÁCE

PHD THESIS

AUTOR PRÁCE: Ing. MONIKA KUBĚNOVÁ

AUTHOR

VEDOUCÍ PRÁCE: prof. RNDr. ANTONÍN DLOUHÝ, CSc.

SUPERVISOR

BRNO 2014

ABSTRACT

The thesis aims at: (i) an assessment of alloy contamination which may result from vacuum induction melting of Ni-rich NiTi-based shape memory alloys in conventional porous Y_2O_3 crucibles. (ii) an optimization of NiTi melting conditions with respect to the alloy purity and cost efficiency. (iii) an obtaining new differential scanning calorimetry (DSC) and 3D atom probe (AP) data on martensitic transformations and related hydrogen distributions in the Ni-rich NiTi shape memory alloys subjected to heat treatments under controlled environments with systematic variation of the hydrogen partial pressure.

The following experiments were carried out:

- Five different melting routes were designed and carried out in order to decrease melting temperature.
- Five re-melting experiments were performed at 1500 °C with holding time 2, 10 and 20 min, and at 1550 °C and 1450 °C with 20 min holding time to examine the effect of temperature and holding time on oxygen content.
- Ni-rich NiTi alloys were heat treated in Regime I (annealing) and in Regime II (annealing and aging) in either hydrogen or hydrogen-helium mixture (H_2 partial pressure 20, 100, 500 and 700 mbar). Reference experiment were also performed in a pure helium atmosphere.

It was found that designed melting routes lead to the lowering of maximum temperature during the induction melting cycles from 1800 to 1400 °C. Despite this significant maximum temperature drop, oxygen content of the final solidified alloy does not markedly reduce. During re-melting at 1500 °C with 2 min of holding time, the content of oxygen becomes triple the initial oxygen level and does not too differ from the re-melting experiments carried out at the same melting temperature but with 10 min of holding time. Furthermore, the oxygen content increases about fourfold with respect to the initial oxygen level during re-melting for 20 min at 1450 °C. This contamination level does not vary markedly with further rise of the melting temperature by 100 °C. Heat treatments in the controlled gaseous environments revealed that the one-step B2-B19' martensitic transformation ceases with the increasing partial pressure of hydrogen. A pronounced drop in the DSC peak heights occurs at the hydrogen partial pressure exceeding 100 mbar. 3D AP measurements showed that there are no local variations in the Ni and Ti compositions in the sample after the Regime I heat treatment in hydrogen. Hydrogen was found to form stable interstitial solid solution in B2 NiTi. The distribution of hydrogen atoms is inhomogeneous; they organize into nano-domains with the hydrogen content exceeding locally a level of 10 at%.

KEYWORDS

Ni-rich NiTi Alloys, Martensitic Transformations, Differential Scanning Calorimetry, Induction Melting and Heat Treatment under Controlled Atmosphere.

ABSTRAKT

Cíle této práce jsou: (i) vyhodnocení vlivu Y_2O_3 kelímku na kontaminaci indukčně tavené NiTi slitiny obohacené niklem, (ii) optimalizace podmínek, při kterých jsou tavby uskutečněny a (iii) získání nových DSC a 3D AP dat o vlivu vodíkové atmosféry na martenzitickou transformaci a na strukturu NiTi slitin obohacené niklem s tvarovou pamětí. Byly provedeny následující experimenty:

- Pět taveb bylo navrženo a provedeno tak, aby byla snížena maximální tavící teplota.
- Pět přetaveb bylo uskutečněno při teplotě $1500\text{ }^\circ\text{C}$ s dobou výdrže 2, 10 a 20 minut a při teplotách $1450\text{ }^\circ\text{C}$ a $1550\text{ }^\circ\text{C}$ s 20 minutovou dobou výdrže. Experiment byl navržen tak, aby byl vyšetřen vliv tavící teploty a doby výdrže na obsah kyslíku pocházejícího z kelímku Y_2O_3 v tavenině.
- Tepelné zpracování NiTi slitiny obohacené niklem v režimu I (žihání) a v režimu II (kombinace žihání se stárnutím) pod atmosférou vodíku, směsi vodíku s héliem a pod referenční atmosférou čistého hélia.

Získané výsledky jsou:

- Navržené tavící postupy vedou ke snížení maximální tavící teploty a to z $1800\text{ }^\circ\text{C}$ na $1400\text{ }^\circ\text{C}$. Přesto toto velké snížení maximální tavící teploty nevedlo k významnému poklesu obsahu kyslíku.
- Během přetavby uskutečněné při teplotě $1500\text{ }^\circ\text{C}$ s dobou výdrže 2 minuty se obsah kyslíku navýšil o trojnásobek jeho počáteční hodnoty a příliš se nelišil od obsahu kyslíku naměřeného ve slitině, která byla přetavena při stejné teplotě s dobou výdrže 10 minut. K nárustu o čtyřnásobek počáteční hodnoty obsahu kyslíku došlo u přetavby vedené na teplotě $1450\text{ }^\circ\text{C}$ po dobu 20 minut a hodnota obsahu kyslíku se příliš nelišila od hodnoty naměřené ve slitině přetavené při teplotě $1550\text{ }^\circ\text{C}$ se stejnou dobou výdrže.
- S rostoucím parciálním tlakem vodíku dochází k potlačení jednokrokové martenzitické transformace. Významný pokles výšky DSC píku nastává při parciálním tlaku 100 mbar. 3D AP analýza odhalila, že nedochází k žádné lokální změně koncentrace a nebo pozic niklových a titanových atomů ve vzorku, který byl žihán v režimu I ve vodíku. Bylo objeveno, že vodík tvoří stabilní intersticiální tuhý roztok v NiTi B2 mřížce, kde vytváří systém nanodomén s obsahem vodíku vyšší než 10 at%.

KLÍČOVÁ SLOVA

NiTi slitiny obohacené niklem, Martenzitická transformace, Diferenciální skenovací kalorimetrie, Indukční tavení a tepelné zpracování pod řízenou atmosférou.

KUBENOVA, Monika *Processing and martensitic transformations of NiTi-based alloys*: doctoral thesis. Brno: Brno University of Technology, Faculty of Chemistry, Institute of materials science, 2014. 112 s. Supervised by prof. RNDr. Antonin Dlouhy, CSc.

DECLARATION

I declare that the doctoral thesis has been worked out by myself and all the quotations from the used literature sources are accurate and complete. The content of the doctoral thesis is the property of the Faculty of Chemistry of University of Technology and all commercial uses are allowed only if approved by both the supervisor and the dean of the Faculty of Chemistry, VUT.

Brno

.....

(author's signature)

ACKNOWLEDGEMENT

First of all, I would like to thank my supervisor, Prof. Antonín Dlouhý. I cannot think of any supervisor from whom I could have learned as much as I did. He was not only available when I needed counsel regarding the direction of my research, but he was also there when I needed career. I would like to thank Prof. Ladislav Zemčík for carrying out all melting experiments and advise. I would also like to thank doctor Čermák for help in sealing samples into quartz capsules filled in gases. I would like to thank the member of our research group, Jakub Zálešák, for great cooperating and for his friendship. I would like to thank my parents, Marie and Josef Kuběna, I could not have come all the way to this stage in my academic life without their encouragement, support and love. I would like to thank for financial support received from CSF under the contract number 106/09/1913 and from GACR under the number CZ.1.07/2.3.00/20.0214.

Brno

.....

(author's signature)

CONTENTS

1	Introduction	17
1.1	The unique behavior of NiTi alloys	17
1.2	The outline of this work	17
1.3	Reversible martensitic transformations	18
1.3.1	Crystal structures	19
1.4	Crystallographic theory of martensite	20
1.5	Thermodynamics	21
1.6	Physical metallurgy of Ni-Ti alloys	25
1.6.1	Phase diagram	25
1.6.2	Transformation temperatures	26
1.6.3	Melting and casting	28
1.6.4	Heat treatments (decomposition of Ni-rich alloys)	29
1.6.5	Ni ₄ Ti ₃ phase and its effect on sequence of martensitic transformations	31
1.7	Effect of impurities on martensitic transformations	33
1.7.1	Carbon impurities	33
1.7.2	Oxygen impurities	34
1.7.3	Hydrogen impurities	35
1.7.4	Heat treatment environments	36
1.8	The objectives of the thesis	40
2	Experimental techniques	41
2.1	As-received material	41
2.1.1	Induction melting experiments	41
2.1.2	Heat treatments	41
2.2	Vacuum induction melting	42
2.3	Heat treatments under controlled atmospheres	44
2.4	Analytical methods	45
2.4.1	Oxygen analysis	45
2.4.2	Differential scanning calorimetry	45
2.4.3	Scanning electron microscopy	47
2.4.4	Transmission electron microscopy	47
2.4.5	Neutron diffraction measurements	48
2.4.6	3D Atom probe analysis	48

3	Results	53
3.1	Alloys melted in Y_2O_3 crucible	53
3.1.1	Contamination by oxygen	53
3.1.2	$Y_2O_3/ Ni_{50.8}Ti_{49.2}$ interface	59
3.2	Heat treatments in controlled atmospheres	60
3.2.1	Influence of the quenching rate	60
3.2.2	Impact of heat treatments in the Regime I and II on the mar- tensitic transformation	61
3.2.3	Impact of heat treatments in Regime I on microstructure: pre- sence of impurities	66
3.2.4	Impact of heat treatments in Regime II on microstructure: varying size of Ni_4Ti_3 precipitates	71
4	Discussion	73
4.1	Alloys melted in Y_2O_3 crucible	73
4.1.1	Melt-crucible interaction mechanisms	73
4.1.2	Oxygen contamination in a relation to melting temperatures	75
4.2	Heat treatments in controlled atmosphere	78
4.2.1	Material quality	78
4.2.2	Heat treatment in air	82
4.2.3	Hydrogen impact	82
5	Conclusions	87
6	Suggestions for future work	89
	Bibliography	91
	List of symbols, physical constants and abbreviations	101
	List of appendices	105
A	Appendix	107
A.1	DSC analysis	107
B	Appendix	111
B.1	Curriculum Vitae	111

LIST OF FIGURES

1.1	(a) Growth of plates terminated at grain boundaries and at other martensite plates. (b) Surface upheaval due to the plate intersecting the surface of the sample [19].	18
1.2	The observed experimental structures of NiTi: B2 austenite, R-phase and B19' martensite (cubic coordination). Ni and Ti atoms are shown as gray and blue-coded spheres, respectively.	19
1.3	Schematic representation of lattice distortions which provide the experimentally observed orientation relationship between austenite and martensite, and correct macroscopic shape of martensitic plates [18].	20
1.4	Difference in free energy between martensite and austenite close to equilibrium temperature T_0 . The curvature of the G^{B2} and $G^{B19'}$ lines has been ignored [19].	23
1.5	Calculated phase diagram of NiTi binary system, to which the phase equilibrium between B2 and B19' phases is added together with stable phases NiTi ₂ and NiTi ₃ [30].	25
1.6	Relation between nickel content and M_s , or M_p temperatures [35]. . .	26
1.7	The SMA phase diagram of stress and temperature (see text) [38]. . .	27
1.8	Schematic drawing of VIM (a) and VAR (b) process [36].	29
1.9	3D views of the equilibrium shape of an isolated Ni ₄ Ti ₃ precipitate [22] and TEM micrograph showing precipitates of the Ni ₄ Ti ₃ phase.	30
1.10	Stability of B2, R-phase and B19' in binary Ni-rich NiTi alloy (a and c). The presence of obstacles (precipitates and dislocation substructures) makes it energetically more difficult to form B19', while the formation of R-phase is not affected (c) [51]. Schematic DSC charts illustrating one-step transformation (b), one exothermic peak on cooling from the B2 regime and one endothermic peak on heating, and two-step transformation (d), two exothermic peaks on cooling from B2 to R-phase and from R-phase to martensite and one endothermic peak on heating [52].	31

1.11	Schematic illustration of a multiple-step martensitic transformation due to coherency stress fields around precipitates. In the first stage of the transformation sequence (a), B2 transforms into R-phase as R-phase nucleates at the particle/matrix interface and grows into the B2 matrix. In the second step (b), the R-phase transforms into B19'₁. The subsequent growth of B19'₁ is bounded by those region around particles which are affected by coherency stresses. Finally (c), in the third step, those region of the matrix outside the local precipitate coherency stresses are able to transform to B19'₂. The same scenario might be observed even if coherency stresses were not significant, in which case varying Ni concentrations would be responsible [51]. . . .	32
1.12	(a) Different scanning calorimetry (DSC) charts and (b) the dependence of transformation temperature and thermal hysteresis on carbon content (0, 0.2, 0.3 and 0.6) of annealed Ni ₅₀ Ti ₅₀ alloys [55]. . . .	33
1.13	SEM micrographs showing TiC phase in the vacuum induction melted Ni _{50.7} Ti _{49.3} alloy. (a) Hypoeutectic microstructure contains eutectic phase in the NiTi matrix, (b) Eutectic TiC phase with small primary TiC particles, one particle is highlighted by a white arrow [57]. . . .	34
1.14	(a) Bright-field image showing an oxide phase in the Ni _{50.8} Ti _{49.2} alloy prepared by vacuum induction melting using Y ₂ O ₃ crucible. (b) SAD pattern of the oxide phase taken in the zone [101] [59]. Lattice has a cubic structure with space group Fd-3mS. Lattice constant is 1.13279 nm [60].	35
1.15	Schematic illustration of heat treatment conditions A and B of analyzed samples (a) and their corresponding cooling DSC curves (b). The samples were annealed at 1000 °C for 3.6 ks [66].	36
1.16	DSC cooling curves of samples annealed at 1000 °C for 3.6 ks and aged at 500 °C for 7.2 ks in conditions (a) A–B and (b) B–A [66]. . .	37
1.17	Bright field images of G.B. and G.I. regions of the samples aged at 500 °C for 3.6 ks in conditions A–A (a and b), and B–B (c and d) [66].	38
1.18	Schematic illustration of precipitation morphology and sequence of the transformations (a), and DSC charts (b) of the aged Ni _{50.8} Ti _{49.2} alloy heat-treated in condition A. The alloy were annealed at 1000 °C for 3.6ks and aged at 500 °C for 3.6 ks [68].	39
2.1	A schematic drawing of an 128 mm piece spark-cut into 15 mm and 2 mm cylinders.	42
2.2	(a) Conventional porous Y ₂ O ₃ crucible and (b) vacuum induction melting furnace used for re-melting procedure.	43
2.3	A schema of heat treatment sequences of a cylinder (a) and the image of a cylinder sealed into quartz capsules filled with argon (b).	45

2.4	A schematic drawing illustrating positions of samples for oxygen analysis (black squares) and for DSC analysis (red circles) in a ingot (a) and in a re-molten ingot (b). Corresponding dimensions are in mm.	46
2.5	A schematic drawing that illustrates position of DSC samples (red areas) in the heat treated and quenched cylinders. Corresponding dimensions are in mm.	46
2.6	Inside view of the scanning electron microscope Tescan SEM/FEG LYRA 3 XMU with the focus ion (Ga^{3+}) beam, a gas injection system (GIS), a micromanipulator, bellow sample holder and backscattered electron (BSE) detector.	47
2.7	IMAGO LEAP microscope and AP needle-shaped samples.	48
2.8	An anodic sample situated within a gold ring-shape cathode: a) at the beginning and b) at the end of electro-chemical etching process [72].	49
2.9	AP-sample preparation using lift-out technique (see text for details) [71].	49
2.10	Final-shape of a tip (a,b) and inside view of the IMAGO LEAP microscope (c).	50
3.1	The column chart displays the content of oxygen in the cast alloys (see text for details).	53
3.2	The cone shaped ingots of 30 (bottom) and 70 (top) mm in diameter and 180 mm in length. The ingot melting route is given using capital letters.	54
3.3	DSC charts of the cast alloys A and B. Samples taken from different positions along the ingot axis were investigated.	55
3.4	(a,b) Microstructure of the DSC sample taken from an annealed piece (position 5) of ingot B. The images were obtained by means of SEM in BSE contrast mode. (c,d) The detail of a white particle in BSE contrast (c) and in X-ray 'dot' distribution map (d) (yttrium L_{α}).	55
3.5	Macrostructures from the ingots A and B.	56
3.6	(a) The variation of the release latent heat associated with martensitic transformation from $\text{B2} \leftrightarrow \text{B19}'$ in the re-molten alloys with oxygen content at different melting temperatures and holding times. (b) Result of the chemical analysis showing increase of oxygen content in re-molten alloys at 1450, 1500 and 1550 °C after different reaction times.	57
3.7	DSC charts of the supplied and re-molten alloys at different melting temperatures and holding times.	58

3.8	Microstructure of the DSC samples taken from the alloy after re-melting for 2 min at 1500 °C (a) and the supplied alloy (b). (2) The SEM images at higher magnifications show Y ₂ O ₃ (white) and Ti-rich (dark) phases (a2), and a small TiC particle (b2) in NiTi matrix. The images were obtained by means of SEM in BSE contrast mode.	58
3.9	(a) The bottom of Y ₂ O ₃ crucible. (b) Ni _{50.8} Ti _{49.2} block after re-melting for 10 min at 1500 °C in Y ₂ O ₃ crucible, and SEM and SEM back-scatter micrographs of detail of surface of the block containing Y ₂ O ₃ particles.	59
3.10	SEM back-scatter micrographs of the interface region between the Y ₂ O ₃ crucible (white phase below) and the Ni _{50.8} Ti _{49.2} alloy (bright-gray phase above) after re-melting for 20 min at 1450 °C. The dark-gray phase in between represents Ti-rich phase.	60
3.11	DSC charts of the Ni _{50.8} Ti _{49.2} alloys heat treated in Regime I in 900 mbar of hydrogen. (Fast) the capsule was opened during quenching, in the quenching water, or (slow) after quenching, out of quenching water. Sample temperature equaled to room temperature.	61
3.12	DSC charts of Ni _{50.8} Ti _{49.2} alloy after the Regime I heat treatments in air, argon and helium.	62
3.13	DSC charts of the Ni _{50.8} Ti _{49.2} alloy after the Regime II heat treatments in air, argon and helium.	63
3.14	DSC charts of the Ni _{50.8} Ti _{49.2} alloy after the Regime I heat treatments in either oxygen, nitrogen, hydrogen or in the reference inert gases - argon or helium.	64
3.15	DSC charts of the Ni _{50.8} Ti _{49.2} samples heat treated in Regime I in pure hydrogen and hold at 200 °C for 1.8 or 3.6 ks between the two DSC analysis.	65
3.16	DSC charts of the Ni _{50.8} Ti _{49.2} samples heat treated in the Regime I in either hydrogen-helium mixtures (H ₂ partial pressure 20, 100, 500 and 700 mbar) or in the reference helium atmosphere.	65
3.17	DSC charts of the Ni _{50.8} Ti _{49.2} samples that were heat treated in the Regime II in hydrogen-helium mixtures (H ₂ partial pressure 20, 100, 500 and 700 mbar) or in the reference helium atmosphere.	66
3.18	SAD patterns of the quenched Ni _{50.8} Ti _{49.2} alloy taken in the zones [111] _{B2} , [100] _{B2} , [110] _{B2} and [210] _{B2} . The patterns were obtained after heat treatment in Regime I in hydrogen (a1-4) or reference helium atmosphere (b1-4).	67

3.19	SAD patterns of the quenched Ni _{50.8} Ti _{49.2} alloy taken in the [001] _{B2} zone. The patterns were obtained after the Regime I heat treatments in hydrogen-helium mixtures with hydrogen partial pressure: (a) 300, (b) 500, (c) 700 and (d) 900 mbar.	68
3.20	3D APT reconstructions of 10 (a) and 1 (b) % of detected atoms of a sample taken from cylinder heat treated in Regime I in hydrogen-helium mixture (H ₂ partial pressure 700 mbar). Color codes correspond detected hydrogen, nickel and titanium atoms.	69
3.21	3D elemental map of hydrogen atoms in an AP sample after the Regime I heat treatment in hydrogen-helium mixture (H ₂ partial pressure 700 mbar) showing isoconcentration surfaces which delimit regions with hydrogen content exceeding 10 at% (color coded red). The blue regions correspond to hydrogen concentration lower than 5 %at.	69
3.22	Bright-field TEM images of the precipitation structure in a sample subjected to the Regime II heat treatment in air. The montage proceeds in the direction of the arrow from a grain boundary (G.B.) down to grain interior (G.I.).	70
3.23	Bright-field TEM images of G.B. and G.I. regions of the sample heat treated in the Regime II in air.	71
3.24	Distribution and size of Ni ₄ Ti ₃ variants as observed in TEM experiments after the Regime II heat treatment. Sample heat treated in hydrogen-helium mixtures (H ₂ partial pressures 20, 100, 300, 500 and 700 mbar) and in the reference helium atmosphere (He partial pressure 900 mbar).	72
4.1	Experimental enthalpies of Ni-Ti mixing from two sets of independent calorimetric measurements as a function of Ti mole fraction [80]. The plot also includes extrapolated values obtained for three solid intermetallic phases by Kubashewski [81] and from Gachon, Notin and Hertz [82].	75
4.2	The NiTi phase diagram (Poole and Hume-Rothery) [80]. The compositions of the melted stocks in first part of route A, B and C are marked.	76
4.3	The variation of oxygen content in the molten NiTi alloy during the VIM experiments A, B and C (C1-3) in Y ₂ O ₃ crucible with the maximum measured temperature.	77
4.4	(a) DSC chart of annealed samples of the Ni _{50.8} Ti _{49.2} melted by route B. Sample were taken from position 3, see Figure 2.4. (b) DSC data of high quality vacuum induction melted Ni _{50.9} Ti _{49.1} alloy in graphite crucible are included for comparison.	77

4.5	Transmission electron micrographs of an as-received commercial Ni _{50.8} Ti _{49.2} alloy. The dark contrasts shown in the micrographs are dislocation structures including tangled dislocation cell walls.	78
4.6	Transmission electron micrographs of two samples (a,b and c,d) annealed in helium at 850 °C for 1.8 ks and water quenched. Dislocation-free regions next to a high angle boundary (a) and well-ordered low angle boundaries (b,c and d) with dislocation loop debris inside the subgrains (c) can be observed.	79
4.7	DSC charts of (a) as-received sample and (b) samples annealed in helium at 850 °C for 1.8 ks and water quenched.	79
4.8	DSC chart of annealed sample (blue curve in Fig 4.7) split into two fitted peak described by a Gaussian function.	80
4.9	Bright-field image of annealed sample in helium subjected to cooling. The R-phase can be detected on subgrain at -52 °C (small extra spots at 1/3 <110> in the selected area diffraction pattern a). The surrounding matrix was left untransformed, formed by B2 lattice in the pattern b.	81
4.10	(a) [110] _{B2} -zone SADs obtained for the material states after Regime I heat treatments in hydrogen. Diffuse 1/2 (111) _{B2} intensity maxima are highlighted by arrows in the pattern. (b) Simulated SAD pattern assuming a B2 (blue open circles) and NiTiH (red dots) phase mixture, see text for details	84

LIST OF TABLES

2.1	Nominal composition (ppm atomic) of the Ti rod.	41
2.2	Nominal composition (ppm atomic) of the Ni rod.	41
2.3	Nominal composition (at%) of the grade SE508 NiTi alloy used in the experiments.	42
2.4	Melting routes of induction melting of $\text{Ni}_{50.8}\text{Ti}_{49.2}$ alloys.	43
2.5	Parameters characterizing five re-melting experiments of induction melting of $\text{Ni}_{50.8}\text{Ti}_{49.2}$ alloys.	44
3.1	The oxygen content (atomic ppm) in the raw materials and the alloys after melting and solidification.	54
3.2	The start and the rise of temperatures ($^{\circ}\text{C}$) when the remainder of nickel was added in second melting step.	57
3.3	The coefficient of thermal conductivity of gases at 0°C and 1 atm (1.01325 bar) [29].	61
A.1	Enthalpy changes [J/g] associated with martensitic transformation $\text{B2} \leftrightarrow \text{B19}'$ in the supplied and the re-molten $\text{Ni}_{50.8}\text{Ti}_{49.2}$ alloy at 1500°C with holding time 2, 10 and 20 min, and at 1500°C and 1450°C with 20 min of holding time.	107
A.2	Characteristic phase transformation temperatures [$^{\circ}\text{C}$] and enthalpy changes [J/g] associated with martensitic transformations in the $\text{Ni}_{50.8}\text{Ti}_{49.2}$ samples heat treated in Regime I in air, argon and helium.	107
A.3	Characteristic phase transformation temperatures [$^{\circ}\text{C}$] and enthalpy changes [J/g] associated with martensitic transformations in the $\text{Ni}_{50.8}\text{Ti}_{49.2}$ samples heat treated in Regime II in air, argon and helium.	108
A.4	Characteristic phase transformation temperatures [$^{\circ}\text{C}$] and enthalpy changes [J/g] associated with martensitic transformations in the $\text{Ni}_{50.8}\text{Ti}_{49.2}$ samples heat treated in Regime I in oxygen, nitrogen, hydrogen, argon and helium.	108
A.5	Characteristic phase transformation temperatures [$^{\circ}\text{C}$] and enthalpy changes [J/g] associated with martensitic transformations in the $\text{Ni}_{50.8}\text{Ti}_{49.2}$ samples heat treated in Regime I in reference helium atmosphere, hydrogen-helium mixtures (H_2 partial pressure 20, 100, 500 and 700 mbar) and pure hydrogen.	109
A.6	Characteristic phase transformation temperatures [$^{\circ}\text{C}$] and enthalpy changes [J/g] associated with martensitic transformation in the $\text{Ni}_{50.8}\text{Ti}_{49.2}$ samples heat treated in Regime II in reference helium atmosphere or hydrogen-helium mixtures (H_2 partial pressure 20, 100, 500 and 700 mbar).	109

1 INTRODUCTION

1.1 The unique behavior of NiTi alloys

A unique behavior of polycrystalline Ni-Ti alloys (containing 49–51 at% Ni), such as shape memory effect (SME) consisting of mechanical memory (pseudo-elasticity, PE) and thermal memory (one way effect, 1WE) results from a reversible martensitic transformation between two phases, each with a different crystal structure and therefore different properties [1, 2, 3]. SME of NiTi shape memory alloys (SMAs) can be exploited many times compared to other SMAs till a malfunction or structural degradation occurs [4, 5, 6, 7, 8]. PE of the NiTi alloys is associated with a large non-linear recoverable strain upon loading and unloading at a temperature range where a high temperature phase called austenite is stable. 1WE is the unique behavior where the alloy is deformed in a low temperature regime where a low temperature phase called martensite is stable and recovers its original shape by the reversible martensitic transformation on heating.

The behavior is extremely sensitive to the initial chemistry as well as the subsequent processing [1]. Current development and growth of NiTi SMAs applications in the industrial and commercial markets induces a good control over the manufacturing process in order to deliver high quality products. This principle becomes increasingly important. Ensuring purity, understanding the impact of the manufacturing process and its effect on product performance is a key to successful process controls. Furthermore, there is a steadily growing interest in a comprehensive knowledge on effects which treatment conditions may have on the structure of the B2 phase, and, consequently, on the transformation behavior and mechanical properties of the NiTi alloys. The comprehensive knowledge is still lacking, largely owing to the complexity of the issue itself.

1.2 The outline of this work

The Introduction briefly summarizes a background knowledge related to martensitic transformations and the processing of NiTi alloys. Martensitic transformations in NiTi alloys, crystallographic theory of martensite formation, transformation thermodynamics and physical metallurgy of NiTi alloys are briefly discussed in following Sections including remarks on the effect of impurities. The Introduction was structured regarding to two major subjects of my thesis (Section 1.8): induction melting in Y_2O_3 crucible and heat treatments under controlled environments. The Introduction is then followed by chapters on experimental techniques, results and their discussion. Finally, main conclusions are drawn.

1.3 Reversible martensitic transformations

In the NiTi alloys, the high temperature austenite phase (the parent phase) transforms into the low-temperature martensite phase (the product phase) and the martensite phase then transforms back to the austenite phase. This reversible martensitic transformation is a first-order, diffusionless solid-solid transformation and can be induced by both applied stress and temperature variation [9, 1].

During the martensitic transformation, the parent lattice is distorted cooperatively (shear lattice distortion) into the product lattice by moving atoms by less than one interatomic distance. Due to the diffusionless nature of the transformation, no change in composition occurs. The transformation process may include an intermediate phase, R-phase, as other martensite candidate [10, 11, 12, 13]. Thin $1/3$ superlattice reflections along $\langle 110 \rangle^*$ and $\langle 111 \rangle^*$ reciprocal lattice directions of B2 phase appear [14]. Such transformation path is known as two-step transformation [15, 16]. This transformation proceeds from B2 austenite through the R-phase to the final product B19' martensite [1]. All various combinations of the aforementioned transformations taking place in NiTi SMAs are martensitic in nature and are reversible. The reverse transformation occurs by the backwards movement of the interface between the product and the parent phases, and the product phase shrinks and reverts completely to the initial parent phase with the original orientation [17]. This class of the reverse transformations is called thermo-elastic [17].

The crystallographic variants of the martensite phase form as thin lenticular plates growing into the austenite grain. The rate with which the individual variants grow may approach the velocity of sound in the material [9]. The plates initially are very thin and subsequently thicken during the growing process. The lenticular

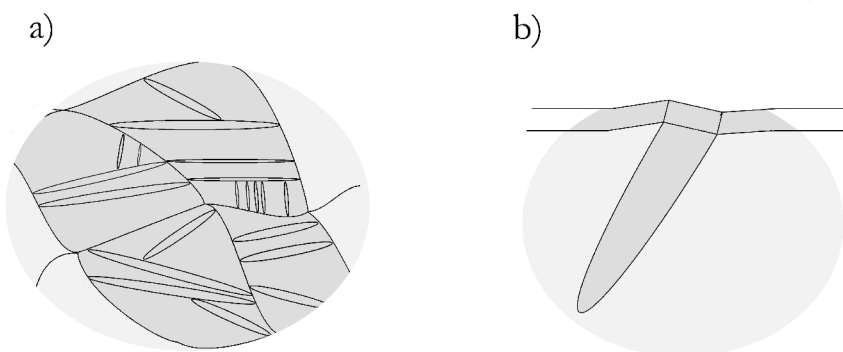


Fig. 1.1: (a) Growth of plates terminated at grain boundaries and at other martensite plates. (b) Surface upheaval due to the plate intersecting the surface of the sample [19].

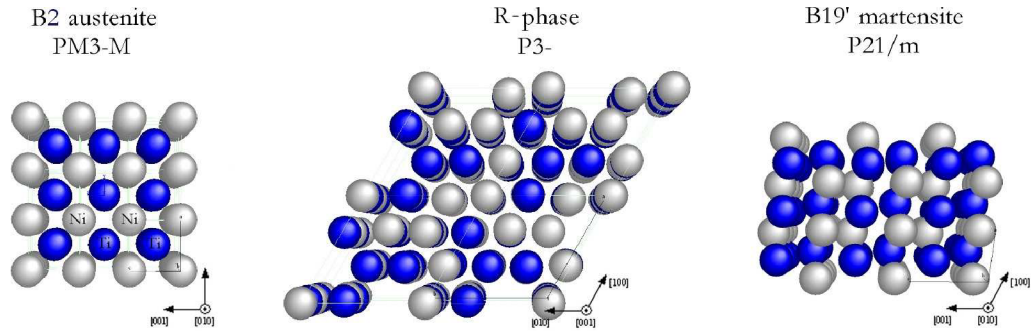


Fig. 1.2: The observed experimental structures of NiTi: B2 austenite, R-phase and B19' martensite (cubic coordination). Ni and Ti atoms are shown as gray and blue-coded spheres, respectively.

shape of plate is formed rather than mechanical twin to minimize strain energy associated with the shape and the volume change between the corresponding crystal structures [18]. The size of the plate is usually limited by the boundaries of the initial austenite grain, in which the plate nucleated, the specimen surface, or a neighbor martensite plate (Fig. 1.1a) [19]. The intersection of martensite plate and the sample surface causes a change in the surface shape in accord with the macroscopic shape change accompanying the transformation (Fig. 1.1b). The process of the formation of the plates can be autocatalytic in the sense that a growing plate can trigger the nucleation and growth of other plates [9].

1.3.1 Crystal structures

The austenite phase has ordered B2-type cubic structure that belongs to a Pm-3m space group (Fig. 1.2). The lattice constant of the B2 phase is 0.3015 nm at room temperature [20, 21, 22, 23].

The R-phase formed by a rhombohedral distortion of the B2 cubic structure belongs to a space group $P\bar{3}$ [24, 25]. With respect to the austenite B2 lattice, the R-phase is elongated 0.94% in the direction $[111]_{B2}$ [1]. The lattice parameters using a hexagonal lattice indexes for convenience are $a = 0.738$ nm and $c = 0.532$ nm [87].

The martensite phase has a B19'-type monoclinic structure with space group P21/m [27, 21]. The unit cell of the B19' phase is elongated about 10 % in the direction $[223]_{B2}$ [1]. B19' lattice parameters obtained by a single crystal X-ray diffraction method for $\text{Ni}_{50.8}\text{Ti}_{49.2}$ composition are $a = 0.2892$ nm, $b = 0.4108$ nm, $c = 0.4646$ nm and $\beta = 97.78^\circ$ [28].

1.4 Crystallographic theory of martensite

The fact that martensite plates can grow and shrink with velocity approaching the velocity of sound at very low temperatures (from -50 to 100°C for NiTi shape memory alloys (SMAs) [2]) results from an excellent mobility of the interface between the martensite and the parent phases. The interface moves without any assistance of diffusion. Such interface is called a glissile interface. Contrary, the interface that cannot translate without diffusion is called a sessile interface. There are necessary conditions for the interface to be glissile. The continuity of the structure across the interface must be high and the interfacial set of dislocations, which provides discontinuity between the two phases, must move only by glide. Contrary, climb is dislocation motion involving diffusion of atoms over long distances, thereby this mode of dislocation motion is not permitted during martensitic transformations [18, 9].

During the martensitic transformation the interfaces are semi-coherent and their discontinuities are screw dislocations or dislocations the Burgers vector of which

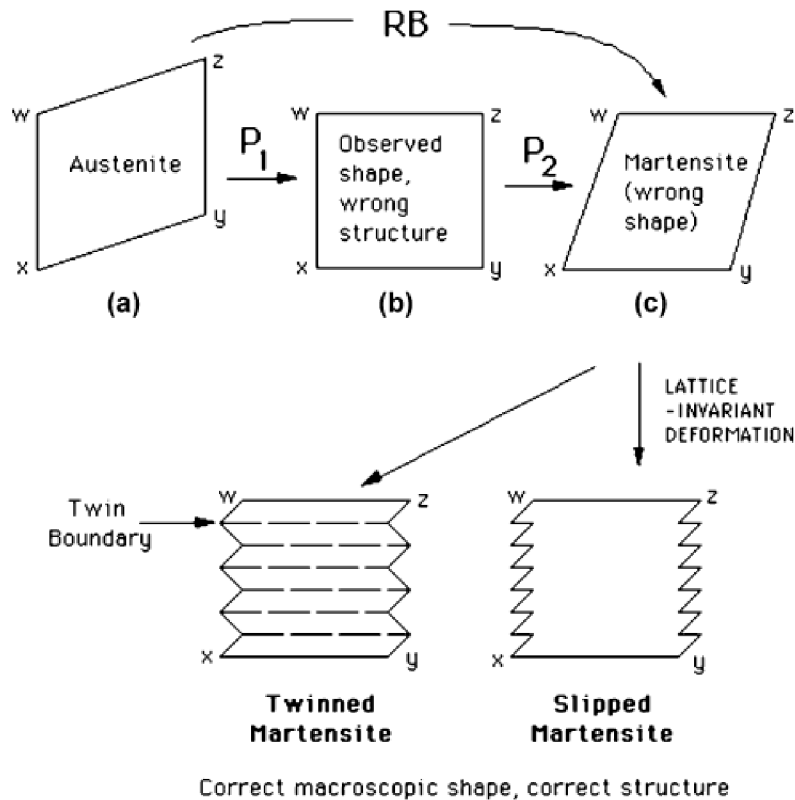


Fig. 1.3: Schematic representation of lattice distortions which provide the experimentally observed orientation relationship between austenite and martensite, and correct macroscopic shape of martensitic plates [18].

do not lie in the interface. Motion of such interface is conservative, i.e., it does not cause the creation or destruction of lattice defects. If there is a second set of dislocations, then these should have the same line vector in the interface, or their Burgers vector must be parallel to the original set. It means there are lines in both phases that are not distorted or rotated on passing through the interface. These lines are called invariant-lines. The presence of invariant-lines is the essential feature of the martensitic transformation [18].

Lattice distortions (Fig. 1.3), which lead to the experimentally observed orientation relationship between parent and product phases, are a homogeneous deformation known as Bain strain (B) and rigid body rotation (R). The combination B and R is equal to a series of two invariant-plane strains. Both combinations lead to the irrational orientation relationship and leave one line undistorted and unrotated. Nevertheless, the combination RB alone results in a wrong shape of martensite. To obtain correct macroscopic shape of martensite plate without a change of the structure one more mechanism is needed, which can be either twinning or slip. This mechanism reduces strain and is essential in nucleation and growth of martensitic phases. This mechanism also explains irrational indexes of habit planes. The habit plane is a plane separating austenite and martensite with zero macroscopic (not microscopic) distortion. The indexes of a habit plane can be obtained as an average one of rational indexes that characterize crystallographic planes [18].

More than one habit plane can be calculated by the described phenomenological theory of martensitic transformations and also found experimentally in the martensite structure. A presence of the habit plane variants in the martensite structure (martensitic variants) leads to efficient reduction of strain during martensitic transformations. The martensite microstructure can exist in two forms: twinned martensite, which is formed by a combination of "self-accommodated" variants of the martensite phase (up to 24 B19' and 8 R-variants for NiTi SMAs), and detwinned or reoriented martensite in which a specific variant is dominant [19, 18].

1.5 Thermodynamics

From the point of thermodynamics, any transformation, including the martensitic one, is possible and can occur spontaneously at constant pressure and temperature if the related change in Gibbs free energy is negative [29]. Therefore, the criterion of a measurable change in the free energy, when a system changes form an initial state with free energy G_i to a final state of free energy G_f , can be expressed as:

$$\Delta G_{T,p} = G_f - G_i < 0. \quad (1.1)$$

By including more thermodynamic state functions, this expression becomes:

$$\Delta G_{T,p} = \Delta H - T\Delta S < 0 \quad (1.2)$$

where ΔH is a change in enthalpy, T absolute temperature, and ΔS a change in entropy of the system upon the transformation.

At either constant entropy ($\Delta S = 0$) or constant enthalpy ($\Delta H = 0$), respectively, we obtain:

$$\Delta H_{S,p} < 0 \quad \Delta S_{H,p} > 0. \quad (1.3)$$

The first formula states that, in a system of constant entropy held at constant pressure, the enthalpy (the total kinetic and potential energy of the atoms in the system) must decrease during a spontaneous change. The second inequality requires that, if the enthalpy and pressure of the system are constant, the entropy (the dissipation of energy in the system) increases during a spontaneous change [29].

Therefore, transformations are spontaneous in the direction of decreasing free energy, moving towards the most stable state ($G_f < G_i$). The stable state is the one with the best compromise between low enthalpy and high entropy. However, in line with the second Law of Thermodynamics, the tendency to lower G is solely a tendency towards states of greater overall entropy [29]. Systems change spontaneously if the total entropy of the system and its surrounding increases, not because of decreasing internal energy of systems [29]. In reversible processes, overall entropy does not change ($\Delta S_{universe} = \Delta S_{system} + \Delta S_{surroundings} = 0$).

At an equilibrium temperature T_0 which is characteristic for a given phase transitions any transfer of energy as heat between the system and its surroundings is reversible by definition because the initial and final states are in equilibrium [19]. We can write $\Delta G = 0$ in Eq. 1.2. Then at constant pressure the change in entropy of the system is:

$$\Delta S_p = \frac{\Delta H_p}{T_0} \quad (1.4)$$

Phase transformations are accompanied by a decrease in free energy, see Eq. 1.1. The phase transformation between B2 austenite and B19' martensite is martensitic and takes place upon a temperature change. The difference in free energy between these two phases at a temperature different from the equilibrium temperature than represents the driving force for the phase transition [19]. The free energy of the B2 austenite and B19' martensite at the temperature T is given by:

$$G^{B2} = H^{B2} - TS^{B2} \quad (1.5)$$

$$G^{B19'} = H^{B19'} - TS^{B19'} \quad (1.6)$$

Therefore, the driving forces are $\Delta G = G^{B19'} - G^{B2}$ for the forward and $\Delta G = G^{B2} - G^{B19'}$ for the reverse martensitic transformation.

For a small temperature change the difference in the specific heats of these two phases can be ignored. Then ΔH and ΔS are approximately independent of temperature and the substitution of Eq. 1.4 into Eq. 1.2 gives

$$\Delta G \approx \left(1 - \frac{T}{T_0}\right)\Delta H \quad (1.7)$$

On cooling the forward transformation from B2 austenite to B19' martensite is exothermic process that releases energy as heat into its surroundings. The driving force for the exothermic process than requires undercooling of the system:

$$\Delta G < 0 \quad \Delta H < 0 \quad \left(1 - \frac{T}{T_0}\right) > 0 \quad (1.8)$$

On the contrary, on heating the transformation form B19' martensite to B2 austenite is endothermic process in which energy is acquired from its surroundings as heat. The driving force for this endothermic transition requires overheating of the system:

$$\Delta G < 0 \quad \Delta H > 0 \quad \left(1 - \frac{T}{T_0}\right) < 0 \quad (1.9)$$

The endothermic reverse transformation rises spontaneously to states of higher enthalpy at $T \geq A_s$ (austenite start temperature). It follows that the entropy of the system increase so much that $T\Delta S$ is strongly positive and outbalances the positive enthalpy change ΔH , see Eq. 1.2.

Dependencies of free energy on temperature characterizing B19' martensite and B2 austenite is shown in Fig. 1.4. As an example, a NiTi alloy is undercooled by ΔT

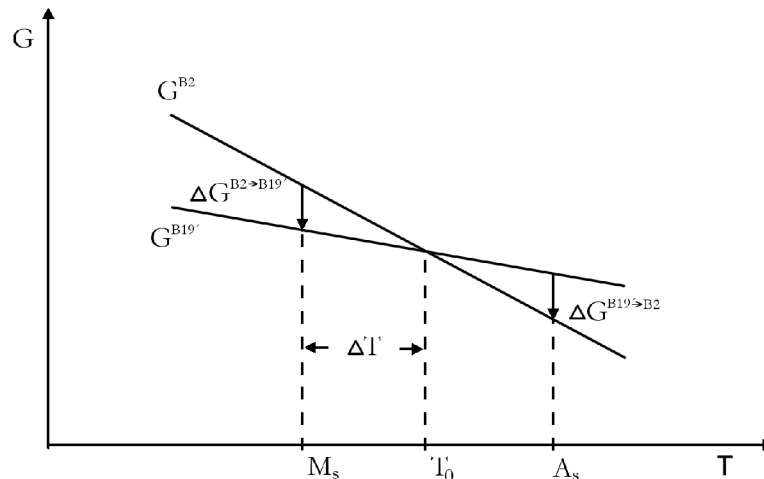


Fig. 1.4: Difference in free energy between martensite and austenite close to equilibrium temperature T_0 . The curvature of the G^{B2} and $G^{B19'}$ lines has been ignored [19].

below T_0 before it transforms. The transformation will be accompanied by a decrease in free energy $\Delta G^{B2 \rightarrow B19'}$ at temperature M_s (martensite start temperature) as shown in Figure 1.4. This free energy decrease provides the aforementioned driving force for the transformation.

The reverse transformation can be induced mechanically as well as thermally. An explicit dependence exists between the critical stress and the critical temperature. The dependence can be represented by a Clausius-Clapeyron type equation:

$$\frac{\Delta\sigma}{\Delta T} = -\frac{\rho\Delta H}{T_0\epsilon_t} \quad (1.10)$$

where ρ is the density of the transforming body and ϵ_t is the linear strain of the transformation in the direction of the uniaxial stress.

The change in free energy ΔG (1.2) is only associated with the structural lattice change between the initial and the final state. The total change in the effective driving force $\Delta G'$ of a system during martensitic transformations may be than expressed as [19]:

$$\Delta G' = \Delta G + \Delta G_{ne} \quad (1.11)$$

where ΔG_{ne} is a change due to nonchemical effects. Nonchemical energy term can be expressed as:

$$\Delta G_{ne} = \Delta G_s + \Delta G_e + \Delta G_p \quad (1.12)$$

where ΔG_s is a change in a surface energy between austenitic and martensitic phase, ΔG_e is a change in an elastic energy around the martensitic plates, and ΔG_p is a change which stems from a plastic energy stored in the system during the transformation. During thermoelastic martensitic transformation ΔG_p term is insignificant compared with the other two nonchemical terms. In most martensitic transformations, including the transformation in NiTi SMAs, ΔG_{ne} is comparable to ΔG_e . Therefore ever increasing undercooling is necessary for the nucleation of the martensitic phase and progress of the forward transformation. Similarly, ever increasing superheating is necessary for the reverse transformation ($T_0 \neq M_s \neq A_s$). The same reasoning can be applied to inequality of transformation temperatures: M_s , M_f (martensite start and finish temperatures), and A_s , A_f (austenite start and finish temperatures). The elastic energy around the martensite resists the growth of the martensitic plates unless a further driving force (more supercooling or more superheating) is provided. Details on the transformation temperatures are provided in Section 1.6.2.

During the transition from the initial state into the state of lower free energy, the system must pass through a so-called activated state with free energy above G_i . The associated increase of free energy above the G_i is known as the activation free energy barrier. The activation energy is the minimum energy that parent phase must have

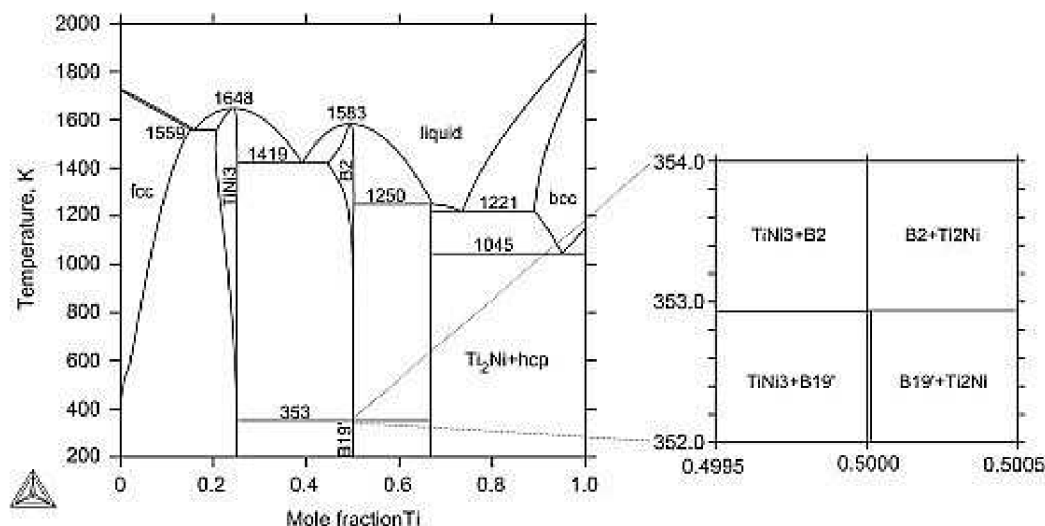


Fig. 1.5: Calculated phase diagram of NiTi binary system, to which the phase equilibrium between B2 and B19' phases is added together with stable phases NiTi_2 and NiTi_3 [30].

in order to form product phase. The kinetics of transformations will depend on the activation free energy barrier and frequency with which atoms reach the activated state.

1.6 Physical metallurgy of Ni-Ti alloys

1.6.1 Phase diagram

The research focuses on the central region of the phase diagram situated round the equiatomic NiTi composition (Fig. 1.5). The reason is that solid solution B2 austenite phase of a near-equiatomic Ni-Ti alloy exhibits the unique behavior based on the reversible martensitic transformation as it was mentioned in Section 1.1 [31, 32, 33]. In Figure 1.5, the right boundary of B2 phase field is almost vertical. On the other hand, there is pronounced solubility of Ni atoms in NiTi intermetallic on the Ni-rich side in the temperature range between 830 and 1310 °C. At temperatures below 650 °C there is a very narrow NiTi-phase region and it is generally accepted that this region accommodates composition only between 50.0 and 50.5 at% Ni [1]. The NiTi phase retains the B2 order until a low temperature when the martensitic transformation occurs.

1.6.2 Transformation temperatures

From the B2 phase stability regime, the B2 structure starts to transform into the B19' martensite phase at M_s (the martensite start temperature) on cooling. The volume transformed into the martensite is a function of temperature. Holding at any temperature below M_s for any length of time does not cause the formation of more "athermal" martensite. The parent B2 phase is completely transformed into the product B19' martensite for temperatures below M_f (the martensite finish temperature). If the transformation process includes the R-phase, the start and the end temperatures of the transformation from the austenite to R-phase are denoted by R_s and R_f , respectively. On heating, the reverse transformation from B2 austenite to B19' martensite phase takes place. The temperature, at which the reverse transformation begins, is denoted by A_s . Similarly, the last remnant of martensite disappears at the temperature A_f . There is transformation temperature hysteresis such that $A_s > M_f$ and $A_f > M_s$. If the reverse transformation includes the R-phase, corresponding transformation temperature are denoted A_{Rs} and A_{Rf} on heating. The magnitude of thermal hysteresis of the B19' phase transformation is much larger (one order of magnitude higher) compared with the magnitude of the thermal hysteresis of the R-phase transformation (more in Section 1.6.5).

There is a strong composition dependence of the B19'-Phase transformation temperatures (PTTs), see Fig. 1.6; the PTTs decrease significantly with increasing concentration of Ni atoms in the Ni-rich NiTi-phase [34]. The PTTs can change by about 20°C per added 0.1 at% Ni [24].

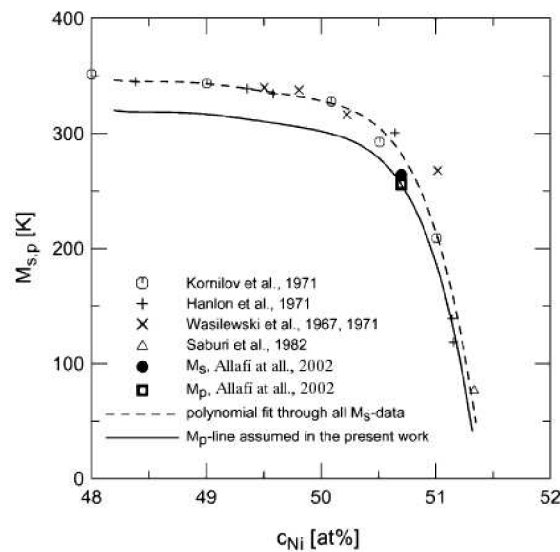


Fig. 1.6: Relation between nickel content and M_s , or M_p temperatures [35].

As mentioned earlier in Section 1.5, martensitic transformations can be triggered by external applied stress according to the Clausius-Clapeyron type relationship. The highest temperature at which martensite phase can form under applied stress is denoted M_d [9, 36, 37]. M_d is the temperature above which the chemical driving force becomes so small that nucleation of martensite cannot be mechanically induced [17]. In the following section I will introduce a SMA phase diagram of one-step martensitic transformation in temperature-stress coordinates, where a dependence of transformation temperatures on applied stress can be seen.

SMA phase diagram

In SMA phase diagram (Fig. 1.7) [38] the pure phases austenite (A), twinned martensite (M^t) and detwinned martensite (M^d) can exist only in respective shaded regions. All three regions are separated by transformation field, labeled according to the type of transformation taking place. In overlap regions (non-shaded in Fig. 1.7) multiple transformations take place and various mixtures of phases can exist. Four phase transformations are denoted in Figure 1.7: 1) from austenite to twinned or "self-accommodated" martensite ($A \rightarrow M^t$), 2) from austenite to detwinned martensite ($A \rightarrow M^d$), 3) from twinned martensite to austenite ($M^t \rightarrow A$) and 4) from detwinned martensite to austenite ($M^d \rightarrow A$). Moreover, one inelastic deformation process of reorientation of martensite variants ($M^t \rightarrow M^d$) is also highlighted.

One-step martensitic transformation induced by temperature variation at zero-

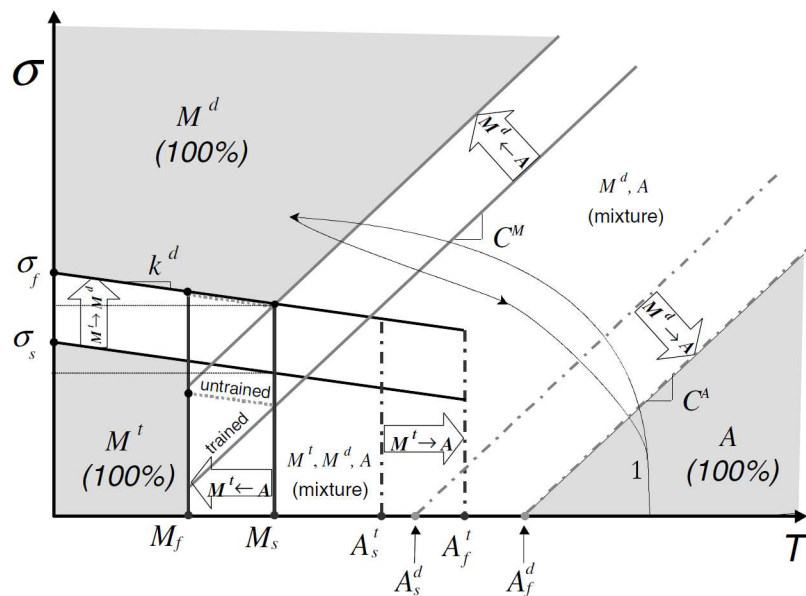


Fig. 1.7: The SMA phase diagram of stress and temperature (see text) [38].

stress involves transition $A \rightarrow M^t$. PTTs (M_s , M_f , A_s^t and A_f^t) of the transition lay on x -axis in Figure 1.7. Notice that there are additional start and finish temperatures A_s^d and A_f^d of phase transition $M^d \rightarrow A$, which are assumed different from temperatures A_s^t and A_f^t . Temperatures A_s^d and A_f^d on x -axis were measured in a detwinned sample (austenitic temperature was well above room temperature) after elastic unloading and compared with A_s^t and A_f^t of the annealed identical sample. The explanation of the results is based on the assumption that [38] detwinned martensite needs additional energy input to reverse the inelastic strain around the interface between the martensite and the austenite phases and thus the transition occurs at higher temperatures, compared to twinned martensite. There are three transition stresses that exhibit the temperature dependence, namely stresses that characterize transitions $A \rightarrow M^d$, $M^d \rightarrow A$ with positive slopes and $M^t \rightarrow M^d$ characterized by a negative slope. For untrained SMA alloys, it is assumed that the band $A \rightarrow M^d$ (solid line) changes slope at M_s and at temperatures below M_s they have slope k_d (dashed lines) (for more details see study [38]).

As example in Figure 1.7, number 1 marks one possible thermomechanical loading path. The path starts well above M_s and thus the sample is entirely in the B2-phase state when loaded. On simultaneous stressing and temperature decrease in A -marked shaded region, the elastic deformation of austenite starts. Higher stress is required for nucleation of M^d -phase at temperature much higher than M_s . The reason is that the parent phase is more stable in higher temperature ranges, and thus higher stress is required to start transformation. The path is continuing over the $A \rightarrow M^d$ region, where the phase transformation takes place. Sample is entirely in M^d at the end of the first semicycle. When the sample is unloaded and temperature increases to the initial value, the M^d phase transforms back to B2-phase. There is stress-strain hysteresis. Loading paths are not identical with the unloading ones. The described path 1 represents general microstructural change during superelastic cycles in a NiTi SMA subjected to changes of temperature and stress.

1.6.3 Melting and casting

Induction melting (IM) under a protective argon atmosphere and vacuum arc remelting (VAR) are the most commonly used processes for the commercial production of NiTi SMAs (see Fig. 1.8) [36, 39]. During (IM), the crucible is held in insulating material and introduced into the work coil which is connected to the power supply. The electric current through the coil generates an alternating magnetic field. The alternating magnetic field induces eddy currents that heat the ingot. IM is performed under vacuum or an inert gas atmosphere. For the production of NiTi SMAs, graphite crucibles are commonly used [40]. The important advantage of the IM is

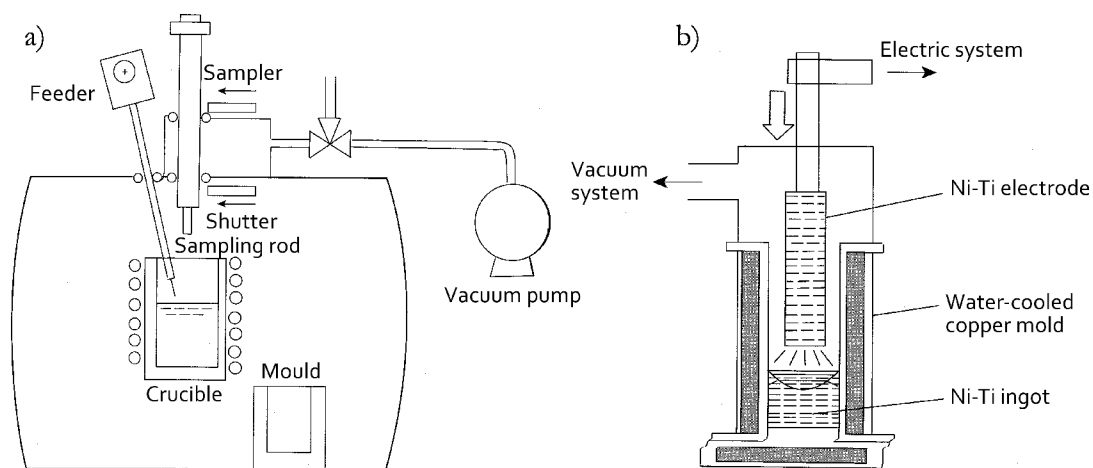


Fig. 1.8: Schematic drawing of VIM (a) and VAR (b) process [36].

the melt stirring due to the eddy currents which leads to a good mixing and the homogeneity of chemical composition throughout the ingot.

In VAR process, a discharge arc is generated between an electrode and the mold base, or between an electrode and the ingot. The electrode melts and drops alloy into a water-cooled copper mold. Only a part of the alloy electrode melts and the process is thus limited to a small melting zone. The small melting zone makes it difficult to obtain fully homogenous ingot as far as the chemical composition is concerned. The distribution in transformation temperatures is then a direct consequence of the inhomogeneity. Remelting is required. An alternative way can combine both, VIM and VAR techniques in a double melting process, using first VIM melting followed by VAR re-melt to get homogenous and large-scale ingots [36, 39].

1.6.4 Heat treatments (decomposition of Ni-rich alloys)

If near-equiatomic B2-phase NiTi alloys with nickel contents below 50.0 or above 50.5 at% are subjected to aging at temperatures in a range between 200 and 800 °C, they decompose into multiphase systems. Final products of the decomposition are mixtures of stable phases NiTi and either NiTi₂ or Ni₃Ti depending on the initial composition of the alloy (see Fig. 1.5 in Chapter 1.6.1) [1]. As mentioned in Chapter 1.6.1, the boundary limiting the B2 phase region on a Ti-rich side is straight line, almost perpendicular to the concentration axis of the phase diagram. Consequently, it is easier to obtain Ni-supersaturated solid solution by quenching from a high temperature (about 6 at% supersaturated Ni from 1050 °C) than Ti-supersaturated solid solution of NiTi alloys. A decomposition of Ni-supersaturated solid solution of NiTi alloys at temperature below 800 °C leads to formation of Ni-rich metastable

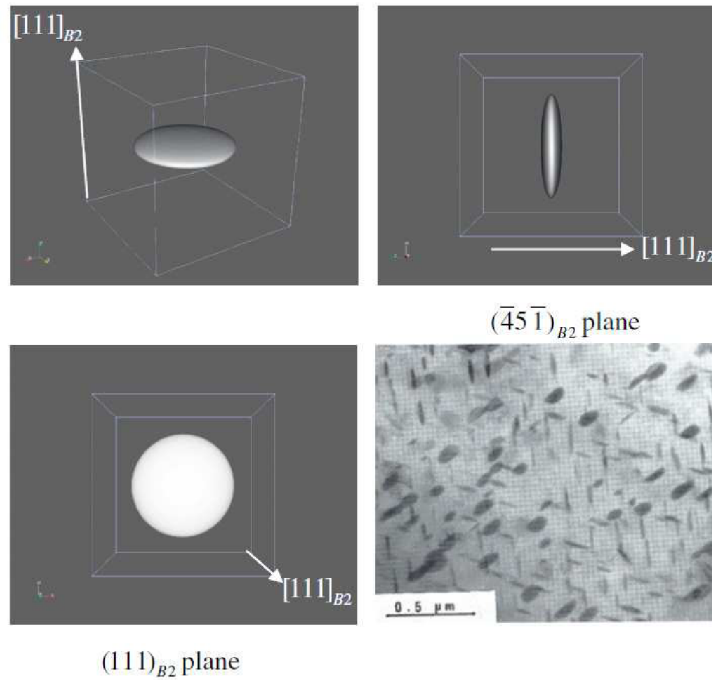


Fig. 1.9: 3D views of the equilibrium shape of an isolated Ni_4Ti_3 precipitate [22] and TEM micrograph showing precipitates of the Ni_4Ti_3 phase.

phases. One of the most important metastable phases is Ni_4Ti_3 , which proved to be useful for improving shape memory characteristics (Fig. 1.9).

The platelets of Ni_4Ti_3 precipitates form in the early stage of aging at temperatures below 680°C [41, 42, 43]. The precipitates of Ni_4Ti_3 phase have rhombohedral crystal structure with space group $R\bar{3}$. The lattice parameters for a rhombohedral unit cell of Ni_4Ti_3 phase are $a = 0.6704$ nm and $\alpha = 113.83^\circ$ [44]. The data were obtained from sample aged for 20 h at 600°C . After this heat treatment the size of the precipitates already exceeds $1 \mu\text{m}$ [44]. The precipitates are regarded as incoherent with the matrix and thus the coherency stresses are relaxed by the misfit dislocations [45, 46, 47, 48]. On aging at temperatures below 500°C [49], the size of Ni_4Ti_3 precipitates does not exceed around 300 nm in diameter and these precipitates are regarded as fully coherent with the parent (austenite) matrix. Disk with diameters in between 150 and 300 nm are considered as a limit for coherency/semi-coherency [46, 47, 48]. The coherency result in strain fields around Ni_4Ti_3 precipitates [22]. These strain fields provide effective obstacles for dislocation-mediated slip (plastic deformation) and seem to yield high mechanical strength and improved shape memory effect. Moreover, the formation of Ni_4Ti_3 precipitates results in Ni-depletion from the NiTi matrix and thus in changes of transformation temperatures [50]. Therefore, it is possible to alter the martensitic transformation path and

temperatures through controlling size and density of Ni_4Ti_3 precipitates in Ni-rich NiTi alloys [14].

1.6.5 Ni_4Ti_3 phase and its effect on sequence of martensitic transformations

A near-equiatomic NiTi alloy aged at temperature below 680°C may undergo one-step direct martensitic transformation from B2 to B19' phase or the transformation split into two steps: from austenite to R-phase and from R-phase to martensite. These three kinds of transformation are characterized by different features of transformation strain and temperature hysteresis. The phase transition from austenite to R-phase exhibits a small transformation strain of about 1% and hysteresis about $1\text{--}5^\circ\text{C}$. The second martensitic transformation between austenite or R-phase and

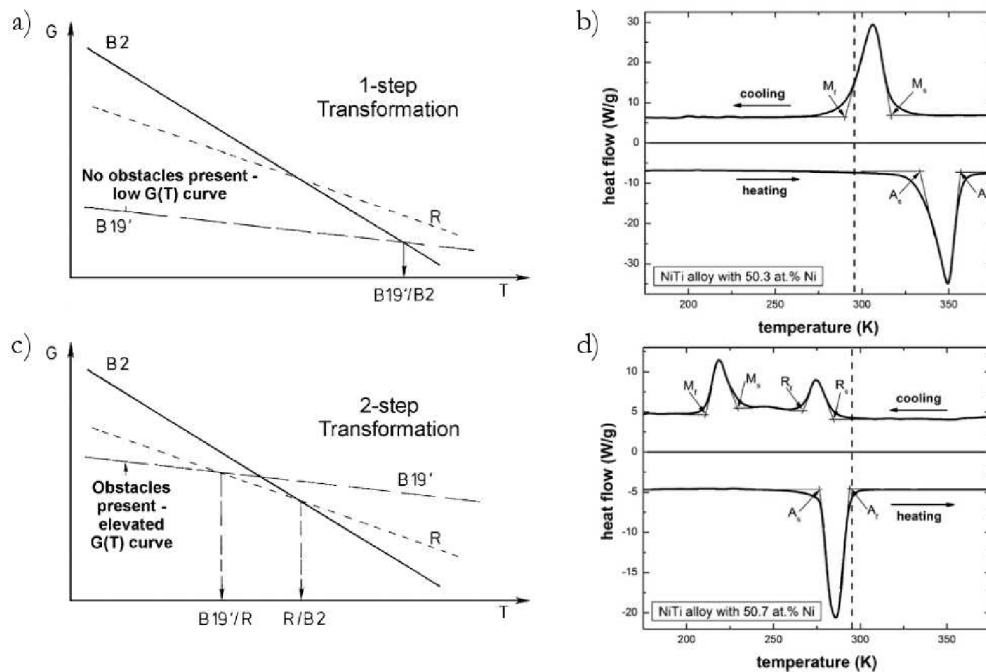


Fig. 1.10: Stability of B2, R-phase and B19' in binary Ni-rich NiTi alloy (a and c). The presence of obstacles (precipitates and dislocation substructures) makes it energetically more difficult to form B19', while the formation of R-phase is not affected (c) [51]. Schematic DSC charts illustrating one-step transformation (b), one exothermic peak on cooling from the B2 regime and one endothermic peak on heating, and two-step transformation (d), two exothermic peaks on cooling from B2 to R-phase and from R-phase to martensite and one endothermic peak on heating [52].

martensite is associated with much larger transformation strain of about 10% and hysteresis about 20–70 °C. Fine coherent Ni_4Ti_3 precipitates and their strain fields in B2-matrix give a strong resistance to the large transformation from B2 to B19' phase. Higher energy barrier of the second transformation then leads to a change from a one-step transformation into a two-step transformation with two lower partial energy barriers (Fig. 1.10) [51, 35].

Beside the stress fields, the fine Ni_4Ti_3 precipitates generate Ni concentration gradients in the surrounding NiTi matrix. The strain fields and Ni-concentration behavior contribute differently to the local phase transition during the usual two- or less usual multiple-step process (Fig. 1.11). The Ni concentration gradients exist since the Ni concentration near the long side of particle interface (particle diameter of 244 nm) is about 0.1 at% lower than that near the rim of a precipitate [22]. The lower Ni concentration can lead to locally higher martensite start temperature at the long side of particle interface. Moreover, stress fields around the precipitates favor the formation of R-phase. R-phase has the same habit plane as Ni_4Ti_3 precipitates (i.e., $\{111\}_{B2}$) and a large magnitude of the strain component along the habit plane normal, compared to small in-plane strain component. Formation of the R-phase can thus uniformly relax the coherence stresses along the habit plane normal direction in the matrix near the $\{111\}$ Ni_4Ti_3 interface. The elastic interaction between the

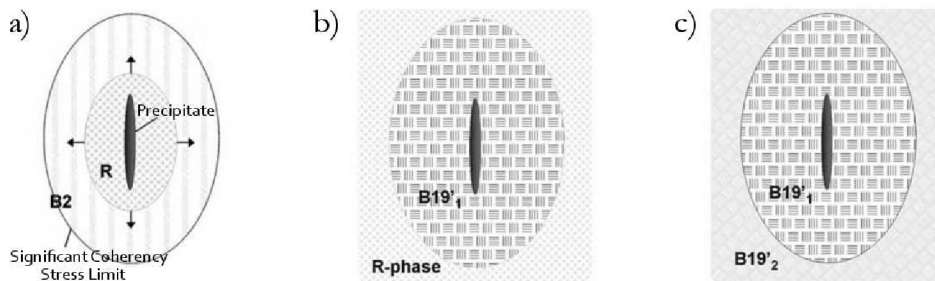


Fig. 1.11: Schematic illustration of a multiple-step martensitic transformation due to coherency stress fields around precipitates. In the first stage of the transformation sequence (a), B2 transforms into R-phase as R-phase nucleates at the particle/matrix interface and grows into the B2 matrix. In the second step (b), the R-phase transforms into B19'1. The subsequent growth of B19'1 is bounded by those region around particles which are affected by coherency stresses. Finally (c), in the third step, those region of the matrix outside the local precipitate coherency stresses are able to transform to B19'2. The same scenario might be observed even if coherency stresses were not significant, in which case varying Ni concentrations would be responsible [51].

precipitates and martensite nucleus does not favor the transition from austenite to martensite [22].

1.7 Effect of impurities on martensitic transformations

1.7.1 Carbon impurities

In solid NiTi alloys, carbon has no measurable solubility and forms exclusively titanium carbides TiC. The presence of TiC particles (which is consuming Ti) increases the Ni concentration in the NiTi matrix and accounts for the lowering of transformation temperatures (Fig. 1.12). There is a specification according to the ASTM standard for carbon content in NiTi devices. The ASTM 2063-00 standard specification, issued for wrought NiTi SMAs for medical devices and surgical implants requires maximum carbon content at or below of 0.3125 at% [50].

Possible sources of carbon are raw materials composing the melting stock and graphite crucibles employed during melting. The graphite crucible is not stable with respect to both nickel and titanium melts and carbon atoms diffuse into the liquid [57]. At 1700 °C, where both Ni and Ti are liquid, Ni melt can dissolve about 5 at% of carbon compared to Ti melt, which can dissolve about 3 at%. Additional C reacts to produce incongruent melting phase TiC. At the temperature of 1500 °C of NiTi phase, melts with increasing Ti/Ni-ratios can dissolve only about 1 at% of carbon atoms [53]. In the study by Zhang et al. [54], fine eutectic TiC fibers together with primary TiC were found in the microstructure of the as-cast Ni_{50.7}Ti_{49.3} alloy

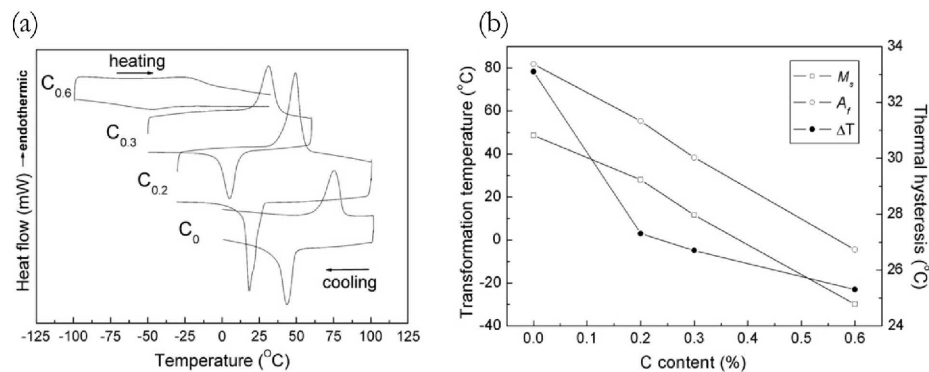


Fig. 1.12: (a) Different scanning calorimetry (DSC) charts and (b) the dependence of transformation temperature and thermal hysteresis on carbon content (0, 0.2, 0.3 and 0.6) of annealed Ni₅₀Ti₅₀ alloys [55].

with a higher carbon concentration and only eutectic TiC fibers in the low carbon Ni_{50.7}Ti_{49.3} alloy. The formation of TiC in carbon-containing NiTi SMAs was described on the basis of a quasi-binary NiTi-TiC eutectic system which has been presented by Du and Schuster [56]. In low carbon content melts with eutectic composition the "eutectic" TiC forms at the eutectic temperature. The NiTi-TiC system with high carbon content has hypoeutectic composition and the "primary" TiC particles form before the "eutectic" TiC phase. It was found that some of the eutectic TiC fiber and the matrix show specific orientation relationship [54] and their interface is semi-coherent in comparison with incoherent interface between primary TiC and the matrix. During subsequent heat treatments, the fine eutectic TiC microstructure coarsened together with the formation the new TiC particles. The primary TiC phase is not influenced. The microstructure of eutectic phases and their morphologies with primary TiC phase in NiTi matrix are shown in Fig. 1.13. TiC phase has B1-type cubic structure [54].

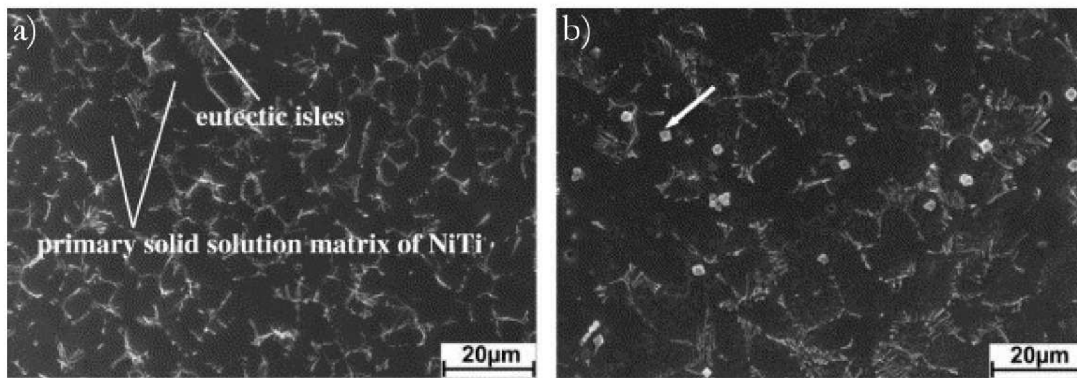


Fig. 1.13: SEM micrographs showing TiC phase in the vacuum induction melted Ni_{50.7}Ti_{49.3} alloy. (a) Hypoeutectic microstructure contains eutectic phase in the NiTi matrix, (b) Eutectic TiC phase with small primary TiC particles, one particle is highlighted by a white arrow [57].

1.7.2 Oxygen impurities

Oxygen atoms can either form an oxide phase or dissolve in NiTi matrix as interstitial impurities. The oxide phase is often characterized using a formula Ti₂NiO_x [50]. The presence of this phase as well as TiC particles increases the Ni concentration in the matrix resulting in the lowering of transformation temperatures. Solid solubility of oxygen in NiTi alloys is very small (0.045 at%) [1].

It has been shown recently [50] that the formation of the intermetallic phase Ti_2Ni is a prerequisite for the development of the oxide phase. Oxygen atoms are taken up by the Ti_2Ni phase and form the thermodynamically stable oxygen-rich Ti_2Ni particles which can be described using the formula Ti_2NiO_x [58].

Oxygen sources can be raw materials composing the melting stock, employed oxide crucibles during melting and the residual oxygen gas presented in the melting furnace or heat treatment atmosphere.

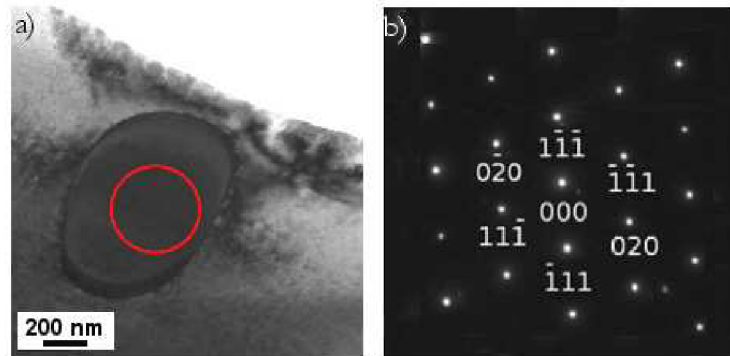


Fig. 1.14: (a) Bright-field image showing an oxide phase in the $\text{Ni}_{50.8}\text{Ti}_{49.2}$ alloy prepared by vacuum induction melting using Y_2O_3 crucible. (b) SAD pattern of the oxide phase taken in the zone [101] [59]. Lattice has a cubic structure with space group $\text{Fd-}3\text{mS}$. Lattice constant is 1.13279 nm [60].

1.7.3 Hydrogen impurities

There are many experimental and theoretical studies that explored various aspect of the interaction between environments containing hydrogen and NiTi alloys. In particular, NiTi based alloys were considered as candidate materials for hydrogen storage purposes in early stages of the hydrogen storage research [61, 62].

It is known that absorbed hydrogen causes a loss of shape memory properties of NiTi alloys. Pelton et al. [63] studied mechanical and transformation properties of Ti-50.8 at% Ni alloy which were exposed to a solution of phosphoric acid for various times in order to introduce hydrogen into the bulk of material. Pelton et al. reported that concentrations up to 1809 wppm hydrogen suppress the transformation process and hydrogen concentration greater than 400 wppm reduces ductility and increases a plateau stress. Hydrogen concentration from 20 to 1050 wppm causes an increase in the B2 lattice parameter from 3.025 to 3.047 Å, and an increase in volume by 2.2% [64]. This study also reported that the X-ray diffraction (XRD) peaks decrease in intensity with increased hydrogen content indicating a presence of

lattice strains associated with dissolved hydrogen. Hydrogen with concentrations in the 50–300 wppm has been reported to be extremely mobile at room temperature and escapes the samples. At higher levels, hydrogen is trapped at the interface and dislocations [63].

The study by Runciman et al. [65] found that the suppression of the single-stage martensitic transformation occurs at hydrogen concentrations as low as 50 wppm. This study [63] has confirmed an effect of absorbed hydrogen on martensitic transformation. DSC analysis showed a suppression of the austenite peak during heating and more significant suppression of the martensite peak during cooling. No $B2 \leftrightarrow B19'$ transition was observed in a sample with hydrogen contents above 240 wppm. Samples were also charged cathodically in a mixture of phosphoric and hydrofluoric acid.

1.7.4 Heat treatment environments

Nishida and co-workers [66] provided first evidence that variations in heat treatment environments may result in considerable changes of DSC charts. They pointed out that the solution annealing is the most significant heat treatment step as far as the impact of heat treatment atmosphere on the multiple-step martensitic transformation (MMT) path is concerned. Cooling DSC curves of $Ni_{50.6}Ti_{49.4}$ annealed samples are shown in Figure 1.15b. While the heat treatment A was performed in an evacuated quartz tube of 2.5×10^{-3} Pa, the heat treatment B is characterized by samples sandwiched between NiTi sheets, wrapped with pure Ti foil and sealed in an

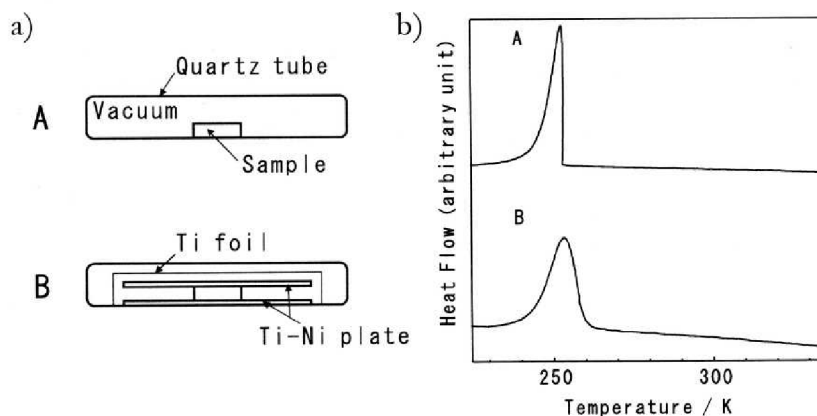


Fig. 1.15: Schematic illustration of heat treatment conditions A and B of analyzed samples (a) and their corresponding cooling DSC curves (b). The samples were annealed at 1000 °C for 3.6 ks [66].

evacuated quartz tube of 2.5×10^{-3} Pa (Fig. 1.15a). No marked difference in the DSC charts is observed between the treatments A and B. However, additional aging step and subsequent DSC analysis reveals distinctly different transformation paths after the respective combination of heat treatments A and B. The corresponding results are presented in Figure 1.16. Samples were alternatively annealed in condition A and

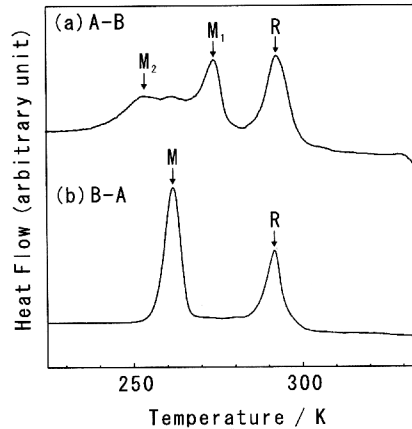


Fig. 1.16: DSC cooling curves of samples annealed at 1000°C for 3.6 ks and aged at 500°C for 7.2 ks in conditions (a) A–B and (b) B–A [66].

subsequently aged in condition B, and vice versa. In Figure 1.16, the transformation takes between B2 to R-phase is marked by the letter R. Transformations, whose products are B19' phase, are marked by the letters M1 and M2. It is obvious that the combination of heat-treatment steps leads to the usual two-step transformation whereas the A–B annealing-aging sequence yields considerably more complicated transformation path. Transmission electron microscopy (TEM) observations focused on microstructural changes associated with the heat treatments A and B [66]. TEM microstructures of samples aged at 500°C for 3600 s in conditions A–A and B–B are summarized in Figure 1.17. Two regions in the crystal structure were investigated: one near to grain boundaries (G.B.) and other in grain interior (G.I.). DSC charts of these samples have similar features as can be seen in Figure 1.16 (see [66]). The sample annealed and aged in condition B, marked by B–B, transformed in two steps (from B2 to R and from R to B19') corresponding to two sharp peaks on the cooling curves. On the contrary, there is multistage martensitic transformation in the sample heat-treated in condition A–A. The authors conclude that the heterogeneity in precipitation morphology of Ni_4Ti_3 phase (Fig. 1.17) is responsible for the MMT. They also suggest that the precipitation heterogeneity can be suppressed when the heat treatment atmosphere is carefully controlled. The size of Ni_4Ti_3 precipitates in G.I. region is about ten times larger than that in G.B. in the sample heat treated

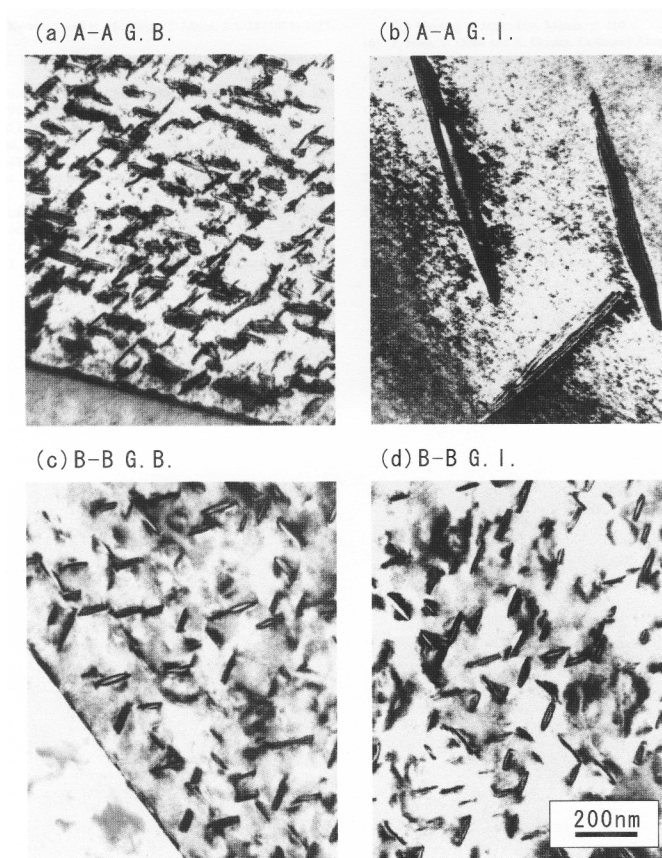


Fig. 1.17: Bright field images of G.B. and G.I. regions of the samples aged at 500°C for 3.6 ks in conditions A–A (a and b), and B–B (c and d) [66].

in the condition A–A. On the other hand, distributions and sizes of precipitates are homogeneous in the sample heat-treated in the condition B–B [66]. Fujishima and co-workers [67] also demonstrated that the appearance and disappearance of MMT in aged Ni-rich NiTi alloys depend on the heat treatment atmosphere. No MMT occurs when the evaporation of Ti and/or Ni and the preferential oxidation of Ti are prevented and heat treatment atmosphere in an evacuated quartz tube is purified using Ti-getter. In their study [67], various Ni-rich NiTi alloys were analyzed and no MMT was detected in the highly Ni-supersaturated and aged $\text{Ni}_{51.4}\text{Ti}_{48.6}$ alloy. Transformation paths taking place near the sample surface (a contaminated region with interstitial impurity elements) and in bulk (a region with higher Ni concentration) were investigated. The effect of heat treatment atmosphere on the MMT was reinvestigated in several subsequent studies, e.g. [68]. Transformation areas and their sequence corresponding to the peaks on DSC charts were estimated by SEM, EBSD and TEM observations. DSC charts of the aged $\text{Ni}_{50.8}\text{Ti}_{49.2}$ alloy in condition A together with a schematic illustration of precipitation morphology

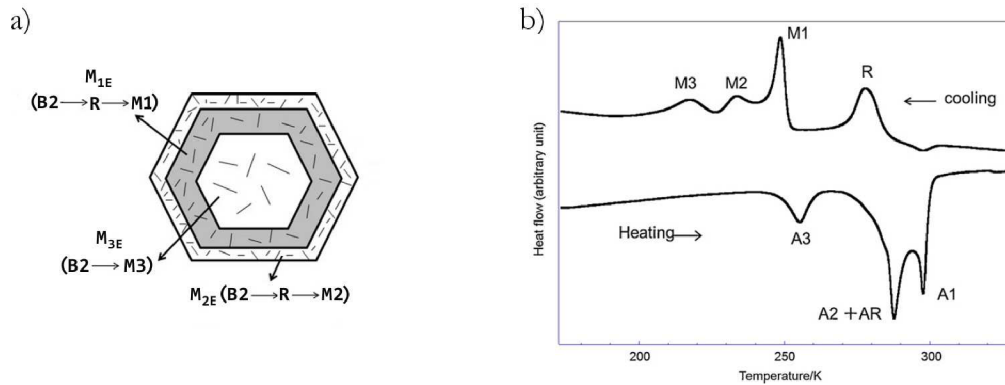


Fig. 1.18: Schematic illustration of precipitation morphology and sequence of the transformations (a), and DSC charts (b) of the aged $\text{Ni}_{50.8}\text{Ti}_{49.2}$ alloy heat-treated in condition A. The alloy were annealed at $1000\text{ }^\circ\text{C}$ for 3.6ks and aged at $500\text{ }^\circ\text{C}$ for 3.6 ks [68].

and sequence of the transformation events are presented in Fig. 1.18 [68]. From the observations, Ravari and co-workers [68] concluded that the microstructure of the aged $\text{Ni}_{50.8}\text{Ti}_{49.2}$ alloy heat treated in condition A consists of three regions shown in Figure 1.18a with different morphology of Ni_4Ti_3 precipitates. The investigated aged alloy transformed in a sequence $\text{B2} \rightarrow \text{R} \rightarrow \text{M1} \rightarrow \text{M2} \rightarrow \text{M3}$ where steps M1, M2 and M3 all represent transformations to $\text{B19}'$ martensite (Fig. 1.18b). The martensitic transformation corresponding to M1 peak takes place at the intermediate part 1 of B2 grains. The transformation corresponding to M2 peak occurs in the grain boundary regions 2. Both, M1 and M2 transformations involve intermediate R-phase transition. M3 peak corresponds to the martensitic transformation directly from B2 to $\text{B19}'$ phase. The M3 transformation takes place in the central part of B2 grains. Ceo and co-workers [69] performed a three-dimensional analysis of Ni_4Ti_3 precipitation morphology and distribution in both, grain interior and near to the grain boundaries of $\text{Ni}_{50.8}\text{Ti}_{49.2}$ alloy which exhibited the MMT effect. The precipitates near to grain boundaries show considerably smaller inter-particle distance that was suggested as an important feature for the observed MMT sequence [69]. Appearance of R-phase is related to the existence of coherent precipitates in the regions 1 and 2 including corresponding strain fields in the B2 matrix. Total number of the precipitates and their number densities were evaluated as 239 and $4.07\ \mu\text{m}^2$ in the grain interior, and 2461 and $38.5\ \mu\text{m}^2$ in grain boundary regions. Precipitates in the grain interior were also found notably larger than those close to grain boundaries [69].

1.8 The objectives of the thesis

The primary objective of the current work is to obtain sound experimental evidence and to improve the theoretical understanding of how the impurities influence the characteristics of martensitic transformations in Ni-rich NiTi SMA. Oxygen contamination of Ni-rich NiTi SMAs results from oxygen environments during induction melting experiments. Optimization of the melting conditions in u-shaped Y_2O_3 crucible should be conducted. The optimization of the melting conditions and study of interstitial impurities (introduced during melting and subsequent heat treatments) and their influence on the microstructure and martensitic transformation characteristics establishes a close link between the two main objectives of the presented investigation.

Three fundamental goals are expected which will result from the investigation:

- (i) An assessment of alloy contamination which may result from vacuum induction melting of Ni-rich NiTi-based shape memory alloys in conventional porous Y_2O_3 crucibles.
- (ii) An optimization of NiTi melting conditions with respect to the alloy purity and cost efficiency.
- (iii) An obtaining new differential scanning calorimetry (DSC) and 3D atom probe (AP) data on martensitic transformations and related hydrogen distributions in the Ni-rich NiTi shape memory alloys subjected to heat treatments under controlled environments with systematic variation of the hydrogen partial pressure.

2 EXPERIMENTAL TECHNIQUES

2.1 As-received material

2.1.1 Induction melting experiments

Titanium (99.65 at%) and nickel (99.93 at%) used in the present study was supplied by Goodfellow in the form of round rods with a diameter of 25.4 mm and 40 mm, respectively. A particular attention has been given to the effect which Y_2O_3 crucibles may have on oxygen contamination in Ni-rich NiTi alloys during induction melting. Nominal compositions of the Ti and Ni rods are given in Tables 2.1 and 2.2. U-shaped Y_2O_3 crucibles used during induction melting were purchased from Treibacher Industry AG.

Tab. 2.1: Nominal composition (ppm atomic) of the Ti rod.

Ti	Al	Co	Cr	Cu	Fe	Mg	Mn	Ni	Si	Sn	Ta	V
balance	888	2	461	151	257	39	436	408	341	81	3	470

Tab. 2.2: Nominal composition (ppm atomic) of the Ni rod.

Ni	Ag	B	Ca	Cr	Ga	Mg	N	P	Zn	Al	Cd	Cu	H
balance	<2	<27	<15	<6	<1	<12	<21	<4	<4	<9	<1	5	<291

Mn	Na	Pb	Se	As	C	Co	Fe	In	Mo	O	S	Si
<2	<13	1	<1	<1	24	85	<5	<5	<3	147	<9	<21

Ni-50.8at% Ti-49.2at% alloy in the form of three cylindrical ingots 33 mm in diameter was provided by the Institute for Materials of Ruhr University Bochum in Germany and used in order to determine the behavior of the oxygen content as a function of melting temperature and holding time. The high-quality ingot was induction melted in a graphite crucible [53].

2.1.2 Heat treatments

A commercial SE508 Ni-rich NiTi alloy purchased from EUROFlex® was used in this part of the study. The nominal composition of this grade is given in Table 2.3. The alloy with a nominal composition of $Ni_{50.8}Ti_{49.2}$ was received as annealed

Tab. 2.3: Nominal composition (at%) of the grade SE508 NiTi alloy used in the experiments.

Ni	Ti	O	H	C	Co	Cr	Cu	Fe
50.5	balance	0.0320	0,0491	0.0102	<0.0045	<0.0051	<0.0042	<0.0048

Nb	N+O
<0.0029	<0.0038

cylindrical rod. The rod dimensions were 660 mm in length and 12.7 mm in diameter. The rod was at first spark-cut into 128 mm pieces. Then the pieces were spark-cut into two types of cylinders with high of 15 mm and 2 mm (Fig. 2.1). All heat-treatment experiments were conducted with the 15 mm cylinders. The 2 mm cylinders were cut out of the as-received rod after each second 15 mm cylinder in order to detect possible additional effects associated with small compositional and microstructural processing variations along the as-received rod. The analysis of the martensitic transformation and the microstructure of the 2 mm cylinders has been a subjected of the thesis [72].

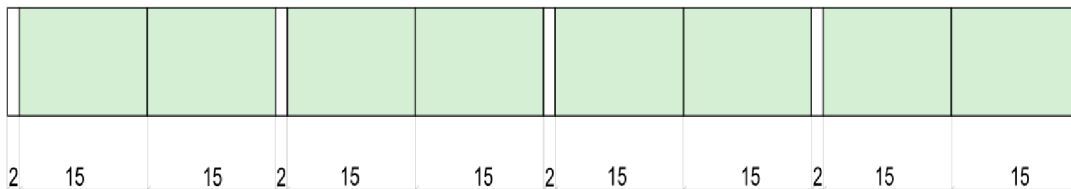


Fig. 2.1: A schematic drawing of an 128 mm piece spark-cut into 15 mm and 2 mm cylinders.

2.2 Vacuum induction melting

Induction melting experiments were carried out in cooperation with prof. Ladislav Zemčík from the Faculty of Mechanical Engineering, the Department of Foundry Engineering. Induction melting of NiTi-SMA was performed in conventional porous Y_2O_3 crucibles (see Section 2.1.1). High-purity nickel and titanium rods (see Section 2.1.1) were used as raw materials. The targeted composition for each melt was Ni-50.8 at% Ti-49.2%. Melting routes were tested in altogether five melting experiments.

Tab. 2.4: Melting routes of induction melting of $\text{Ni}_{50.8}\text{Ti}_{49.2}$ alloys.

Melting route	Procedure
A	A batch of nickel rods was melted, and then the titanium rod was put on the solidified top of the melt and the second melting was carried out.
B	A batch of nickel and titanium rods was filled into the crucible; the composition of the melt was $\text{Ni}_{35.2}\text{Ti}_{64.8}$. Then the remainder of the nickel rod was placed on the solidified top and the second melting was carried out.
C1, C2, C3	Nickel and titanium rods were filed into the crucible in a amount corresponding to an eutectic composition $\text{Ni}_{24.3}\text{Ti}_{75.7}$ and the stock was melted. The rest of the nickel was then introduced on the solidified top and the second melting was carried out.

Each experiment consisted of two-melting steps, described in Table 2.4. The cone-shaped ingots of 30 and 70 mm diameter and 180 mm length were cast from the melt. Liquid alloy was cast into graphite molds covered with Y_2O_3 protective layer (YK-type, ZYP coating). The molds were preheated to a temperature of 200°C .

The cylindrical ingots supplied by Ruhr University Bochum (see Section 2.1.1) were cut into smaller blocks of 34 mm in diameter and approximately 70 mm in length using spark erosion machining. The blocks were separately filled into Y_2O_3 crucibles and remelted. These re-molten blocks were allowed to solidify and cool to

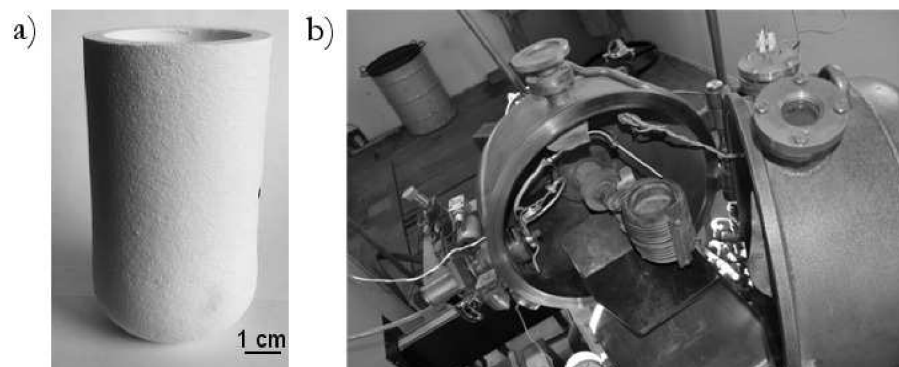


Fig. 2.2: (a) Conventional porous Y_2O_3 crucible and (b) vacuum induction melting furnace used for re-melting procedure.

Tab. 2.5: Parameters characterizing five re-melting experiments of induction melting of $\text{Ni}_{50.8}\text{Ti}_{49.2}$ alloys.

T (K)	t (s)	$o(t)$ (at.%)	V (10^{-3}m^3)	h (10^{-2}m)	S (10^{-4}m^2)	S/V (m^{-1})
1773	120	0.1457 ± 0.0020	45.80	4.2	79.88	174.41
1773	600	0.1563 ± 0.0027	52.40	4.7	86.32	164.73
1773	1200	0.2053 ± 0.0030	55.04	4.9	88.89	161.50
1723	1200	0.1920 ± 0.0027	56.36	5.0	90.18	160.01
1823	1200	0.1943 ± 0.0047	49.76	4.5	83.74	168.29

T : temperature; t : holding time; $o(t)$: oxygen content measured after time t ; $t(0)$ initial oxygen content 0.0454 ± 0.0060 ; V volume of the re-molten block; h high of the upper cylindrical block with spherical end cup; S contact area between the crucible and the melt; S/V ratio of contact area to melt volume.

room temperature inside the crucible. The five re-melting experiments were performed: at 1500°C with holding time 2, 10 and 20 min, and at 1550°C and 1450°C with 20 min holding time. The parameter characterizing these five re-melting experiments are listed in Table 2.5.

All melting experiments were conducted under low vacuum (83 kPa) by first evacuating and flushed with argon three times. During melting, temperature was measured and controlled by a WRe5-WRe26 thermocouple with an Y_2O_3 coated cermet sheath (Fig. 2.2).

2.3 Heat treatments under controlled atmospheres

The cylinders (see Section 2.1.2) were mechanically polished and ultrasonically cleaned in order to remove the surface layers affected by the cutting operations. The cylinders were ultrasonically cleaned firstly in distilled water and then in ethanol, before being dried by flow of hot air. After cleaning, some samples were heat treated in air. Rest of samples were separately sealed into quartz capsules filled with argon (6.0) or helium (5.5) or oxygen (6.0) or nitrogen (4.0) and or with hydrogen (2.0) pure gas. Filling pressure was 900 mbar. To obtain the targeted (variable) hydrogen concentrations in the heat treatment atmosphere the capsules were first pre-filled by 20, 100, 300, 500, and 700 mbar of hydrogen and then the remaining pressure difference to 900 mbar was supplied by helium.

All of the samples were heat treated in either Regime I or Regime II. In the Regime I, the samples were subjected to annealing at 850 °C for 1.8 ks and water quenched. The quartz capsules were open right after annealing step. In Regime II, the samples received the Regime I treatment and an additional aging at 450 °C for 3.6 ks terminated by water quenching. The capsules were opened only after final quenching step from aging temperature (see Fig. 2.3).

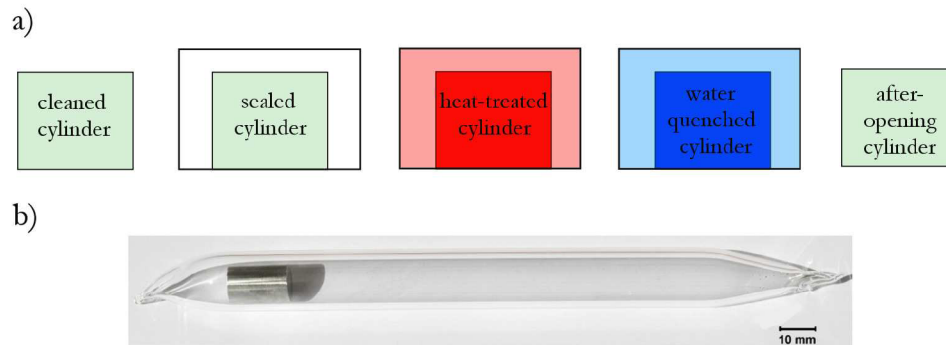


Fig. 2.3: A schema of heat treatment sequences of a cylinder (a) and the image of a cylinder sealed into quartz capsules filled with argon (b).

2.4 Analytical methods

2.4.1 Oxygen analysis

Oxygen content was analyzed in the casts (A, B, C1–3, see Table 2.4) and re-molten alloys to secure extent of oxide contamination. Figure 2.4 shows the position from which 4 mm cube shaped samples for oxygen analysis were taken (12 samples per ingot A, B and C and 5 per re-molten ingots). Before being analyzed the samples were mechanically polished and cleaned in ethanol. The content of oxygen was measured by using a LECO inert gas fusion apparatus at VÚHŽ®, a.s.

2.4.2 Differential scanning calorimetry

DSC samples were analyzed to characterize the martensitic behavior of $\text{Ni}_{50.8}\text{Ti}_{49.2}$ alloys. The disk-shaped DSC samples of about 1.5 mm in final thickness and 3 mm in final diameter were spark-cut from the homogenized pieces of the as-cast alloys A, B and C(1–3) and re-molten alloys (see Fig. 2.4), and the heat-treated cylinders. The pieces with dimensions 2.5x4xvariable mm were subjected to homogenization

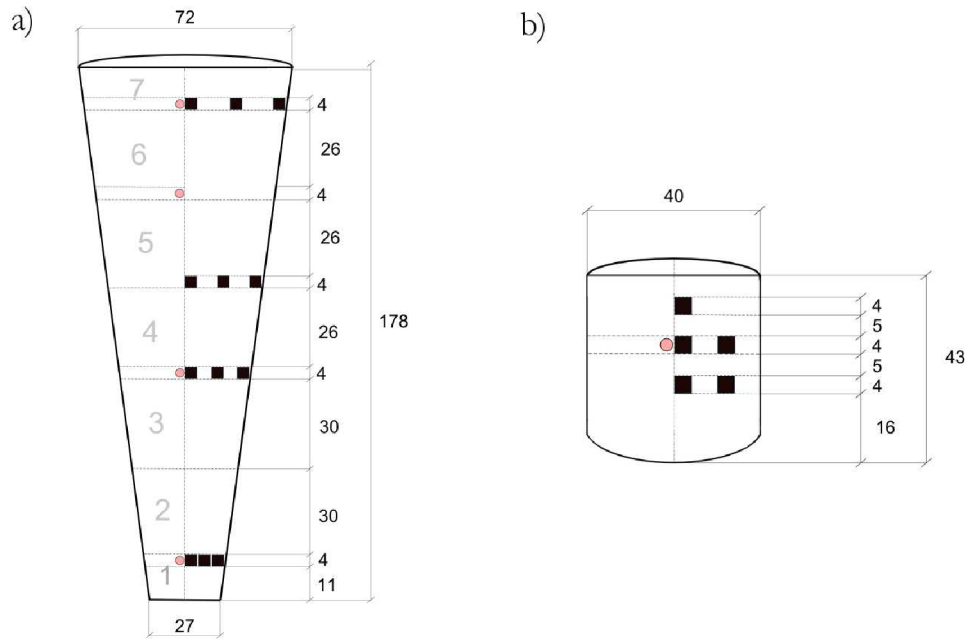


Fig. 2.4: A schematic drawing illustrating positions of samples for oxygen analysis (black squares) and for DSC analysis (red circles) in a ingot (a) and in a re-molten ingot (b). Corresponding dimensions are in mm.

annealing at 850 °C for 1.8 ks in air. DSC samples were taken from bulk (avoiding possible surface effects) of the heat-treated and quenched cylinders as schematically shown in Figure 2.5. Each of the DSC samples was cleaned using a similar procedure as outlined for the cylinders in the Section 2.3.

The differential calorimetry signal of the DSC samples was acquired using the calorimeter NETZSCH DSC 204 F1 Phoenix®. The mass of individual DSC samples was between 25 and 45 mg. DSC cycles consisted of cooling and heating parts where cooling and heating rates were chosen as 10 °C/min. The cooling and heating semi-

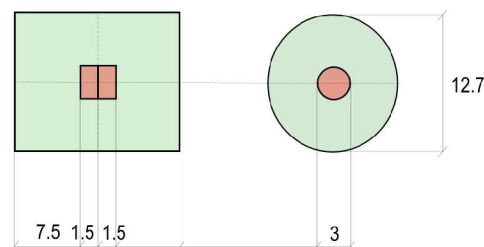


Fig. 2.5: A schematic drawing that illustrates position of DSC samples (red areas) in the heat treated and quenched cylinders. Corresponding dimensions are in mm.

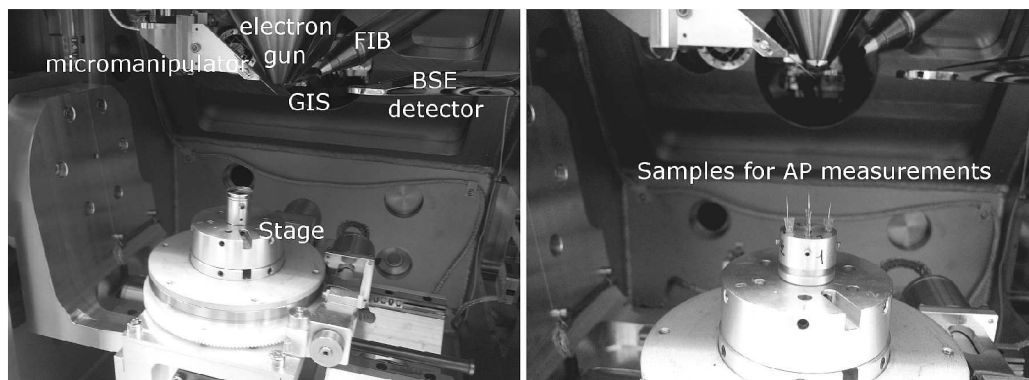


Fig. 2.6: Inside view of the scanning electron microscope Tescan SEM/FEG LYRA 3 XMU with the focus ion (Ga^{3+}) beam, a gas injection system (GIS), a micromanipulator, bellow sample holder and backscattered electron (BSE) detector.

cycles were finalized by isothermal segments at lowest and highest temperature of the cycle. In the isothermal regime, samples were kept at constant temperature for 3 or 5 minutes. Program NETZSCH Proteus® was used to process the measured DSC data.

2.4.3 Scanning electron microscopy

Atome probe sample was prepared by using scanning electron microscope Tescan SEM/FEG LYRA 3 XMU with the focus ion (Ga^{3+}) beam and with a gas injection system (GIS) (Fig. 2.6). Built-in energy-dispersive (EDS) detector D.1028 Oxford Instruments was used to perform the local chemical analysis of the individual phases presented in the alloys.

2.4.4 Transmission electron microscopy

TEM technique was employed in order to assess microstructural changes associated with heat-treatments. TEM observations were performed using the DSC samples as a starting material for grinding and polishing of TEM foils. The DSC samples were mechanically polished with 500, 600, 800, 1000 and 1200-grit emery paper down to a thickness of about $120\ \mu\text{m}$ and, finally, electro-polished using electrolyte AS-I from Struers®. TEM foils from DSC samples offer a unique possibility to characterize simultaneously microstructure and corresponding transformation behavior. The electro-polished TEM samples were examined in a Philips CM12 operating at 120 kV. Additional TEM studies of martensitic transformation in some of these samples were performed by using a FEI Tecnai F20 microscope operating at 200 kV.

This facility was kindly made available by the Department of Materials Science RU-Bochum. Obtained diffraction patterns were processed by ACC32 Image Analyser software.

2.4.5 Neutron diffraction measurements

Neutron diffraction experiments were performed by using the standard neutron powder diffraction instrument MEREDIT (Medium Resolution Neutron Powder Diffractometer) in Nuclear Physics Institute of the Academy of Science of the Czech Republic in Rež. The data were collected from the cylinders (see Fig. 2.5 and 2.3 b) at temperature around 65 °C. The cylinders were sliced by spark erosion into quarters and sealed in different orientations to attenuate texture effect. Higher temperature was chosen in order to avoid any martensitic phases such that only B2 reflections characterized the matrix background structure. The data were collected in one 2θ scan ranging from 4 to 144° with an angular step size of 0.08° and a collection time of 1040 s per one angular step. Neutrons with wavelength 0.146 nm were selected by employing copper mosaic crystal as a monochromator. Program Full Prof was used for the refinement of the diffraction patterns.

2.4.6 3D Atom probe analysis

AP analysis was performed using IMAGO local electrode atom probe (LEAP) microscope at the Department of Physical Metallurgy and Materials Testing MU-Leoben (Fig. 2.7). The AP analysis was used to detect hydrogen atoms and their localization in B2 lattice. Samples for AP measurements must be shaped into the form of sharp needles. These shapes were achieved in one-step process which involved chemical etching or using a lift-out technique [70, 71] .



Fig. 2.7: IMAGO LEAP microscope and AP needle-shaped samples.

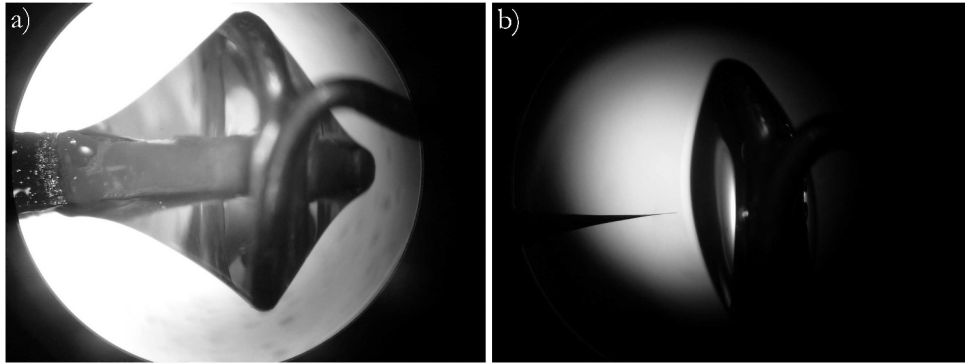


Fig. 2.8: An anodic sample situated within a gold ring-shape cathode: a) at the beginning and b) at the end of electro-chemical etching process [72].

Electro-chemical etching

Before electro-chemical etching, samples with dimensions 1x1x10 mm were spark-cut from the heat-treated cylinders. The samples were then mechanically polished and ultrasonically cleaned in ethanol. The cleaned samples were mounted into cooper bolts, held in steel tweezers and connected as an anode in a movable holder. A cathode was formed by a small wire ring made of gold (see Fig. 2.8). An etchant consisting of acetic and sulphuric acid was used as a starting solution. A final etching

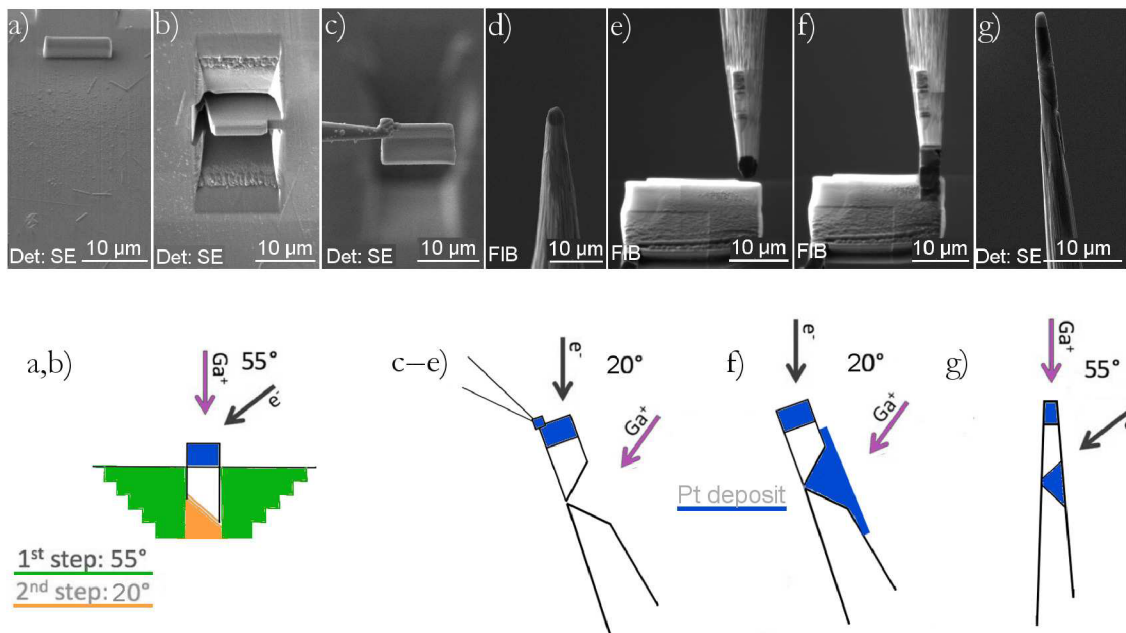


Fig. 2.9: AP-sample preparation using lift-out technique (see text for details) [71].

was performed in a solution with lower content of sulphuric acid. Short voltage pulses ranging from 20 to 10 V were applied to prepare a single sharp tip. The electrochemical etching was done in the department MU-Leoben and also described in the thesis [72] together with ion milling technique.

Ion milling technique

Lift-out technique was specifically used for AP sample preparation to avoid a shape change of the sharp tip induced during the cooling of sample down to the AP operating temperature. The lift-out technique was also based on the SEM operations (see Section 2.4.3). Surfaces of DSC samples were mechanically polished and ultrasonically cleaned in ethanol. A small area (around $2 \times 10 \mu m$) located the middle of on sample surface was marked and covered by wolfram layer to prevent AP samples from damage by the high-energy ion beam in the following milling procedure (see Fig. 2.9 a). After milling (tilt 55°) and cutting (tilt 20°) the lamella-shaped sample (see Fig. 2.9 b and c), a micromanipulator was welded to the top of the thin film by platinum deposition [70]. The cut-out sample was then lift out and placed to the pre-shaped wolfram needle with its tip cut off (top with a diameter of $1 \mu m$) (Fig. 2.9 d and e). More than one AP sample can be placed onto a needle, a particular number depends on the length of an extracted lamella. Appropriate bonding of the AP sample to the needle was again provided by the platinum deposition (Fig. 2.9 f). The final annual shaping steps of the sample were performed with decrea-

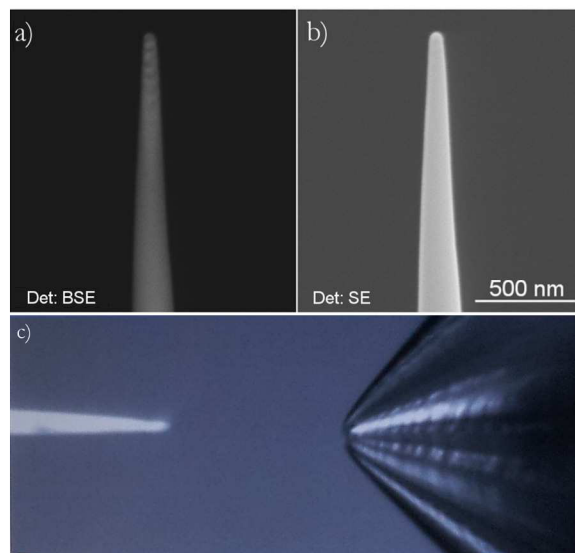


Fig. 2.10: Final-shape of a tip (a,b) and inside view of the IMAGO LEAP microscope (c).

sing milling current (Fig. 2.9 g). Finally, the sharp tip with a diameter of less than 100 nm (tip radius around 10°) was obtained (Fig. 2.10).

Final-shape of the tips was documented by SEM. AP measurements were performed at cryogenic temperature between 60 and 80 K under ultra high vacuum (10^{-12} Pa). A voltage mode with a pulse 200 and 100 kHz (10PF) was used. The operating conditions have still not been optimized. All chemical species are identified by the time-of-flight detector leading to a mass spectrum of atoms and/or molecules within the analyzed volume.

3 RESULTS

3.1 Alloys melted in Y_2O_3 crucible

3.1.1 Contamination by oxygen

Oxygen content

The content of oxygen in the cast $Ni_{50.8}Ti_{49.2}$ alloys is displayed in a bar chart shown in Figure 3.1. The chemical analysis accounts for the overall oxygen content and does not allow for the differentiation between oxygen in solution and oxygen associated with a oxygen phase. Two columns have been stacked up in the chart (Fig. 3.1): one represents a calculated amount of oxygen contained in the melting batches (black columns) and second characterizes a variable increase of the oxygen concentration during the melting procedure (white columns). The starting level of 1123 atomic ppm is always the same and describes the amount of oxygen measured in the raw materials composing the melting stock, 49.2at% titanium and 50.8at% nickel (Table 3.1). The average values of the oxygen content as detected at the end of the melting experiments are based on 12 measurements (Section 2.4.1) and summarized in Table 3.1. The highest final oxygen concentration (4421 atomic ppm) was found in the cast alloy A (melted by procedure marked A, Section 2.2). The lowest oxygen content (3226 atomic ppm) was measured in the cast alloy B. Oxygen pick up during melting procedure B resulted in about triple increase of the initial oxygen level (column B in Fig. 3.1). The difference between the lowest and the highest contamination level equals to 1195 atomic ppm and between these extreme

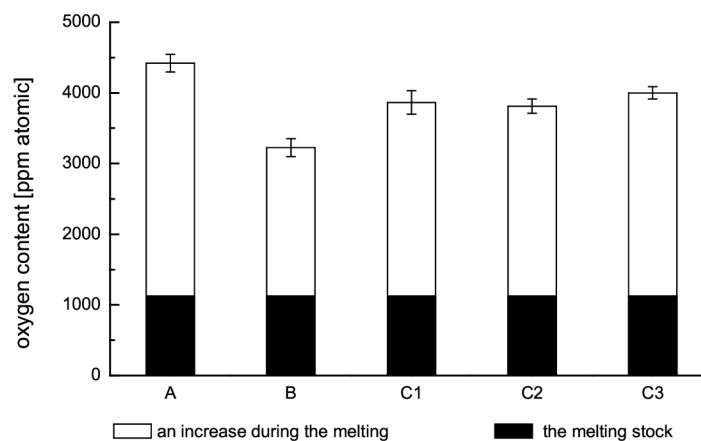


Fig. 3.1: The column chart displays the content of oxygen in the cast alloys (see text for details).

values all three cast alloys C exhibit oxygen content. Figure 3.2 shows the analyzed ingots obtained in the five different melting experiments.

Tab. 3.1: The oxygen content (atomic ppm) in the raw materials and the alloys after melting and solidification.

Ni	Ti
41 ± 7	2239 ± 563

cast alloy A	cast alloy B	cast alloy C1	cast alloy C2	cast alloy C3
4421 ± 125	3226 ± 127	3864 ± 163	3814 ± 100	4000 ± 87

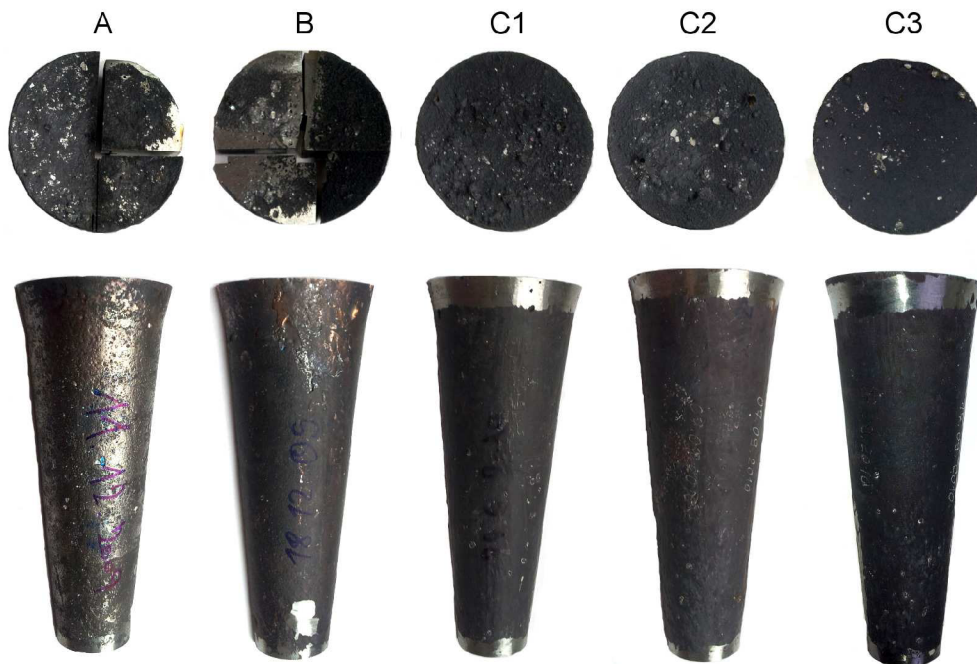


Fig. 3.2: The cone shaped ingots of 30 (bottom) and 70 (top) mm in diameter and 180 mm in length. The ingot melting route is given using capital letters.

Transformation behavior

Figure 3.3 shows an example of the transformation behavior for the cast alloys A and B. These alloys have been chosen to compare the transformation features of microstructures containing the highest and the lowest amount of oxygen. The DSC charts were recorded for annealed samples that were taken from different positions

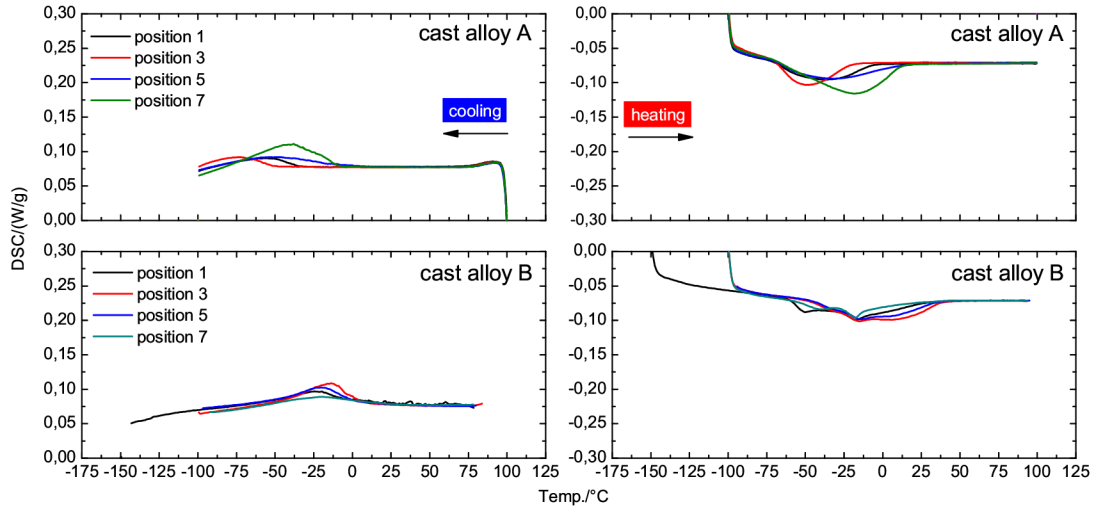


Fig. 3.3: DSC charts of the cast alloys A and B. Samples taken from different positions along the ingot axis were investigated.

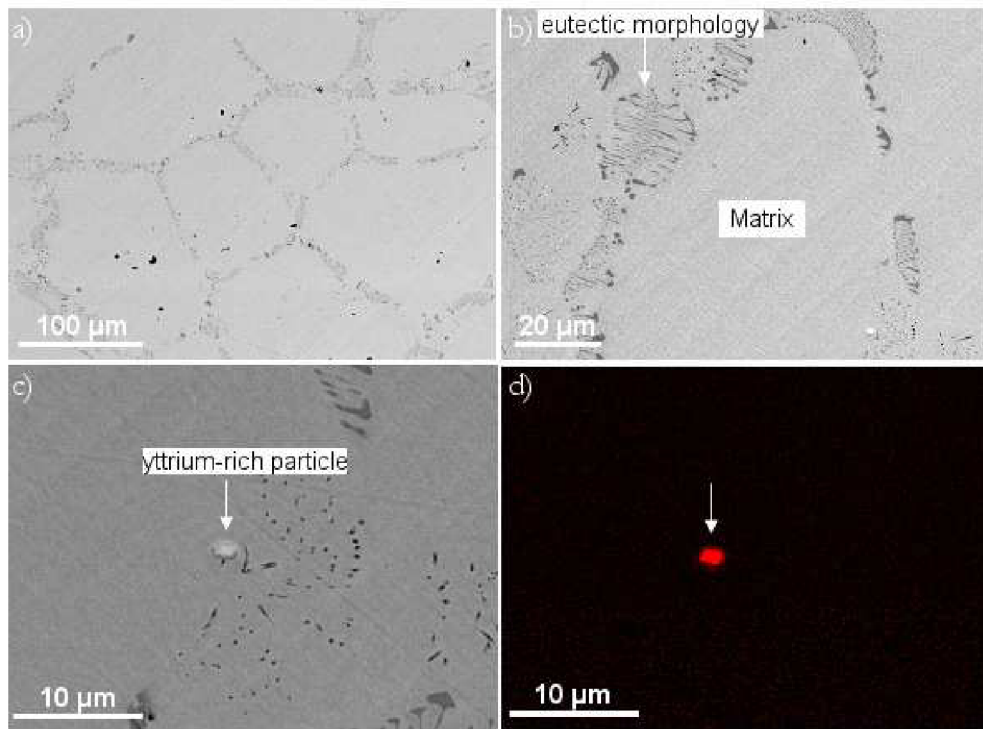


Fig. 3.4: (a,b) Microstructure of the DSC sample taken from an annealed piece (position 5) of ingot B. The images were obtained by means of SEM in BSE contrast mode. (c,d) The detail of a white particle in BSE contrast (c) and in X-ray 'dot' distribution map (d) (yttrium L_{α}).

along the axis of castings, see Figure 2.4. Both alloys A and B exhibit only very limited martensitic transformation. Microstructure of the annealed sample taken from the position 5 (see Fig. 2.4) of the cast alloy B is shown in Figure 3.4. Darker regions correspond to a phase with higher content of titanium. Areas with eutectic morphology formed by the Ti_2NiO_x phase [73] are distributed near grain boundaries in the NiTi matrix (Fig. 3.4 b). As was investigated by Frenzel et al. [50], formation of Ti_2NiO_x precipitates is related to oxygen pick-up during solidification. Melt possess some solubility for oxygen, whereas in solid NiTi oxygen are almost not soluble. Figures 3.4 c and d show an yttrium-rich particle coming from the yttria crucible. This particles are distributed at random throughout the whole volume of cast alloys.

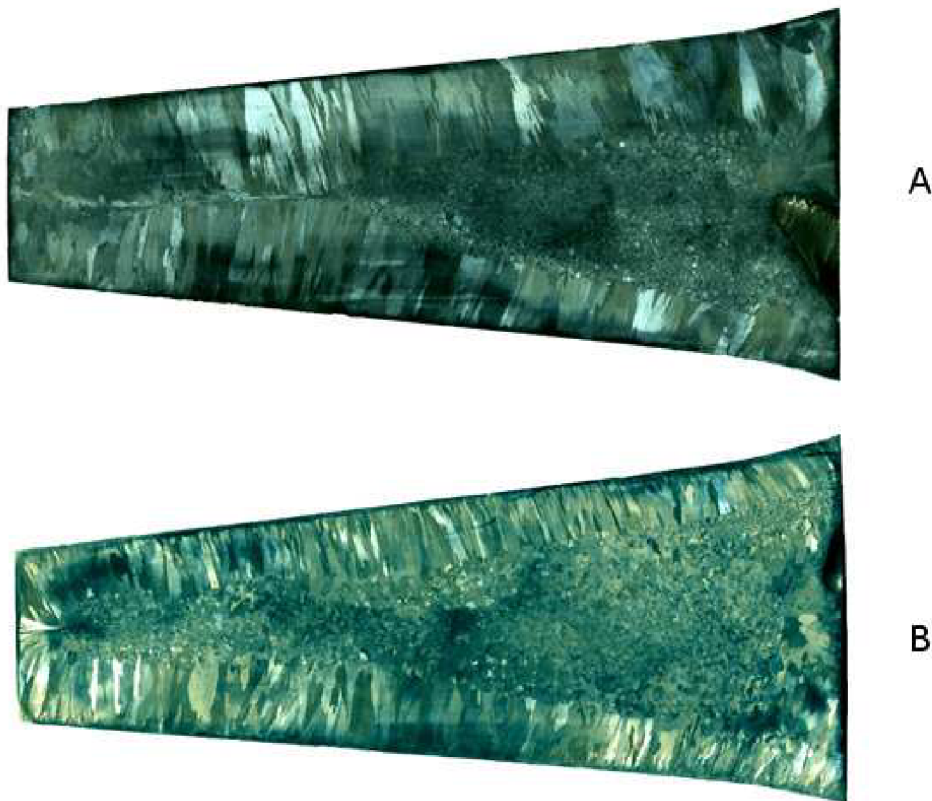


Fig. 3.5: Macrostructures from the ingots A and B.

As-cast microstructure and rise of temperatures

Macrostructures from solidified ingots A and B are shown in Figure 3.5. The ingots A and B differ with respect to extent of regions with columnar grains. It is commonly accepted that the size of the columnar microstructure depends on the pouring temperature and this is in line with the measured temperatures for ingots A and

B (Tab. 3.2). The higher the pouring temperature, the more extensive region with clumnar grains. We expect that higher melting temperatures in our experiments resulted in corresponding higher pouring temperatures. The melting temperatures in second melting step are given in Table 3.2.

Tab. 3.2: The start and the rise of temperatures ($^{\circ}C$) when the remainder of nickel was added in second melting step.

First step		
cast alloy A	cast alloy B	cast alloys C1 C2 C3
≈ 1450	≈ 1060	≈ 942
Second step		
cast alloy A	cast alloy B	cast alloys C1 C2 C3
≈ 1800	≈ 1440	≈ 1400

Holding time and temperature

The change of oxygen content in the $Ni_{50.8}Ti_{49.2}$ alloy during the re-melting experiments in yttria crucibles is illustrated in Figure 3.6. A data point obtained from the bulk of the ingot re-melted for 20 min at $1500^{\circ}C$ is not included due to a failure of the

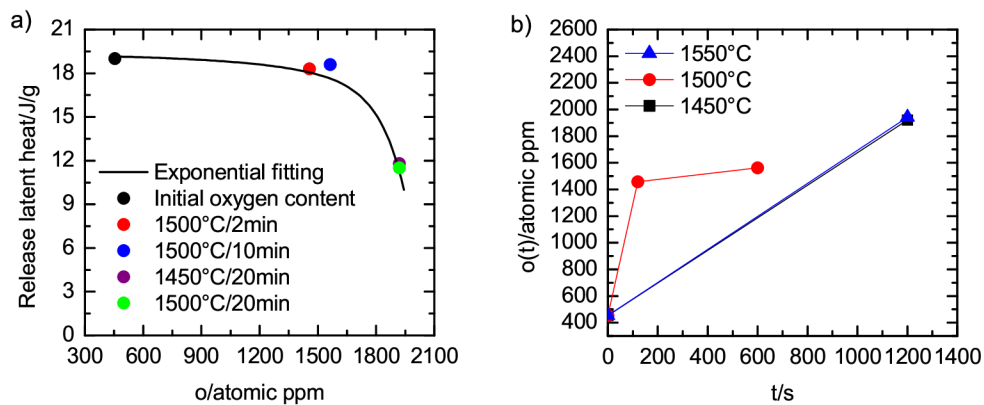


Fig. 3.6: (a) The variation of the release latent heat associated with martensitic transformation from $B2 \leftrightarrow B19'$ in the re-molten alloys with oxygen content at different melting temperatures and holding times. (b) Result of the chemical analysis showing increase of oxygen content in re-molten alloys at 1450, 1500 and $1550^{\circ}C$ after different reaction times.

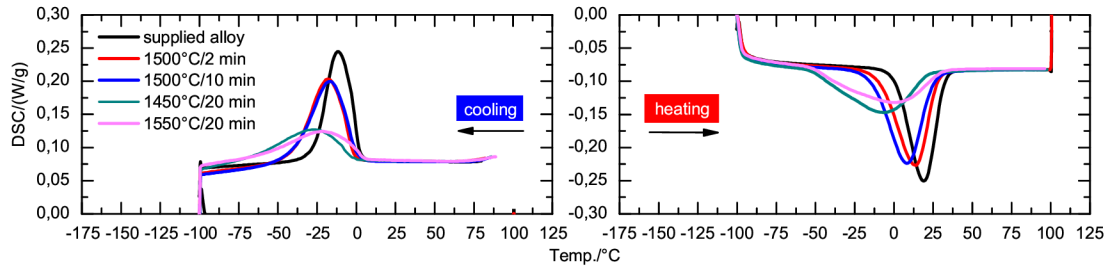


Fig. 3.7: DSC charts of the supplied and re-molten alloys at different melting temperatures and holding times.

Y_2O_3 coated cermet sheath and its partial dissolution in the molten alloy. Figure 3.7 shows transformation behavior of the alloy after the re-melting experiments.

The latent heat decreases exponentially with oxygen content in Figure 3.6 a. It can be seen that martensitic transformations are efficiently suppressed when the oxygen content in the $\text{Ni}_{50.8}\text{Ti}_{49.2}$ alloys exceeds 1900 atomic ppm (Fig. 3.7 a). Figure 3.6 b shows that the impurity content increases significantly during re-melting for 2 min at 1500 °C. The content of oxygen becomes triple the initial oxygen level and does not too differ from the re-melting experiment carried out at the same mel-

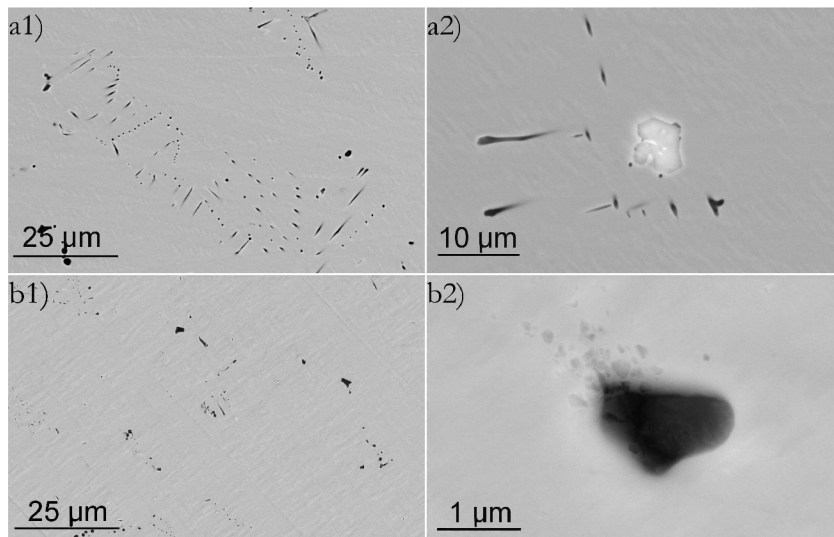


Fig. 3.8: Microstructure of the DSC samples taken from the alloy after re-melting for 2 min at 1500 °C (a) and the supplied alloy (b). (2) The SEM images at higher magnifications show Y_2O_3 (white) and Ti-rich (dark) phases (a2), and a small TiC particle (b2) in NiTi matrix. The images were obtained by means of SEM in BSE contrast mode.

ting temperature but with 10 min of holding time. Increasing to about quadruple the initial oxygen level during re-melting for 20 min at $1450^\circ C$ does not vary with the melting temperature higher by $100^\circ C$. The oxygen content and release latent heat of martensitic transformation in re-molten alloys are summarized in Table 2.5 of Section 2.2 and in Table A.1 of the Appendix A.1. Microstructure of the DSC samples taken from the alloy after re-melting for 2 min at $1500^\circ C$ and the supplied alloy is shown in Figure 3.8. The re-melted material shown in Figure 3.8 a contains more inclusions than the supplied material in Figure 3.8 b. The inclusions in Figure 3.8 a are Ti-rich phase (Ti_2NiO_x , $TiC(O)$ and TiC [74]) and Y_2O_3 particles, while the inclusions shown in Figure 3.8 b represent mainly carbides TiC .

3.1.2 $Y_2O_3/ Ni_{50.8}Ti_{49.2}$ interface

Wetting of Y_2O_3 crucible

Figure 3.9 a illustrates a photograph of the yttria crucible bottom after re-melting for 10 min at $1500^\circ C$. During melting liquid droplets wet surface of Y_2O_3 crucible (gray area in Fig. 3.9 a). Figure 3.9 a shows that the depth of penetration can exceed about 6 mm on the bottom of Y_2O_3 crucible. In those re-molten $Ni_{50.8}Ti_{49.2}$ block allowed to solidify inside the crucible, there was a discontinuous layer of yttrium oxide grains at the surface. This yttrium oxide layer was adhere to the metal. Figure 3.9 b shows area at the surface of the block after re-melting for 10 min at $1500^\circ C$ in Y_2O_3 crucible containing Y_2O_3 particles.

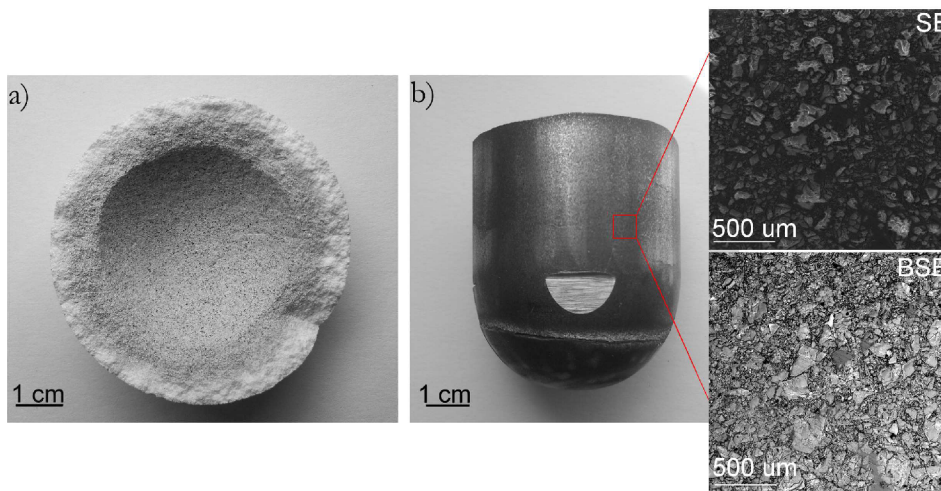


Fig. 3.9: (a) The bottom of Y_2O_3 crucible. (b) $Ni_{50.8}Ti_{49.2}$ block after re-melting for 10 min at $1500^\circ C$ in Y_2O_3 crucible, and SEM and SEM back-scatter micrographs of detail of surface of the block containing Y_2O_3 particles.

Phase analysis

Figure 3.10 shows examples of SEM back-scatter micrographs taken from the interface region between yttria crucible and $\text{Ni}_{50.8}\text{Ti}_{49.2}$ alloy. The Ti-rich phases (dark-gray) presented in detail in Figure 3.10 b) was formed at the $\text{Y}_2\text{O}_3/\text{NiTi}$ interface. The Ti-rich phase does not form compact layer. Figure 3.10 b) also exhibits some insoluble Y_2O_3 particles entering into the melt.

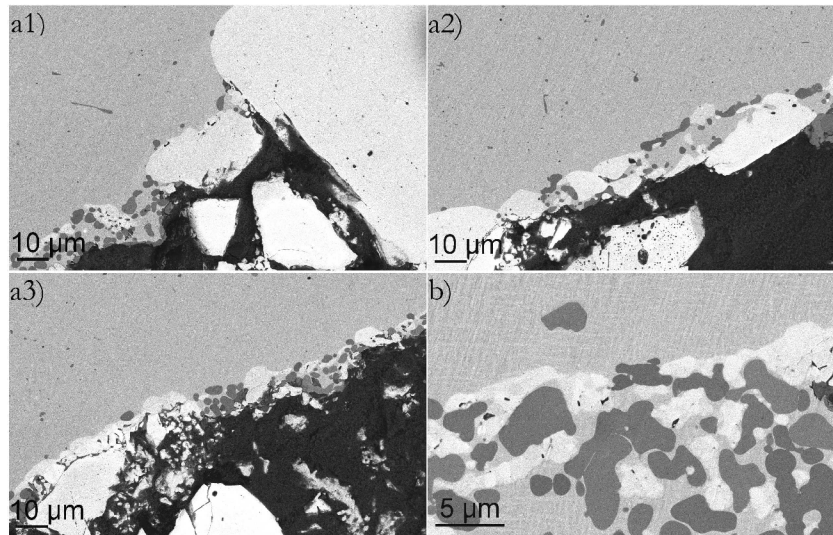


Fig. 3.10: SEM back-scatter micrographs of the interface region between the Y_2O_3 crucible (white phase below) and the $\text{Ni}_{50.8}\text{Ti}_{49.2}$ alloy (bright-gray phase above) after re-melting for 20 min at 1450°C . The dark-gray phase in between represents Ti-rich phase.

3.2 Heat treatments in controlled atmospheres

3.2.1 Influence of the quenching rate

Example of impact of hydrogen on the martensitic transformation in the sealed sample received the Regime I treatment in pure hydrogen and its capsule was open after quenching step is shown in Figure 3.11 (the DSC chart labeled by slow). This impact of hydrogen dismiss when the capsule is opened in water during quenching step (see the DSC chart labeled by fast in Fig. 3.11). In order to examine the impact of hydrogen, capsules were open only after final quenching (Section 2.3). Helium atmosphere was chosen as additional filling-up gas to avoid effect of cooling rate on quenched microstructure in the hydrogen-helium mixtures heat treatment

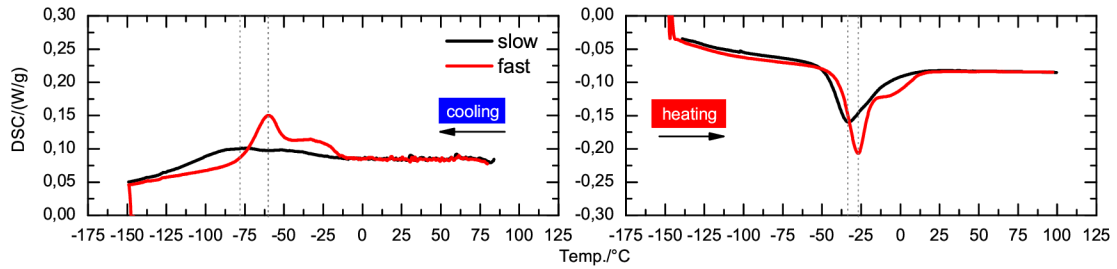


Fig. 3.11: DSC charts of the $\text{Ni}_{50.8}\text{Ti}_{49.2}$ alloys heat treated in Regime I in 900 mbar of hydrogen. (Fast) the capsule was opened during quenching, in the quenching water, or (slow) after quenching, out of quenching water. Sample temperature equaled to room temperature.

experiments. Because thermal conductivities of hydrogen and helium gases shows similar values, compared to argon (see Tab. 3.3).

Tab. 3.3: The coefficient of thermal conductivity of gases at 0°C and 1 atm (1.01325 bar) [29].

gas	H_2	He	Ar
κ [$\text{JK}^{-1}\text{m}^{-1}\text{s}^{-1}$]	$16.82 \cdot 10^{-2}$	$14.42 \cdot 10^{-2}$	$16.3 \cdot 10^{-3}$

3.2.2 Impact of heat treatments in the Regime I and II on the martensitic transformation

Air and inert gases

Figure 3.12 shows DSC charts of the $\text{Ni}_{50.8}\text{Ti}_{49.2}$ alloy which was subjected to heat treatments in the Regime I in air and two inert gases, argon and helium. After heat treatment in Regime I, the alloy transforms between B2 austenite and B19' martensite in one step corresponding to one peak recorded on both, the cooling and heating DSC curves. There is no markable difference between samples annealed in air or in the two inert gases. The "knee" signal associated with DSC peaks on cooling and heating, see Figure 3.12, represents a premature transformation (probable transformation between B2 and R-phase) due to inhomogeneities of the received rod microstructure. The most likely reasons are either an inhomogeneity of the grain structure or a remnant dislocation density. After manufacturing, the remnant dislocation density was organized into low angle dislocation boundaries which favored

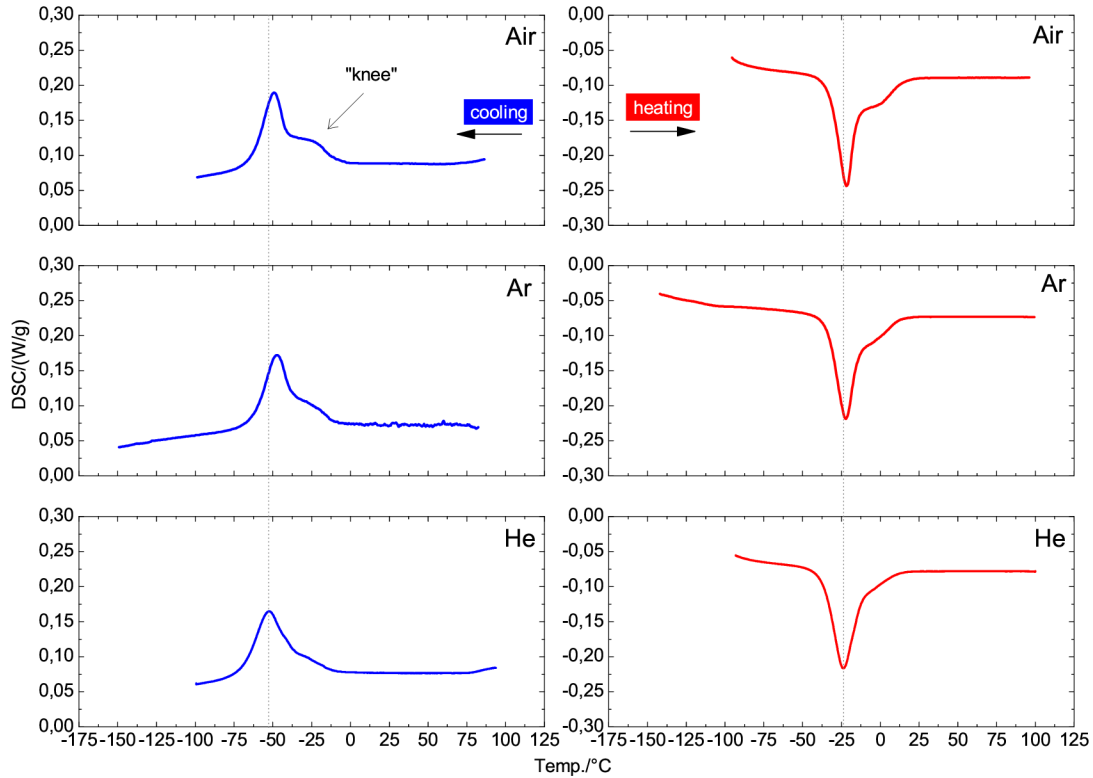


Fig. 3.12: DSC charts of $\text{Ni}_{50.8}\text{Ti}_{49.2}$ alloy after the Regime I heat treatments in air, argon and helium.

the premature transformation to R-phase. These inhomogeneities are a relic of an unoptimized rod processing and cannot be easily corrected by an additional heat treatment.

Transformation behavior recorded using DSC after heat treatments in the Regime II is shown in Figure 3.13. The reference samples (heat treated in inert gases) transform in two steps corresponding two transformation peaks $\text{B2} \leftrightarrow \text{R}$ and $\text{R} \leftrightarrow \text{B19}'$. A distinctly different transformation is observed for the alloy heat treated in air. Here the transformation splits into three peaks (steps) on cooling. The first transformation step on the cooling chart corresponds to transformation from B2 to R-phase (small thermal hysteresis). Other two steps represent transformations the product phase of which is the B19' martensite phase. Temperature regimes which provide thermodynamic stability for the individual phases are accordingly described in Figure 3.13. The characteristic temperatures and latent heats associated with the particular steps are summarized in Table A.2 and A.3 of the Appendix A.1.

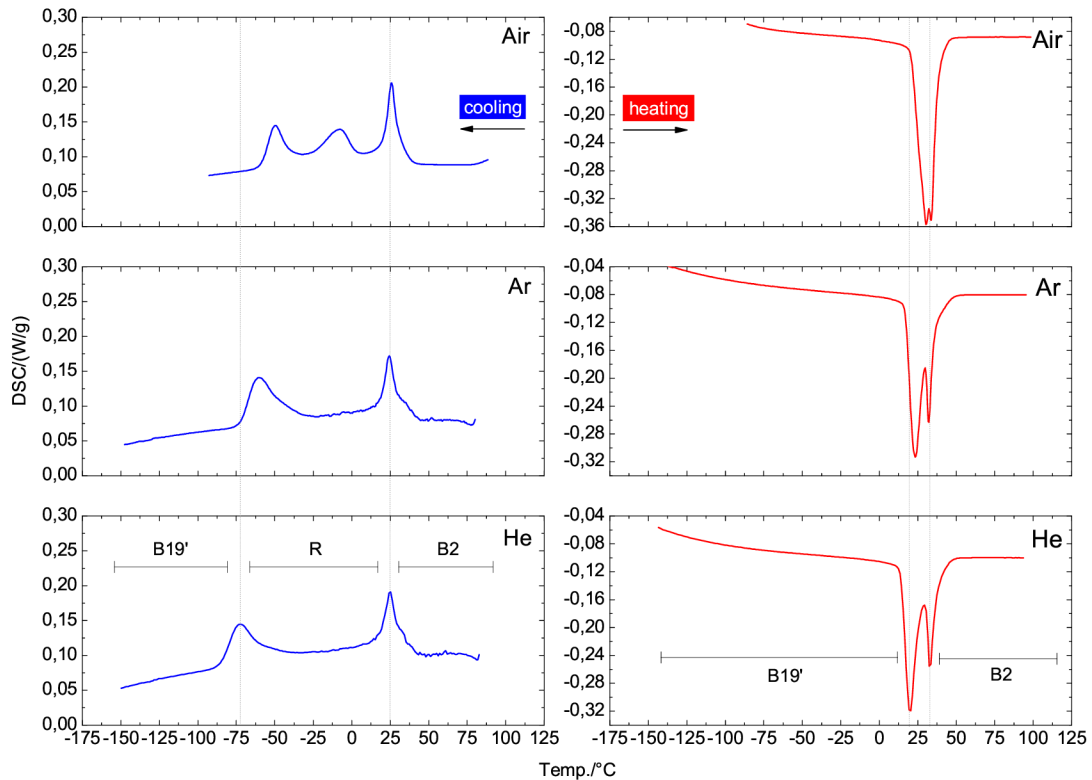


Fig. 3.13: DSC charts of the $\text{Ni}_{50.8}\text{Ti}_{49.2}$ alloy after the Regime II heat treatments in air, argon and helium.

Oxygen, nitrogen and hydrogen

DSC charts of the $\text{Ni}_{50.8}\text{Ti}_{49.2}$ samples that were separately heat treated in Regime I in oxygen, nitrogen or hydrogen are shown in Figure 3.14. The purity of the employed gases was given in the Section 2.3. Results presented in Figure 3.14 suggest that there are no significant differences in the transformation behavior after heat treatments in oxygen, nitrogen and the reference inert gases. In contrast, the heat treatment in Regime I in hydrogen markedly suppresses the overall transformation process and results in the extended interior DSC peaks (Fig. 3.14 and the Appendix A.1). In the same time, the position of the transformation peaks is shifted towards lower temperatures. This suggests that austenite B2 lattice (containing hydrogen) becomes more stable with respect to the B19' martensite lattice dissolving the same amount of hydrogen.

Figure 3.15 shows the DSC charts of samples heat treated in Regime I in pure hydrogen that were kept at 200 °C for 1.8 or 3.6 ks during DSC analysis. The peaks slightly shifted towards lower temperatures.

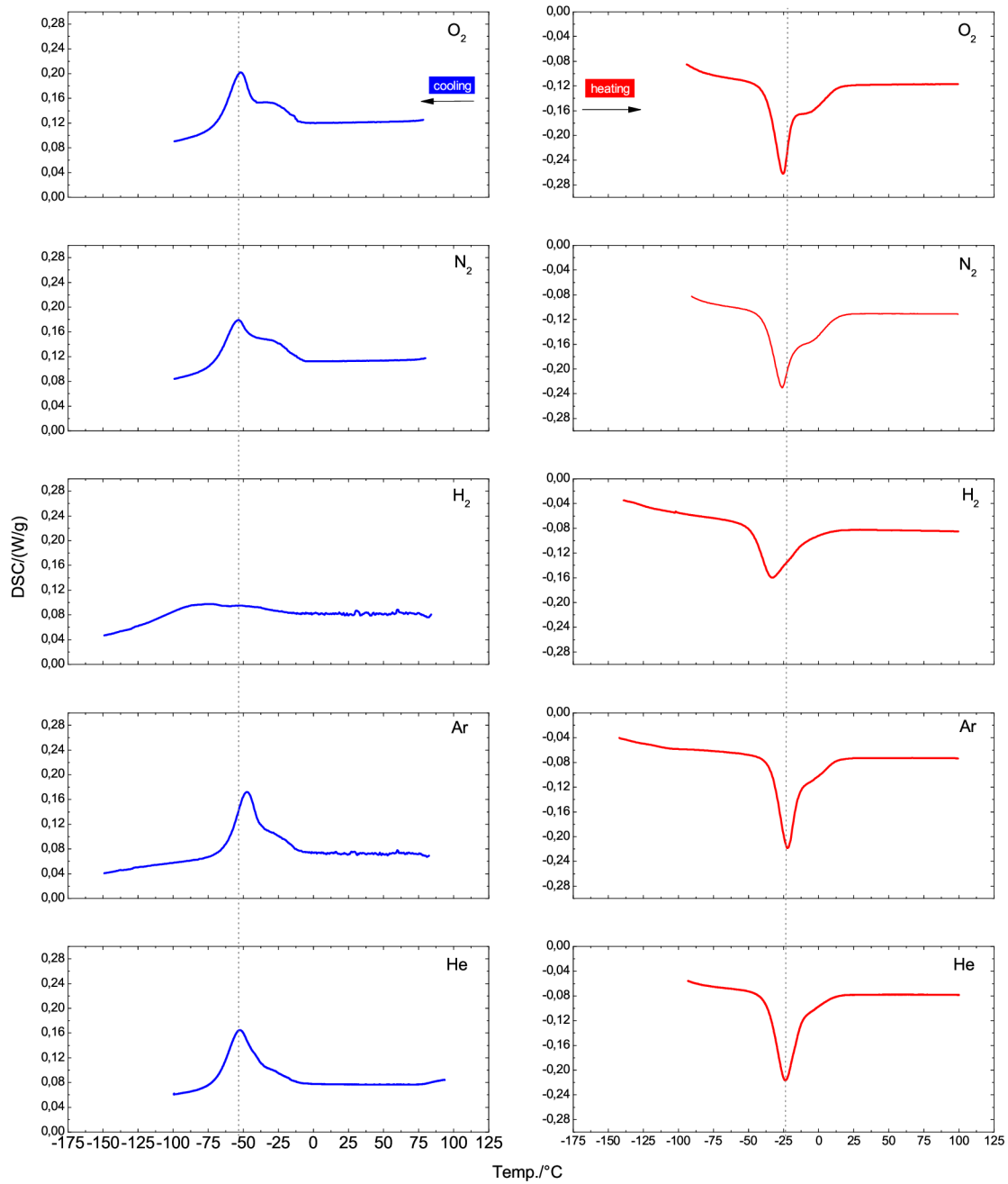


Fig. 3.14: DSC charts of the Ni_{50.8}Ti_{49.2} alloy after the Regime I heat treatments in either oxygen, nitrogen, hydrogen or in the reference inert gases - argon or helium.

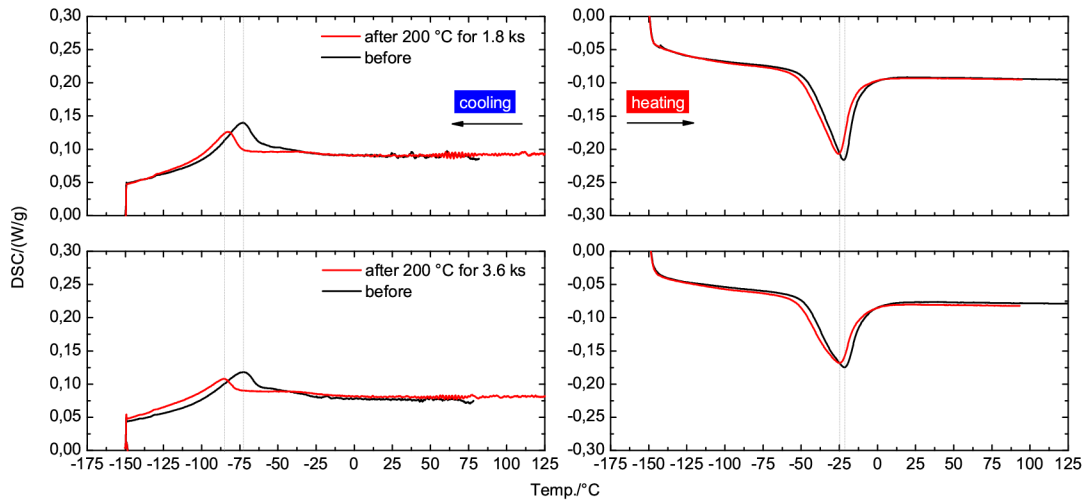


Fig. 3.15: DSC charts of the $\text{Ni}_{50.8}\text{Ti}_{49.2}$ samples heat treated in Regime I in pure hydrogen and hold at 200 °C for 1.8 or 3.6 ks between the two DSC analysis.

Hydrogen-helium mixtures

Figure 3.16 shows transformation behavior of the $\text{Ni}_{50.8}\text{Ti}_{49.2}$ samples heat treated in the Regime I in hydrogen and helium mixtures with the constant overall filling pressure of 900 mbar. With the increasing partial pressure of hydrogen, the one-step martensitic transformation ceases (Fig. 3.16a and b). A partial pressure of hydrogen,

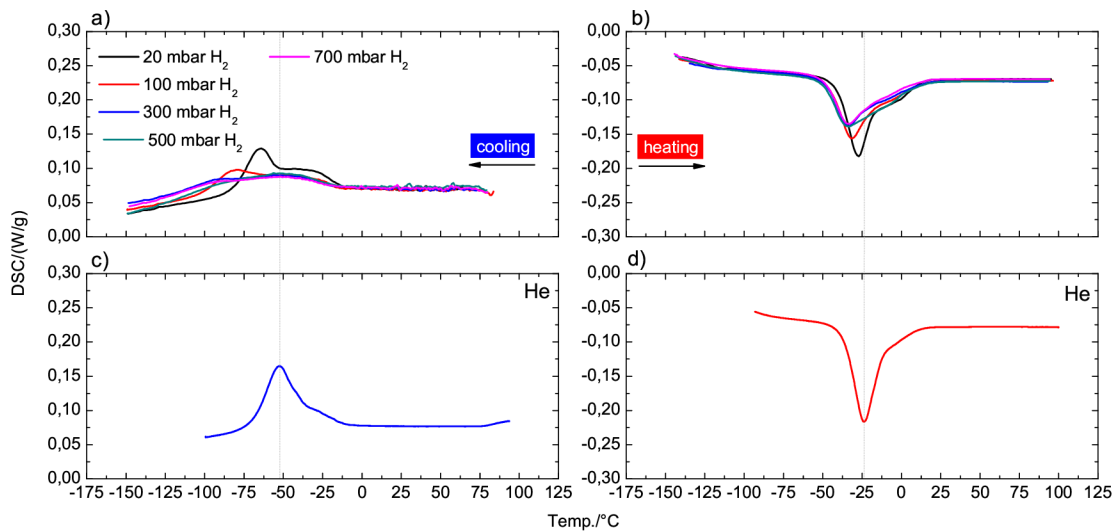


Fig. 3.16: DSC charts of the $\text{Ni}_{50.8}\text{Ti}_{49.2}$ samples heat treated in the Regime I in either hydrogen-helium mixtures (H_2 partial pressure 20, 100, 500 and 700 mbar) or in the reference helium atmosphere.

which assisted the particular heat treatment, is indicated in Fig. 3.16a. A pronounced drop in the peak heights occurs at the hydrogen partial pressure exceeding 100 mbar.

Transformation behavior of the samples that were heat treated in the Regime II using the same gas mixtures is shown in Figure 3.17. The samples aged under the presence of hydrogen exhibit, in principle, the same transformation sequence as the samples aged in the reference inert gases. However the second transformation step, which corresponds to $R \leftrightarrow B19'$ transition, is markedly suppressed. A quantitative assessment of the corresponding latent heats evolved or absorbed during the $R \leftrightarrow B19'$ transformation yielded and data shown in Table A.6 of the Appendix A.1.

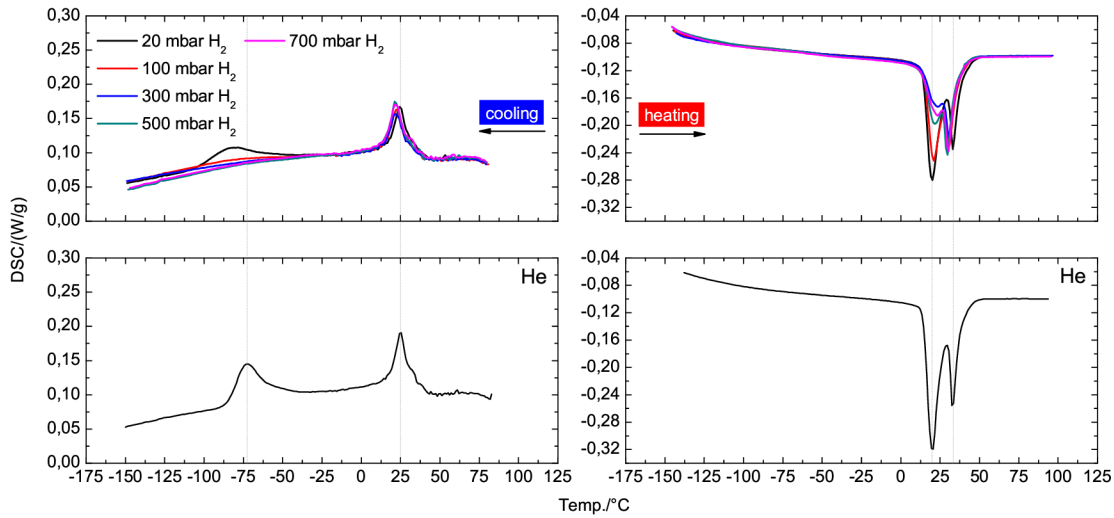


Fig. 3.17: DSC charts of the $\text{Ni}_{50.8}\text{Ti}_{49.2}$ samples that were heat treated in the Regime II in hydrogen-helium mixtures (H_2 partial pressure 20, 100, 500 and 700 mbar) or in the reference helium atmosphere.

3.2.3 Impact of heat treatments in Regime I on microstructure: presence of impurities

Hydrogen

Selected area diffraction (SAD) analysis revealed that the conventional SAD patterns exhibited pronounced modulations of the background electron intensity. Examples are presented in Figure 3.18, where $[111]_{B2}$, $[100]_{B2}$, $[110]_{B2}$ and $[210]_{B2}$ zonal SAD patterns are shown. These patterns are compared to similar SADs from material states formed during annealing in the inert gas only (with zero partial pressure of hydrogen). After the inert gas treatment, only $[100]_{B2}$ and $[110]_{B2}$ patterns show mild modulations of the background electron intensity (marked by red arrows). However,

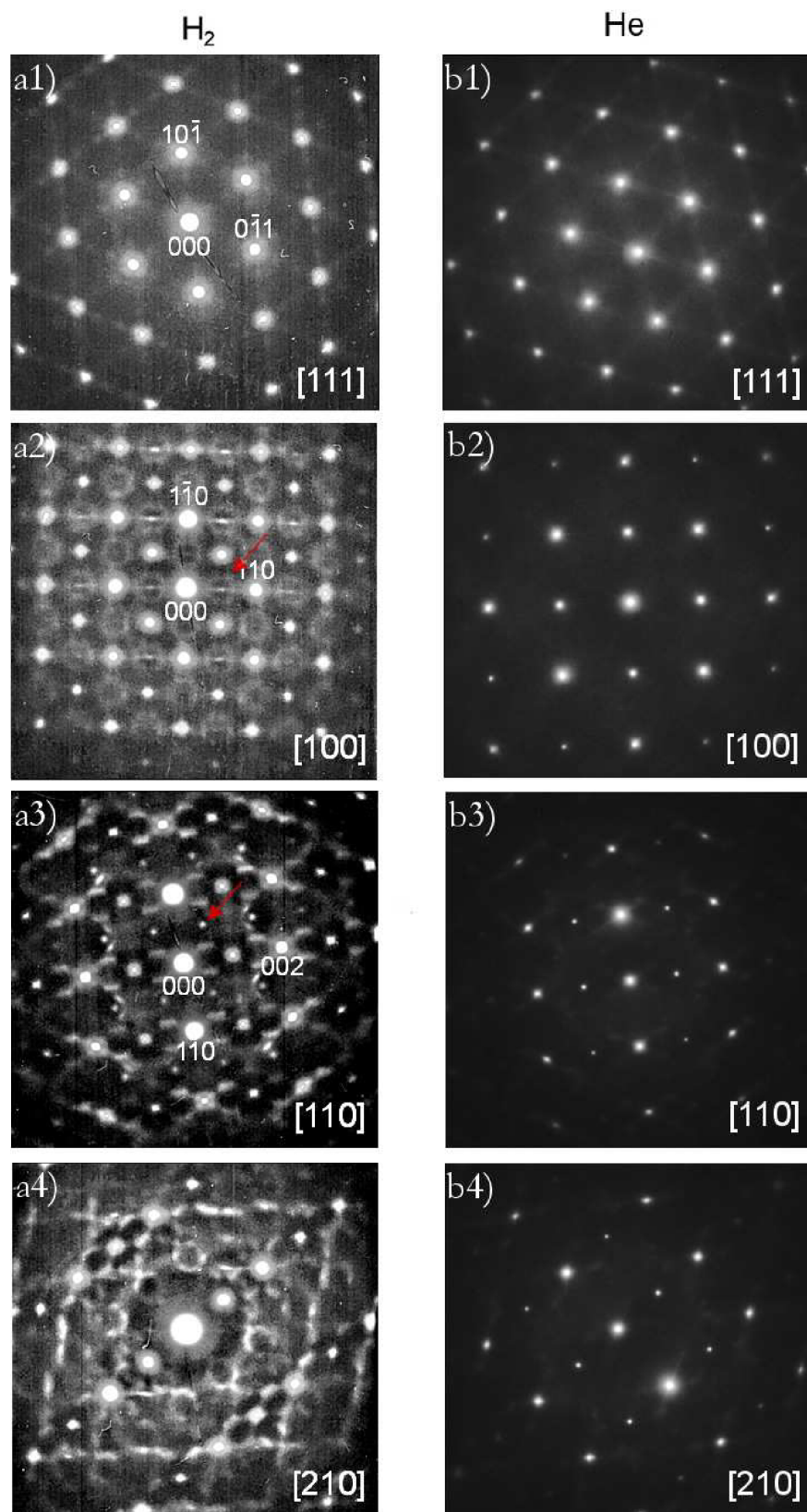


Fig. 3.18: SAD patterns of the quenched $Ni_{50.8}Ti_{49.2}$ alloy taken in the zones $[111]_{B2}$, $[100]_{B2}$, $[110]_{B2}$ and $[210]_{B2}$. The patterns were obtained after heat treatment in Regime I in hydrogen (a1–4) or reference helium atmosphere (b1–4).

the amplitude of these modulations is weak. In contrast, the SAD patterns, which illustrate the diffracted intensity from the sample subjected to Regime I in 900 mbar of hydrogen, reveal regular modulations of the diffuse electron intensity.

Hydrogen mixtures

Figure 3.19 shows examples of the $[110]_{B2}$ zonal SAD patterns taken after Regime I heat treatments in hydrogen-helium mixtures. With the increasing partial pressure of hydrogen in the heat treatment atmosphere from 300 to 900 mbar, the mild background electron density modulations become more pronounced (Figs. 3.19 a–d). It should be underlined again that the $B2 \leftrightarrow B19'$ martensitic transformation is suppressed in all these structures. This has been clearly documented by DSC charts presented in Figure 3.16.

Figures 3.20 a and b show a 3D atom probe tomography (APT) elemental maps (each dot represents one atom) of a sample taken from a cylinder heat treated

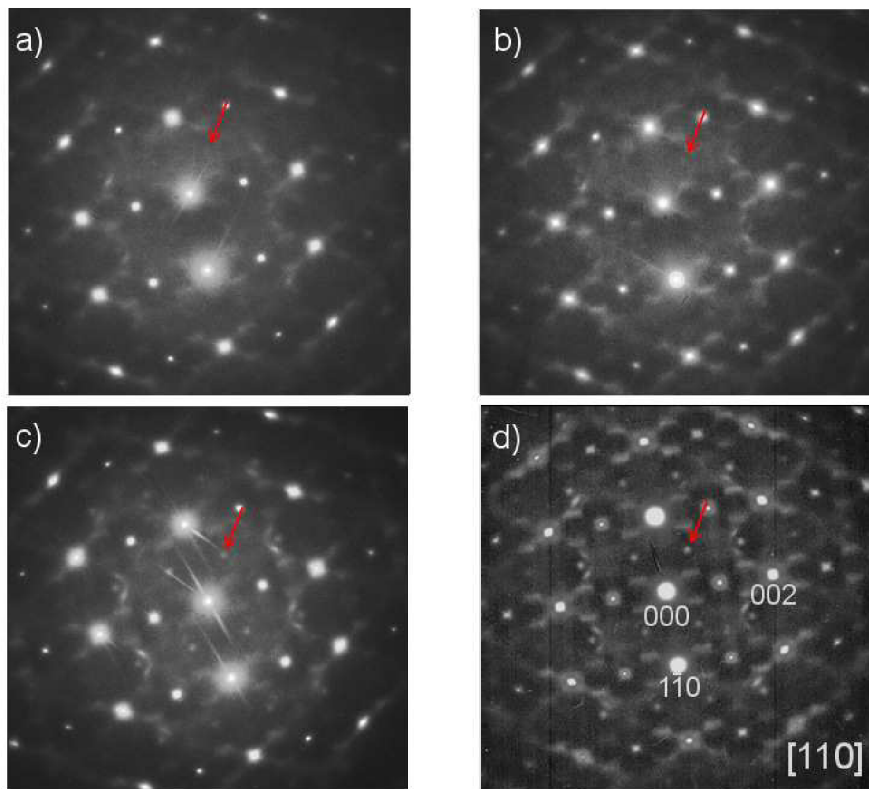


Fig. 3.19: SAD patterns of the quenched $\text{Ni}_{50.8}\text{Ti}_{49.2}$ alloy taken in the $[001]_{B2}$ zone. The patterns were obtained after the Regime I heat treatments in hydrogen-helium mixtures with hydrogen partial pressure: (a) 300, (b) 500, (c) 700 and (d) 900 mbar.

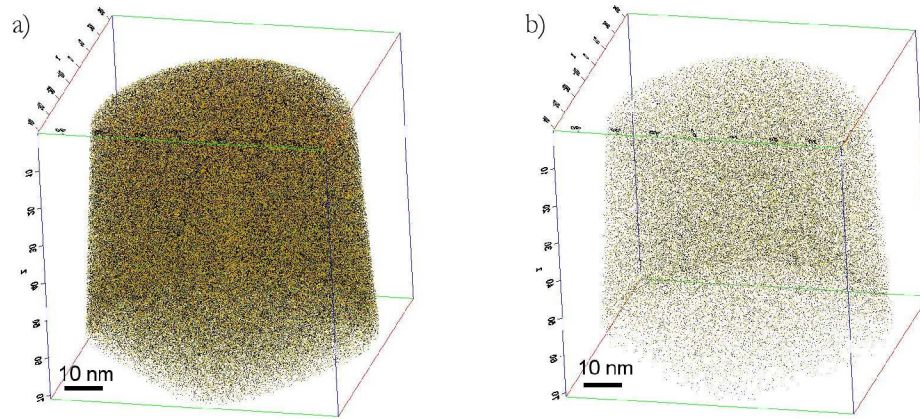


Fig. 3.20: 3D APT reconstructions of 10 (a) and 1 (b) % of detected atoms of a sample taken from cylinder heat treated in Regime I in hydrogen-helium mixture (H_2 partial pressure 700 mbar). Color codes correspond detected hydrogen, nickel and titanium atoms.

in hydrogen-helium mixture (H_2 partial pressure 700 mbar). Figures 3.20 a and b present APT reconstructions of only 10 (Fig. 3.20 a) and 1 % (Fig. 3.20 b) of detected atoms, respectively. Altogether, 11 millions of atoms were collected and analyzed in the APT experiment. Analyzed volume contained hydrogen, nickel and titanium atoms. Figure 3.21 provides information on the local concentration of hydrogen

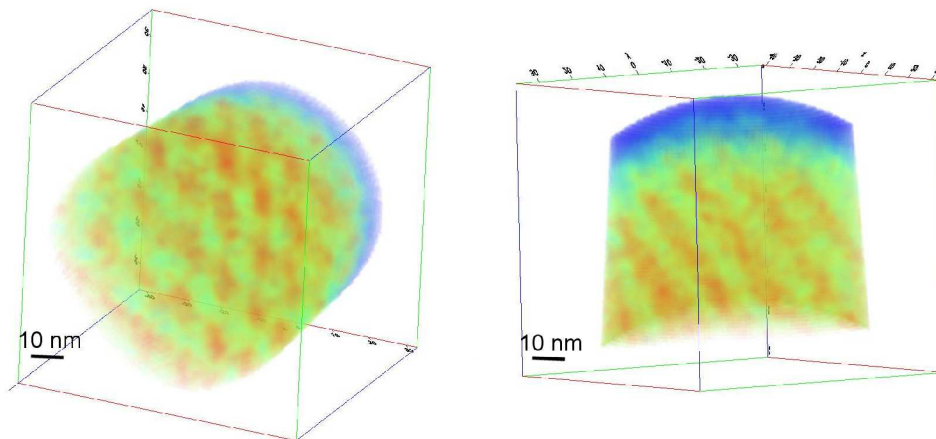


Fig. 3.21: 3D elemental map of hydrogen atoms in an AP sample after the Regime I heat treatment in hydrogen-helium mixture (H_2 partial pressure 700 mbar) showing isoconcentration surfaces which delimit regions with hydrogen content exceeding 10 at% (color coded red). The blue regions correspond to hydrogen concentration lower than 5 %at.

atoms. While spatial distribution of nickel and titanium atoms is homogeneous, hydrogen atoms cluster into nanometer-size domains organized into a regular (cubic) pattern. The hydrogen concentration in the domains is the highest (10 at%).

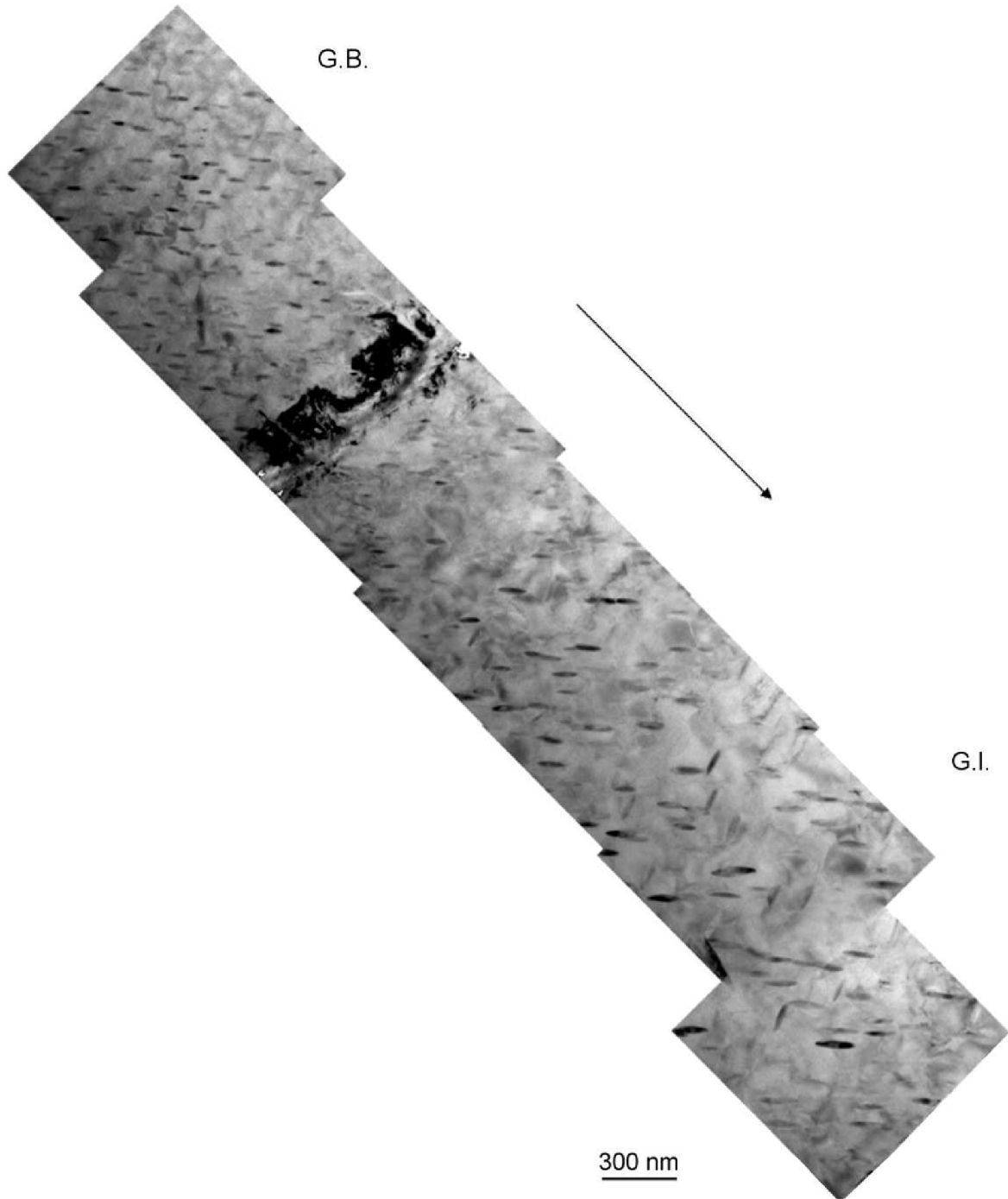


Fig. 3.22: Bright-field TEM images of the precipitation structure in a sample subjected to the Regime II heat treatment in air. The montage proceeds in the direction of the arrow from a grain boundary (G.B.) down to grain interior (G.I.).

3.2.4 Impact of heat treatments in Regime II on microstructure: varying size of Ni_4Ti_3 precipitates

Air

Figure 3.22 shows a montage of bright-field TEM images of Ni_4Ti_3 precipitates in sample subjected to the Regime II heat treatment in air. The montage proceeds from a grain boundary region (first TEM image on the left) down to the interior of the grain. TEM results confirm that the Regime II heat treatment in air result in a non-homogeneous distribution of Ni_4Ti_3 precipitate sizes [66, 68]. Particle diameters increase from 33 ± 4 nm at G.B. to 137 ± 6 nm in the G.I. The particle diameter near to G.B. is thus about six and half times smaller than in G.I. DSC measurements (three-step martensitic transformation on cooling) are in line with observed the inhomogeneous precipitation structure (see Section 1.7.4) [66, 68].

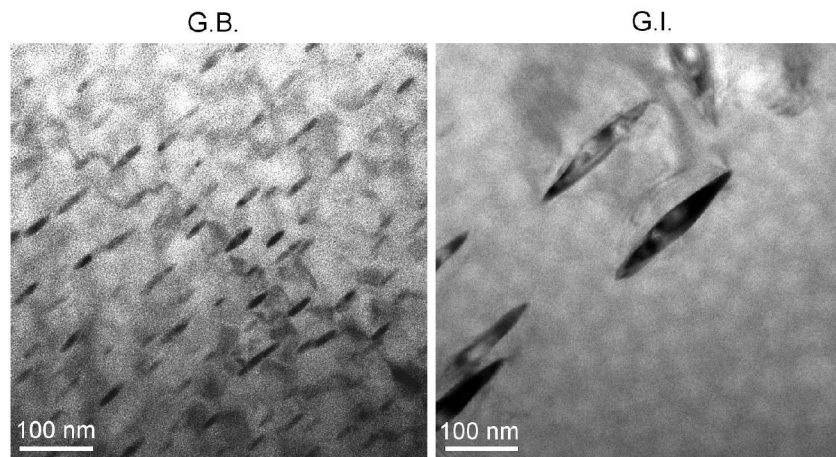


Fig. 3.23: Bright-field TEM images of G.B. and G.I. regions of the sample heat treated in the Regime II in air.

Hydrogen mixtures

The Ni_4Ti_3 precipitation structures are shown in Figure 3.24. The TEM micrographs were acquired from foils cut out of samples after the Regime II heat treatment in hydrogen-helium mixtures (H_2 partial pressures 20, 100, 300, 500 and 700 mbar) and in the reference helium atmosphere (He partial pressure 900 mbar). The Ni_4Ti_3 phase was identified based on the selected area diffraction data. These results suggest that no relevant differences exist between the samples heat treated in the atmospheres with increasing partial pressure of hydrogen. The quantitative assessment yielded mean Ni_4Ti_3 particle sizes of 33 ± 7 nm after the heat treatment in

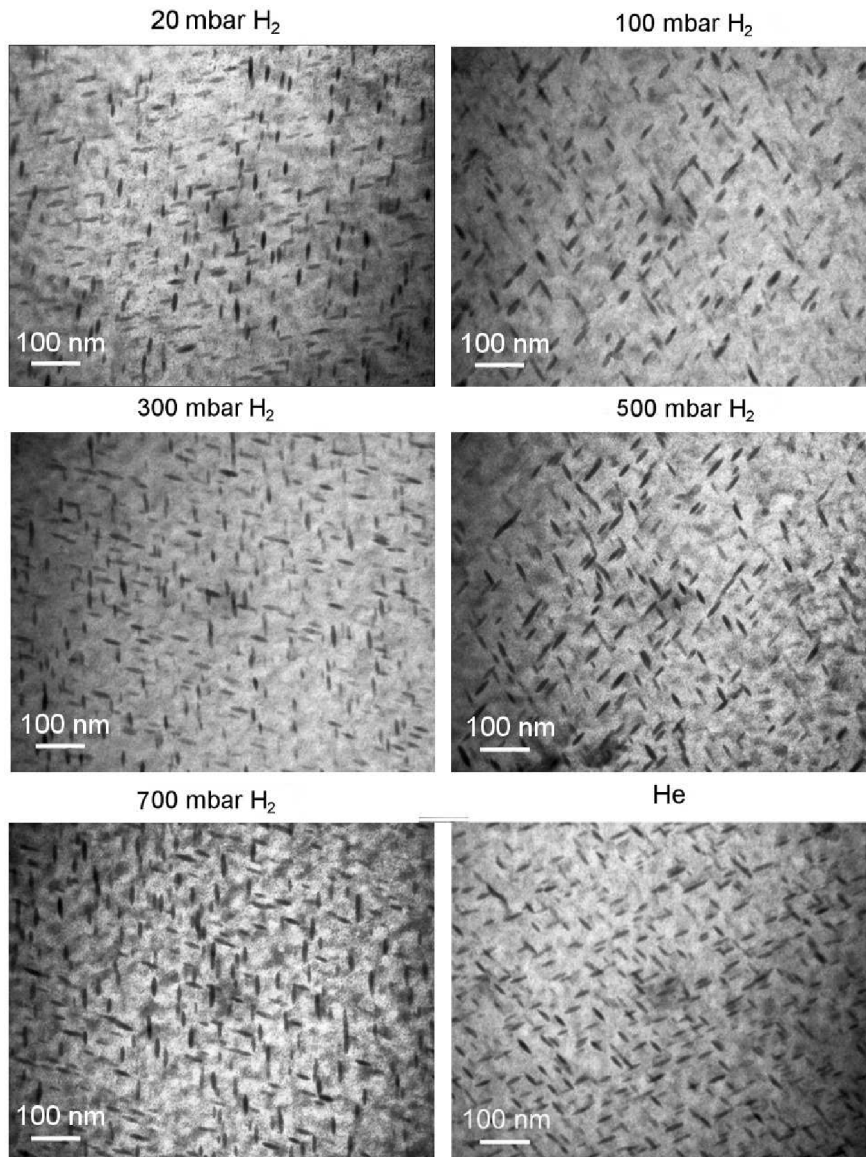


Fig. 3.24: Distribution and size of Ni_4Ti_3 variants as observed in TEM experiments after the Regime II heat treatment. Sample heat treated in hydrogen-helium mixtures (H_2 partial pressures 20, 100, 300, 500 and 700 mbar) and in the reference helium atmosphere (He partial pressure 900 mbar).

the 700/200 mbar hydrogen/helium mixture and 27 ± 7 nm for the material state after the heat treatment in pure helium. Since the precipitation of the Ni_4Ti_3 phase promotes the $\text{B2} \rightarrow \text{R}$ phase transition, the insensitivity of the $\text{B2} \rightarrow \text{R}$ transformation to the heat treatment environment observed in the DSC experiment (see Fig. 3.17) is in line with the stable particle parameters.

4 DISCUSSION

4.1 Alloys melted in Y_2O_3 crucible

4.1.1 Melt-crucible interaction mechanisms

VIM furnaces are generally equipped with refractory crucibles (see Section 1.6.3) [36]. Interaction occurring at melting temperatures between the liquid metal and the refractory crucible wall deteriorate a quality (purity) of the melt. The interactions may involve dissolution, diffusion, precipitation of reaction product, etc. The resulting increase in inclusion content generally leads to degradation of mechanical properties of the solidified alloys (like K_{IC}) [75, 76, 77].

At high temperatures, there is always a certain degree of dissolution of ceramic substrate when is in contact with a liquid metal, regardless of the reactivity of the later [78, 79]. The present study focuses on VIM of NiTi SMA's in Y_2O_3 crucibles. The interactions between NiTi liquid metal and the ceramic crucible then include the dissolution reaction of Y_2O_3 that results in a release of oxygen and yttrium into the molten alloy. The dissolution reaction of the Y_2O_3 crucible occurring at the solid/liquid interface can be described as:



where the parentheses mean that the elements are dissolved in the metal liquid. The equilibrium constant, $K_d(T)$ for this reaction 4.1 is given by:

$$K_d(T) = a_Y \cdot a_O^{\frac{3}{2}} = \exp\left(\frac{\Delta_f G^0_{(Y_2O_3)}}{RT}\right) \quad (4.2)$$

where a_Y is thermodynamic activity of yttrium in the alloy, a_O is the activity of dissolved oxygen and $\Delta_f G^0_{(Y_2O_3)}$ is standard Gibbs energy of formation per mole of Y_2O_3 . For lower concentration of oxygen and yttrium, the activity coefficients γ of these elements are nearly constant (Henry's law) and equal to the activity coefficients at infinite dilution in NiTi, γ_Y^∞ and γ_O^∞ :

$$a_Y = x_Y \cdot \gamma_Y^\infty \quad a_O = x_O \cdot \gamma_O^\infty \quad (4.3)$$

Eq. 4.2 can then be written as follows:

$$K_d(T) = x_Y \gamma_Y^\infty \cdot (x_O \gamma_O^\infty)^{\frac{3}{2}} \quad (4.4)$$

If the only source of elements Y and O is the Y_2O_3 crucible during melting, the molar fraction of Y and O are then related by $3 \cdot x_O = 2 \cdot x_Y$, it yields:

$$x_O^D = \left[\frac{3}{2} \gamma_Y^{-1} \gamma_O^{-\frac{3}{2}} \cdot \exp\left(\frac{\Delta_f G^0_{(Y_2O_3)}}{RT}\right) \right]^{\frac{2}{5}} \quad (4.5)$$

Oxygen can also be transported into the liquid metal from residual gases in the furnace chamber. The decomposition of residual gases occurring at liquid/gas interface can be described by:



The second contribution (Eq. 4.6) is likely small since the furnace chamber is evacuated and flushed several times with high purity argon before the melting process. Therefore, the most important source of the oxygen pick-up is associated with the decomposition of the yttria crucible through the first reaction (Eq. 4.1). Quantitative estimate of oxygen content in the NiTi cast should also consider the contribution of the melting stock:

$$x_{O(\text{in NiTi})} = x_{O(\text{from } Y_2O_3)} + x_{O(\text{in melt stock})} \quad (4.7)$$

The average oxygen content of the melting stock is 0.11 at%, see Section 3.1.1. Eq. 4.7 can be rearranged into:

$$x_{O(\text{in NiTi})} = x_{O(\text{from } Y_2O_3)} + 0.11 \quad (4.8)$$

The thermodynamic stability of the Y_2O_3 crucible thus governs chemical reaction described by Eq. 4.1. Furthermore, the open porosity and wetting resistance of the crucible can contribute to physical erosion. As a consequence, ceramic inclusions are introduced into the molten alloy. Inclusions presented in the molten NiTi alloy can thus be Y_2O_3 particles, dissolved yttrium and oxygen. Figures 3.4 c and d in Section 3.1.1 show the Y_2O_3 inclusion presented in the cast $Ni_{50.8}Ti_{49.2}$ alloy caused by erosion of the crucible wall.

The increase in oxygen content due to the interface reaction would be an issue as long as the reaction of Eq. 4.1 proceeds in the forward direction. Degree of progress of the dissolution reaction 4.1 at equilibrium can be calculated from Eq. 4.5. When the mole fraction of dissolved oxygen is higher than the solubility limit of oxygen in NiTi melt, precipitation of an oxide phase occurs. The experimental results revealed that the gradual increase in oxygen content (Fig. 3.6 b) from the Y_2O_3 crucible during melting was unavoidable and precipitation of Ti_2NiO_x phase was observed at the Y_2O_3 /NiTi liquid metal interface (Fig. 3.10).

Titanium as an element with high affinity to oxygen can promote the segregation of oxygen to the ceramic/metal interface. Assuming that the remaining interaction are negligible, Eq. 4.5 can be modified as:

$$x_O^D = \left[\frac{3}{2} \gamma_Y^{-1} \gamma_O^{-\frac{3}{2}} \cdot \exp\left(\frac{\Delta_f G^0(Y_2O_3)}{RT}\right) \right]^{\frac{2}{5}} \cdot \exp\left(-\frac{3}{5} \varepsilon_O^{Ti} \cdot x_{Ti}\right) \quad (4.9)$$

where ε_O^{Ti} is interaction parameter for NiTi melts.

Precipitation of the Ti_2NiO_x phase can be described as:



The equilibrium constant for this reaction, $K_p(T)$ will then be given by:

$$K_p(T) = x_{Ti} \gamma_{Ti}^{\infty} \cdot (x_O \gamma_O^{\infty})^x = \exp\left(\frac{\Delta_f G^0_{(Ti_2NiO_x)}}{RT}\right) \quad (4.11)$$

4.1.2 Oxygen contamination in a relation to melting temperatures

The oxygen contamination due to the interaction between a ceramic crucible and the molten NiTi alloy has important implications for the materials properties of the as-cast SMAs. When the melting stock is composed such that the required near equi-atomic NiTi composition is reached directly in one melting step (melting route A, see Chapter 2.2), the melting temperature increases considerably upon a release of exothermic heat of mixing. In the present work, the temperature increased from about 1450 to 1800 °C for the melting route A. Since the rate of most chemical reactions increases exponentially with increasing temperature (the Arrhenius equation), the excessive superheat can be a key factor for the enhanced oxygen pick-up. Besides, cooling of the super-heated molten alloy becomes more difficult and also the power input necessary for the melt stirring is difficult to stabilize.

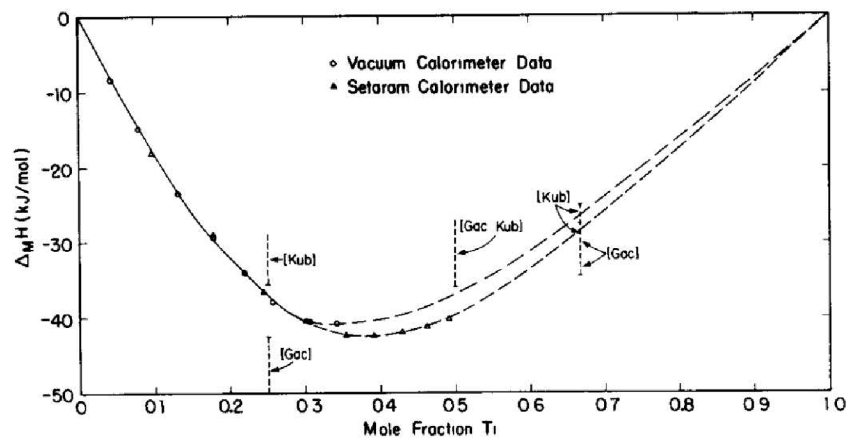


Fig. 4.1: Experimental enthalpies of Ni-Ti mixing from two sets of independent calorimetric measurements as a function of Ti mole fraction [80]. The plot also includes extrapolated values obtained for three solid intermetallic phases by Kubashewski [81] and from Gachon, Notin and Hertz [82].

Figure 4.1 displays the enthalpies of mixing for NiTi melts as a function of the mole fraction of titanium. The exothermic heat of mixing has a maximum -41.95 kJ/mol at about 40 at% Ti. In the melting route A, the enthalpy of mixing in the system with the composition 49.2 at% Ti and 50.8 at% Ni can be estimated as -40 kJ/mol. This value is close to the mentioned maximum. However, the enthalpies of mixing decrease with increasing mole fraction of Ti above 50 at% and with decreasing mole fraction Ti below 30 at%, see Figure 4.1. We take an advantage of this fact when performing melting experiments of route B and C. In the first step of the melting route B, the composition with a higher mole fraction Ti (64.8 at%) was targeted. This measure resulted in a lower exothermic heat of mixing released in the first melting step, and consequently the peak temperature attained in the experiment was considerably lower than in the route A. In spite of the fact that the overall change in enthalpy of mixing is a constant (the Hess's law), the decrease of the peak melting temperature is achieved, since melting at higher Ti molar fraction is also associated with generally lower temperatures of melting, see Figure 4.2. Therefore, the splitting the one melting step into two (routes B and C) helps in effectively suppressing the peak temperatures attained during melting. When the additional nickel was placed on the solidified upper layer in route B, the melting temperature in the second step increased from about 1060 to 1440 °C. Consequently, the melt could be easily cooled to 1400 °C. Melting temperatures associated with particular

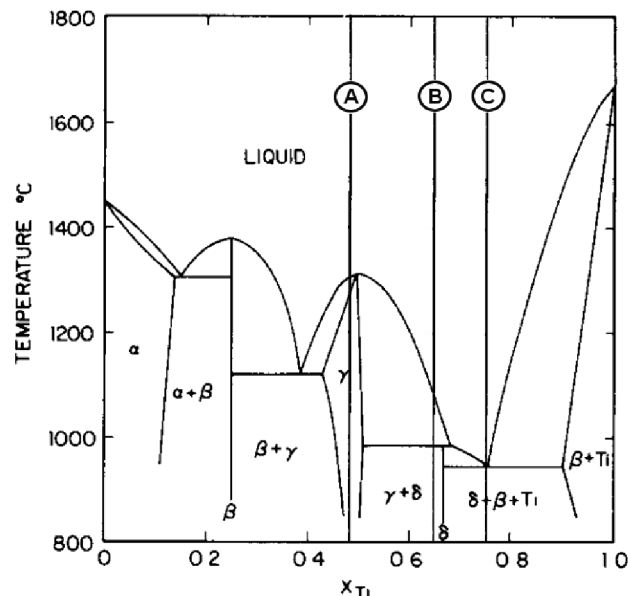


Fig. 4.2: The NiTi phase diagram (Poole and Hume-Rothery) [80]. The compositions of the melted stocks in first part of route A, B and C are marked.

steps of the melting routes A, B and C can be estimated from the binary NiTi phase diagram in Figure 4.2. In this study, alloys with eutectic composition 75.7 at% Ti (the melting routes C) were melted at about 942 °C and heated up by mixing of the additional Ni to only about 1400 °C.

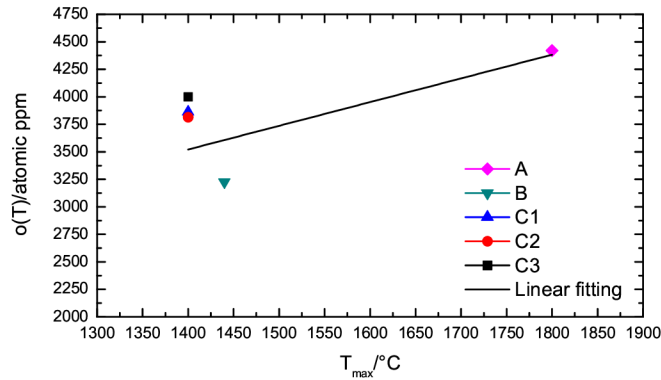


Fig. 4.3: The variation of oxygen content in the molten NiTi alloy during the VIM experiments A, B and C (C1–3) in Y_2O_3 crucible with the maximum measured temperature.

Figure 4.3 shows the variation of oxygen content in the solidified NiTi alloy as a function of the peak temperature attained in the complete melting cycle. The transformation ability of the least contaminated alloy B is demonstrated by DSC charts in Figure 4.4. The experimental melting routes were not successful and acceptable quality of the cast Ni-rich NiTi alloys has not been achieved during melting in Y_2O_3 crucible.

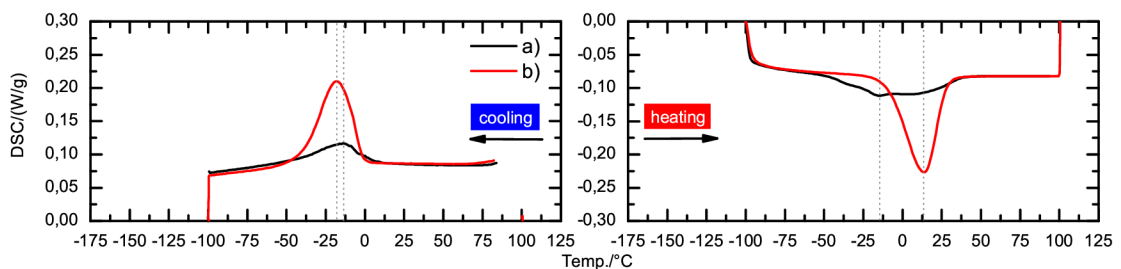


Fig. 4.4: (a) DSC chart of annealed samples of the $Ni_{50.8}Ti_{49.2}$ melted by route B. Sample were taken from position 3, see Figure 2.4. (b) DSC data of high quality vacuum induction melted $Ni_{50.9}Ti_{49.1}$ alloy in graphite crucible are included for comparison.

4.2 Heat treatments in controlled atmosphere

4.2.1 Material quality

As-received structure and transformation behavior

Annealing is an important processing step which leads to a reduction of local stresses and establishes chemical homogeneity of samples [83]. After annealing homogeneous stress-free NiTi samples are subjected to a standard quality test (based on the assessment of their transformation behavior) [84]. Residual local stresses or chemical inhomogeneities may considerably alter the phase transformation characteristics (see Sections 1.6.2 and 1.6.5). Annealing is thus an important part of the thermo-mechanical treatment of these alloys [85, 86]. Figure 4.5 shows the austenite B2 structure of the as-received commercial $\text{Ni}_{50.8}\text{Ti}_{49.2}$ alloy (see Section 2.1.2) contained dislocation cell substructure with a rather high density present in the cell boundaries.

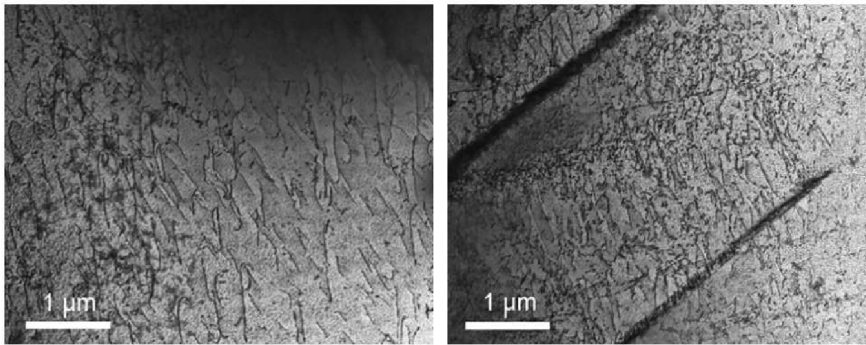


Fig. 4.5: Transmission electron micrographs of an as-received commercial $\text{Ni}_{50.8}\text{Ti}_{49.2}$ alloy. The dark contrasts shown in the micrographs are dislocations structures including tangled dislocation cell walls.

To remove these processing-related defects, the as-received material was subjected to an additional annealing at 850°C ($T_m/1.5$) for 1.8 ks and water quenched. Figure 4.6 shows the B2 structure after this additional annealing step. Figure 4.6 a displays relatively dislocation-free regions next to a high angle boundary. Well-ordered low angle boundaries with dislocation loop debris in annealed B2 structure are shown in Figure 4.6 b,c and d. Based on these TEM observations, it can be concluded that dislocations were arranged into new configurations and only partially annihilated during the additional annealing step.

The presence of lattice defects, e.g. the subgrains, in the annealed microstructure may cause widening of the transformation temperature range (as shown in Fig.

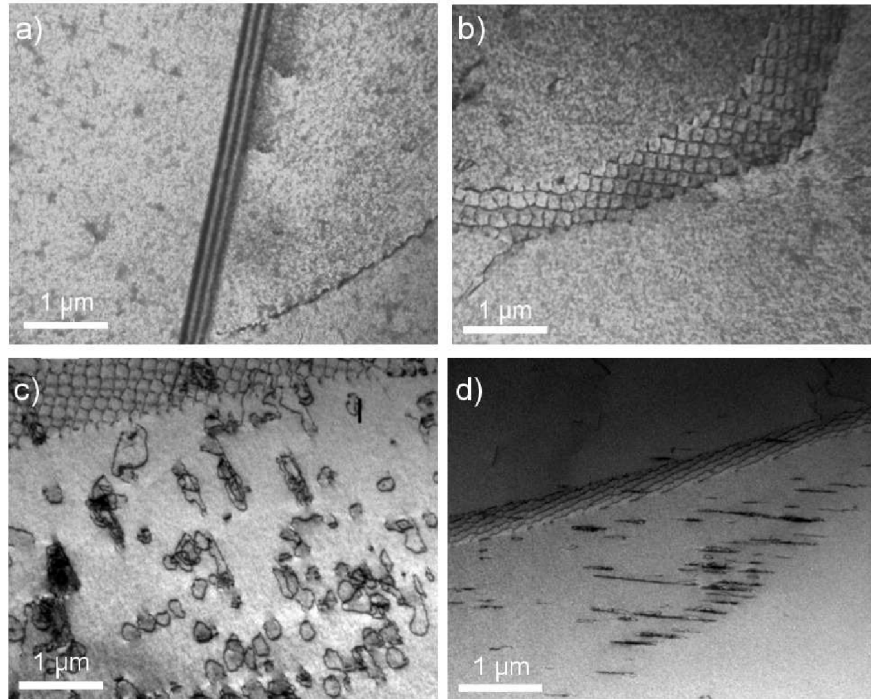


Fig. 4.6: Transmission electron micrographs of two samples (a,b and c,d) annealed in helium at 850 °C for 1.8 ks and water quenched. Dislocation-free regions next to a high angle boundary (a) and well-ordered low angle boundaries (b,c and d) with dislocation loop debris inside the subgrains (c) can be observed.

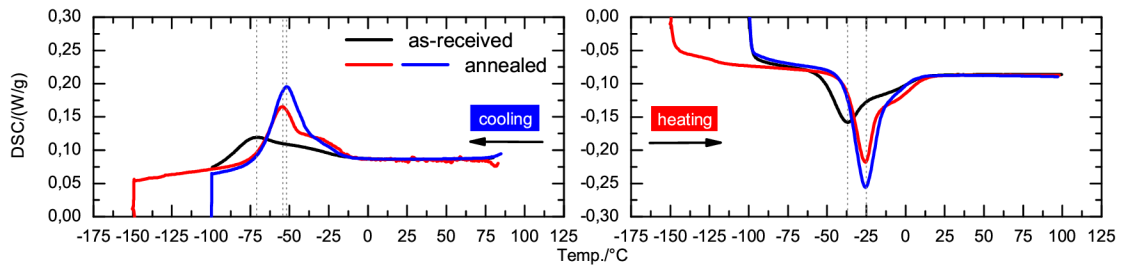


Fig. 4.7: DSC charts of (a) as-received sample and (b) samples annealed in helium at 850 °C for 1.8 ks and water quenched.

4.7). DSC charts of the as-received and two samples after additional annealing step are compared in Figure 4.7. The DSC analysis revealed that the presence of the inhomogeneous microstructure populated by dislocation defects along the received rod caused a premature transformation yielding the "knee" type data. Assuming that the premature transformation, e.g. B2→R, caused by the presence of dislocations can be represented by a specific DSC peak, DSC charts can be convoluted. This

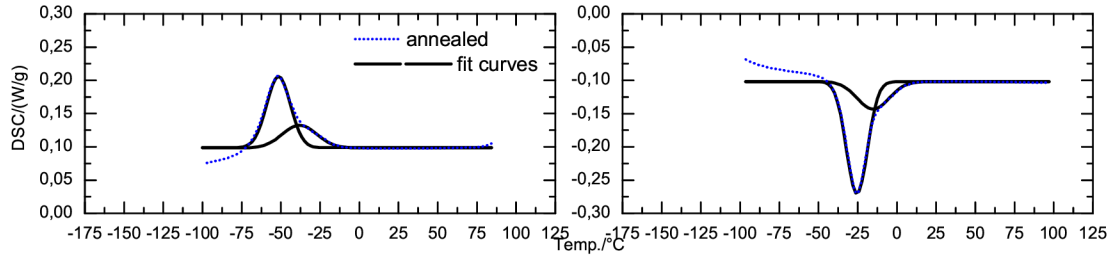


Fig. 4.8: DSC chart of annealed sample (blue curve in Fig 4.7) split into two fitted peak described by a Gaussian function.

procedure is illustrated in Figure 4.8 using Gaussian function profiles for the two separated peaks.

In situ TEM observations

In situ cooling TEM experiment was carried out account for martensitic transformation events associated with the presence of the subgrains in the B2 structure. A typical result of the in-situ cooling cycle is shown in Figure 4.9. The TEM bright-field image in Figure 4.9 documents a region in the microstructure, where a subgrain boundary extends from the left to the right upper part. On cooling to -52°C , the different variants of R-phase form on the subgrain boundary as it is indicated by the presence of weak extra spots at $1/3 \langle 110 \rangle$ B2 positions (see SAD pattern in the Fig. 4.9a) [87, 88]. The surrounding matrix is still untransformed, since no characteristic $1/3 \langle 110 \rangle$ reflection of R-phase are observed in the SAD pattern in Figure 4.9 b taken from interior of the subgrain. In other words the R-phase only appears on the subgrain boundaries. The identification of the R-phase was performed for the $[111]$ -matrix orientation (see Fig. 4.9). On further cooling to -75°C , a B19' needle appear. With decreasing temperature, the volume fraction of the B19' phase increases. The subgrain boundary is a special case of a coherent boundary [9] with lattice elastic distortion and it is well known that, similar to the stress field around fine Ni_4Ti_3 , these elastic distortions favor the formation R-phase (see Section 1.6.5) [51, 35].

It is worth noting that TEM samples are subjected to surface oxidation during preparation and handling at room temperature [89]. The high chemical affinity of Ti to oxygen results in selective oxidation and formation of Ti_2NiO_x and TiO_2 , leading to depletion of Ti from the matrix. Li et al. [89] studied size effect associated with the thermally induced martensitic transformation in nanoscale NiTi SMA. They pointed out that passive layer on the surface resists any mechanical lattice distortion associated with formation of martensite variants underneath. For the TEM samples, the thickness decreases towards the central hole in the TEM foil where the thickness

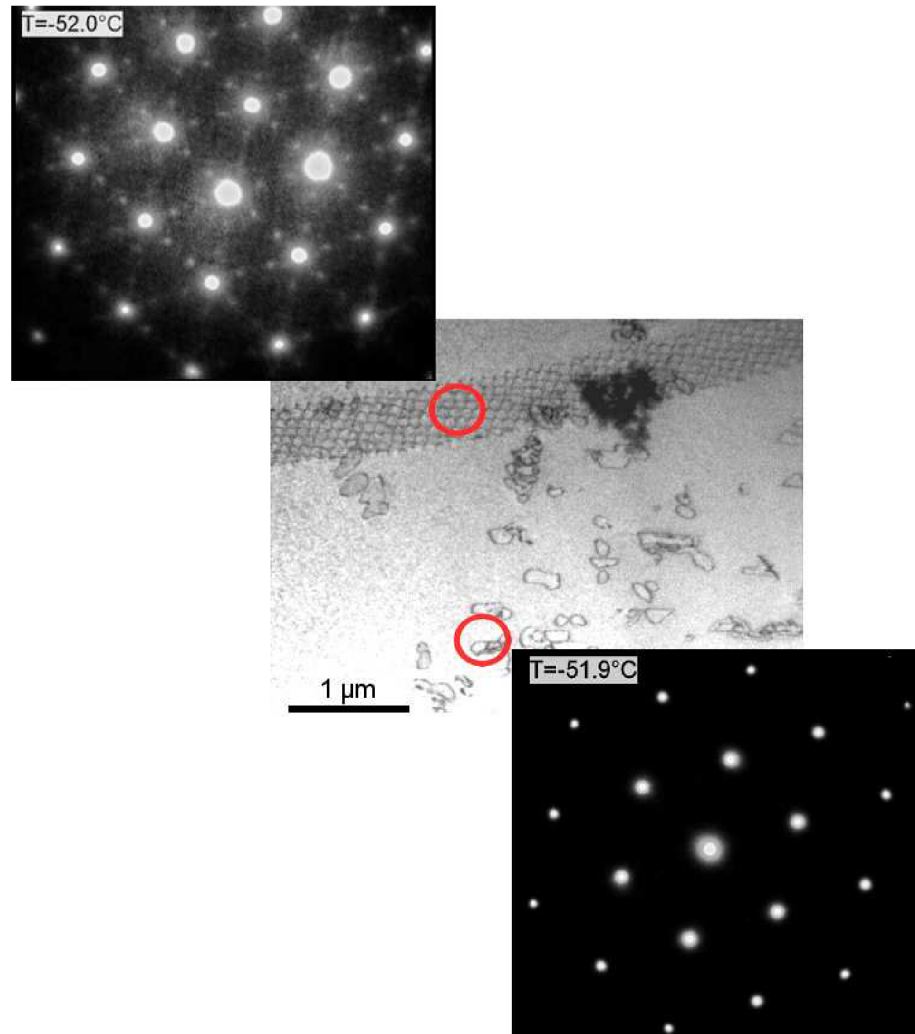


Fig. 4.9: Bright-field image of annealed sample in helium subjected to cooling. The R-phase can be detected on subgrain at -52°C (small extra spots at $1/3 \langle 110 \rangle$ in the selected are diffraction pattern a). The surrounding matrix was left untransformed, formed by B2 lattice in the pattern b.

is of the order of 10 nm and the influence of the passive oxide layers increases. This leads to a progressive reduction in the transformation temperature towards the edge. Other deviation from the DSC transformation temperatures can be caused by different cooling/heating rate, $2^{\circ}\text{C}/\text{min}$. With the lowest cooling rate, M_s shifts to the lower temperatures [90]. Therefore deviation of transformation temperatures obtained from in situ observation and DSC analysis have been expected. In situ observations were carried out relatively far from the perforated areas in order to limit as much as possible the passivity.

From the in situ cooling experiments and the above discussion it can be conclu-

ded that the DSC peaks on cooling are associated with the formation of R-phase on processing microstructural defects ("first peak") and the formation of B19' phase and its growth in the volume of parent B2 grains ("second peak").

4.2.2 Heat treatment in air

DSC results presented in Figure 3.13 suggest that Regime II heat treatment in air results in heterogeneous Ni_4Ti_3 precipitation structure in the commercial $\text{Ni}_{50.8}\text{Ti}_{49.2}$ alloy, see also Figure 3.22 in Section 3.2.4. The heterogeneity in the distribution and size of the Ni_4Ti_3 precipitates is observed between the grain boundary regions and the interior of grains. This heterogeneity may cause the MMT. DSC cooling chart in Figure 3.13 a shows three exothermic peaks related to the MMT. The relation between the precipitation heterogeneity and a sequence of the transformations was recently investigated in the study [68] (see Section 1.7.4).

In order to account for the effect of individual gases present in air on martensitic transformation in Ni-rich NiTi alloys, the Regime I heat treatment in nitrogen and oxygen was carried out. No suppression of the martensitic transformation was observed in samples heat treated in oxygen or nitrogen (see Fig. 3.14 and Table A.4 of the Appendix A.1).

Oxygen atoms may dissolve in the alloy after Regime I heat treatment because titanium atoms have a strong affinities to oxygen. The oxygen content may be too low to directly effect martensitic transformation but it may have an indirect impact. Later during the Regime II heat treatment, the inhomogeneous distributed oxygen atoms may serve as nucleation sites for Ni_4Ti_3 precipitates. Higher oxygen content near to G.B. causes the local lattice distortions which significantly effect the thermodynamics of nucleation of the Ni_4Ti_3 phase.

4.2.3 Hydrogen impact

DSC data obtained as a function of temperature for samples heat treated in gas mixture containing partial pressure of 0, 20, 100, 300, 500 and 700 mbar of hydrogen are shown in Figures 3.16 and 3.17. Figure 3.16 summarizes the DSC charts obtained for the samples after the Regime I heat treatment. On cooling, the exothermic peaks correspond to the forward transition. While the sample heat treated during annealing in pure helium transforms in one broad transformation step, the presence of hydrogen in the heat treatment environment results in a considerable suppression of the $\text{B2} \leftrightarrow \text{B19}'$ transformation. Corresponding transformation enthalpies associated with the transitions change accordingly. While the heat treatment in helium results in enthalpy of 15.25 J/g, the samples after treatments performed under hydrogen

partial pressures of 100, 700 and 900 mbar only release latent heat of 7.42, 6.02 and 4.95 J/g, respectively.

Figure 3.17 shows DSC charts obtained after the Regime II heat treatment (the Regime I and additional aging, see Section 2.3). Corresponding transformation enthalpies associated with the transitions change accordingly. The sample heat treated in pure helium yields two distinct peaks on cooling as well as on heating. This is a standard transformation sequence observed for aged Ni-rich NiTi alloys [91]. However, the transformation paths of samples heat treated under hydrogen partial pressures are different. The presence of hydrogen in the mixture leads again to a gradual suppression of the R→B19' transition during cooling. The B2-R transition recorded during cooling and heating was rather unaffected by the presence of hydrogen in the heat treatment environment. In order to check whether the hydrogen containing environment could affect the precipitation characteristics of the Ni₄Ti₃ phase during aging, the TEM and ND technique was used to document particle microstructures after Regime II heat treatments. The quantitative assessment yielded mean Ni₄Ti₃ particle sizes of 27±7 nm for the heat treatment in pure helium, 35±5 nm and 33±7 nm for the 100 and 700 mbar partial pressure of hydrogen. Neutron diffraction measurement were performed to analyze precipitation density in samples heat treated in Regime II in hydrogen-helium mixtures. The evaluation of ND data were effected by strong texture of samples and are not included in this study. These TEM results suggest that no relevant differences in size of Ni₄Ti₃ particle exist between structures formed during Regime II heat treatments in atmospheres with the increasing partial pressure of hydrogen. Since the precipitation of the Ni₄Ti₃ phase promotes the B2→R phase transition, the insensitivity of the B2→R transformation to the heat treatment environment observed in the DSC experiment (see Fig. 3.17) is in line with the stable particle parameters. As a consequence, the suppression of the B2→R transition cannot be directly attributed to an effect that hydrogen may have on the precipitation of the Ni₄Ti₃ phase (the Regime II) or to the similar effect that may exist regarding a formation of NiTiH precursor clusters after the Regime I heat treatment [91].

Recent systematic analysis performed by Tahara et al. [92] showed that similar extinction of the martensitic transformation in beta-Ti alloys doped by oxygen atoms can be associated with lattice modulations due to local strain fields of oxygen atoms. As suggested by Tahara et al. [92] and Wang et al. [93], the impurity atoms may lead to a formation of nano-domains that carry the same type of lattice distortion. It has been shown that the presence of the nano-domains in beta-Ti alloys gives rise to diffuse intensity maxima in the SAD patterns [93]. Type [110]_{B2} SAD patterns obtained in this work after Regime I heat treatments in hydrogen are shown in Figure 4.10. Diffuse spots at 1/2 (111)_{B2} positions, highlighted by arrows in Fig. 4.10,

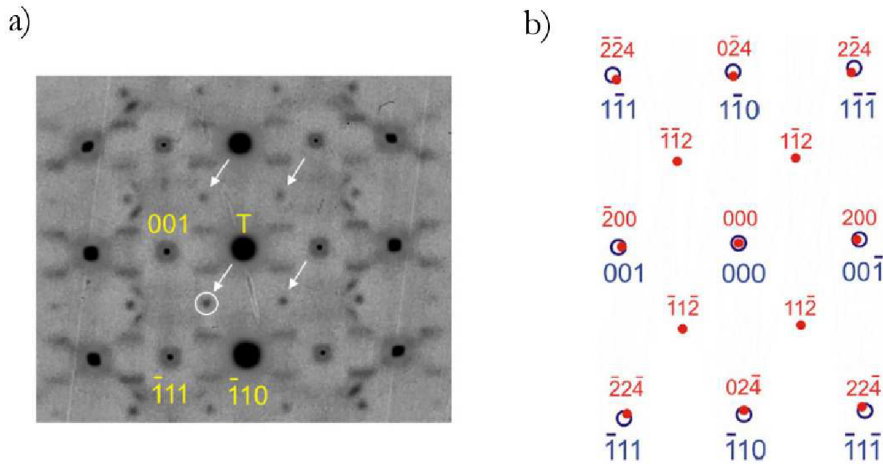


Fig. 4.10: (a) $[110]_{B2}$ -zone SADs obtained for the material states after Regime I heat treatments in hydrogen. Diffuse $1/2 (111)_{B2}$ intensity maxima are highlighted by arrows in the pattern. (b) Simulated SAD pattern assuming a B2 (blue open circles) and NiTiH (red dots) phase mixture, see text for details

are only present in the SAD pattern taken after the hydrogen-assisted heat treatment (see Fig. 3.17). The experimental $[110]_{B2}$ SAD pattern in Figure 4.10 a has been simulated assuming a phase mixture which consists of cubic B2 NiTi and tetragonal NiTiH hydride [94]. A JEMS simulation result presented in Fig. 4.10 b suggests that the diffuse maxima at $1/2 (111)_{B2}$ positions can be accounted for by the $\{112\}_{NiTiH}$ type reflections provided that the B2 cubic and the tetragonal NiTiH lattices obey an orientation relationship $[100]_{B2} \parallel [001]_{NiTiH}$ and $[010]_{B2} \parallel [010]_{NiTiH}$.

AP measurements proved the presence of hydrogen in samples heat treated in Regime I. More than 10 at% H remains locally dissolved in the NiTi alloy. Similar results were published in studies [95, 96] where desorption characteristics of hydrogen from NiTi B2 matrix were investigated. It has been shown that desorption of hydrogen from the cathodically charged samples starts at temperatures above 120°C and thus, at room temperature, hydrogen forms with NiTi a stable interstitial solid solution. Based on this study and results published earlier [95, 96], we suggest that the temperature stability of hydrogen enriched samples is the same regardless the method of charging. In the 3DTAP reconstruction the distribution of nickel and titanium atoms was investigated. The distribution of nickel and titanium atoms is homogeneous and no tendency to clustering of these atoms was found. The result supports the statement that the hydrogen suppressing effect on the MT does not depend on the content of nickel in nickel-rich NiTi alloys. Moreover a closer inspection

of the 3D AP results reveals that the distribution of hydrogen in the B2 lattice is not homogeneous. The hydrogen rich domains form a quasiperiodic structure with some features of cubic symmetry. However, in spite of the apparent hydrogen clustering, SAD patterns and corresponding diffraction TEM images did not provide any evidence that the hydrogen would cause a formation of hydride or other chemically and structurally distinct phases. Hydrogen atoms thus remain in solid solution and occupy tetrahedral or one type of the octahedral B2 lattice sites [97, 98, 99].

5 CONCLUSIONS

NiTi SMAs are considered the most successful shape memory materials today, which combine interesting functional properties with high mechanical strength and good corrosion resistance [53]. Since the transformation behavior has been recognized as a key issue of their successful applications, there is a strong demand for the understanding of all the aspects which the processing steps may have concerning the transformation and shape memory behavior. In addition, the materials must also have a good chemical homogeneity and a low content of impurities to fulfill further design requirements.

We have designed a series of melting experiments to investigate temperature effects and related oxygen contamination in Ni-rich NiTi ($\text{Ni}_{50.8}\text{Ti}_{49.2}$) SMA during VIM in u-shaped yttria crucible. We also carried out re-melting experiments to explore effect of the combination of variables; melting temperature and holding time, on the oxygen level with a strong focus on the optimization of the VIM processing route. The results of this study can be summarized as follows:

(1) Designed melting procedures lead to the lowering maximum temperature during VIM from 1800 °C to 1400 °C. Despite the significant maximum temperature drop oxygen content does not markedly reduce.

(2) During re-melting at 1500 °C with 2 min of holding time the oxygen content was increased by about two times with respect to its initial value. The increase from 454 to 1457 atomic ppm results in a complete suppression of martensitic transformation in the re-molten alloy. The release latent heat decreases exponentially with oxygen content.

(3) The experimental results revealed that a considerable reduction of melting temperature and holding time is absolutely necessary in order to successfully reduce of oxygen content in the conventional yttria crucible during melted ingots.

Heat treatment impurities impact and their impact on martensitic transformations in Ni-rich NiTi SMA have been investigated in the second part of the study. Results can be summarized as follows:

(1) Oxygen and nitrogen does not effect B2-B19' transformation in samples after heat treatment in the Regime I. In contrast heat treatment in the Regime I in hydrogen suppresses the overall transformation process and results in the extended DSC peaks. Hydrogen impact is also associated with a decrease of M_s , M_p and M_f temperatures. The values of A_s , A_p and A_f show no considerable dependence on the hydrogen content.

(2) The B2(R)→B19' suppression effect is also observed after heat treatment in the Regime II. The release and absorbed latent heat and transformation temperatures are significantly influenced by the hydrogen assisted heat treatments. This

behavior is identical for both the Regime I and II of heat treatments. The B2→R transition is rather unaffected by the presence of hydrogen in heat treatment environments.

(3) In situ TEM observations showed that the martensitic transformation proceeded by the same mechanism in spite whether the sample was previously heat treated in hydrogen or helium.

(4) The "knee" effect on DSC curves is associated with the formation of R-phase on microstructural defects inherited from processing steps.

(5) SAD analysis revealed pronounced modulation of background electron intensity in $[100]_{B2}$ and $[110]_{B2}$ SAD patterns in samples after the Regime I heat treatment in hydrogen.

(6) The 3DTAP measurement suggested that there are no local variations in the Ni and Ti compositions or positions of nickel and titanium atoms in the sample after the Regime I heat treatment in hydrogen. It was documented to hydrogen form stable interstitial solid solution in B2 NiTi where organizes into a nano-domains structure with the hydrogen content exceeding locally a level of 10 at%.

6 SUGGESTIONS FOR FUTURE WORK

The subjects of this work are of technological and scientific interest in many respects. Although extensive efforts have been made, the study is far from being complete and requires continuation.

Heat treatment environments dramatically effect on the martensitic transformations either directly or indirectly. But a precise mechanism has not been clarified yet and needs further investigation. TEM-EELS analysis is promising technique to study distribution of oxygen atoms in Ni-rich NiTi SMAs after heat treatments under controlled environments with systematic variations of the oxygen partial pressure. New 3DTAP data related to hydrogen distribution in a stoichiometric NiTi alloy subjected to heat treatments under controlled environments with systematic variations of the hydrogen partial pressure are needed.

BIBLIOGRAPHY

- [1] Otsuka, K., Wayman, C. M.: Shape Memory Materials. First edition, Cambridge University Press, 1998. ISBN 0 521 663849.
- [2] Funakubo, H.: Shape Memory Alloys, Gordon & Breach, New York, 1987.
- [3] Fremond, M., Miyazaki, S.: Shape Memory Alloys, International Center for Mechanical Sciences, No. 351. Springer-Verlag, Wein, 1996.
- [4] Miyazaki S. In: Duerig TW, Melton KN, Stockel D, Wayman CM, editors. Engineering applications of shape memory alloys. London: Butterworth-Heinemann; p. 394, 1990.
- [5] Morgan, N.B., Friend, C. M.: A review of shape memory stability in NiTi alloys. *J Phys IV*, France, Pr8-325–Pr8-332, 2001.
- [6] Duerig, T. W.: The use of superelasticity in modern medicine. *MRS Bull*, 27 (2), 101–104, 2002.
- [7] Sawaguchi, T., Kaustrater, G., Yawny, A., Wagner, M., Eggeler, G.: Shape-Memory Wires in Bending-Rotation Fatigue. *Metall Mater Trans*, 34A, 2847–2860, 2003.
- [8] Eggeler, G., Hornbogen, E., Yawny, A., Heckmann, A., Wagner, M.: Structural and functional fatigue of NiTi shape memory alloys. *Mater Sci Eng A*, 378:24–33, 2004.
- [9] Pfeiler, W.: Alloy Physics: A Comprehensive Reference. WILEY-VCH Verlag GmbH & Co. KGaA, Weinheim, Copyright 8, 2007. ISBN: 978-3-527-31321-1.
- [10] Ling, H. C., Kaplow, R.: Macroscopic length changes during the B2→R and M→B2 transitions in equiatomic Ni-Ti alloys. *Mater. Sci. Eng.*, 51, 193–201, 1981.
- [11] Huang, C. M., Meichle, M.E., Salamon, M. B., Wayman, C. M.: Transformation Behaviour of a $\text{Ti}_{50}\text{Ni}_{47}\text{Fe}_3$ Alloy: II. Subsequent premartensitic behaviour and the commensurate. *Phase Philosophical Magazine A*, 47, 31–62, 1983.
- [12] Salamon, M.B., Meichle, M. E., Wayman, C. M.: Premartensitic phases of $\text{Ti}_{50}\text{Ni}_{47}\text{Fe}_3$. *Phys Rev B Condens Matter*, 31, 7306, 1985.
- [13] Miyazaki, S., Wayman, C. M.: The R-phase transition and associated shape memory mechanism in Ti?Ni single-crystals. *Acta Metall. Mater.*, 36, 181–192, 1988.

- [14] Wang, X.: Crystallization and Martensitic Transformation Behavior of NiTi Shape Memory Alloy Thin Films. Dissertation, Harvard University Cambridge, Massachusetts, May 2007.
- [15] Kroger, A., et al.: Direct transmission electron microscopy observations of martensitic transformations in Ni-rich NiTi single crystals during in situ cooling and straining. *Materials Science and Engineering A*, 481–482, 452–456, 2008.
- [16] Khalil Allafi, J., Ren, X., Eggeler, G.: The mechanism of multistage martensitic transformations in aged Ni-rich NiTi shape memory alloys, *Acta Mat.* 50, pp 793-803, 2002.
- [17] Cahn, R. W., Haasen, P.: Physical Metallurg. Fourth, revised and enhanced edition, Volume II, Elsevier Science B.V., 1996. ISBN 0 444 89875 1.
- [18] Haldar, A., Suwas, S., Bhattacharjee, D.: Microstructure and texture in steels, Springer, 2009. ISBN: 978-1-84882-453-9.
- [19] Porter, D. A., Easterling, K. E.: Phase transformations in metals and alloys. Second edition, Chapman & Hall, 1992. ISBN 0 412 45030 5.
- [20] Plietsch, P., Ehrlich, K.: Strength differential effect in pseudoelastic NiTi shape memory alloy. *Acta Metallurgica*, Vol. 45 (6), 2417–2424, 1997.
- [21] Wang, X. M., et al.: Micromechanical modelling of the effect of plastic deformation on the mechanical behaviour in pseudoelastic shape memory alloys. *International Journal of Plasticity*, 24, 1307–1332, 2008.
- [22] Zhou, N., et al.: Effect of Ni₄Ti₃ precipitation on martensitic transformation in Ti-Ni. *Acta Materialia*, 58, 6685–6694, 2010.
- [23] Kudoh, Y., Tokonami, M., Miyazaki, S., Otsuka, K.: Crystal structure of the martensite in Ti-49.2 at% alloy analyzed by the single crystal X-ray diffraction method. *Acta Metallurgica*, 33(11), 2049-2056, 1985.
- [24] Khalil-Allafi, J., Schmahl, W. W., Toebbens, D. M.: Space group and crystal structure of the R-phase in binary NiTi shape memory alloys. *Acta Materialia*, 54(12), 3171–3175, 2006.
- [25] Khalil-Allafi, J., et al.: Quantitative phase analysis in microstructures which display multiple step martensitic transformations in Ni-rich NiTi shape memory alloys. *Materials Science and Engineering A*, 438–440, 593–596, 2006.

-
- [26] Goo, E., Sinclair, R.: The B2 to R transformations in $\text{Ti}_{50}\text{Ni}_{47}\text{Fe}_3$ and $\text{Ti}_{49.5}\text{Ni}_{50.5}$ alloys. *Acta Metallurgica*, 33(9), 1717–1723, 1985.
- [27] Beyer, J.: Recent advances in the martensitic transformations of Ti-Ni alloys. *Journal de physique IV*, Colloque C2-433. Volume 5, 1995.
- [28] Kudoh, Y., Tokonami, M., Miyazaki, S., Otsuka, K.: Crystal structure of the martensite in Ti-49.2 at%Ni alloy analyzed by the single crystal X-ray diffraction method. *Acta Metallurgica*, 33(11),2049–2056, 1985.
- [29] Atkins, P. W.: Physical chemistry. Fifth Edition, Oxford university press, 1994.
- [30] Povoden-Karadenizetal, E., et al.: Thermodynamics of Ti-Ni shape memory alloys. *CALPHAD: Computer Coupling of Phase Diagrams and Thermochemistry*, 41, 128–139, 2013.
- [31] Liu, Y., Favier, D.: Stabilization of martensite due to shear deformation via variant reorientation in polycrystalline NiTi. *Acta Mater*, 48, 3489–3499, 2000.
- [32] Khalil Allafi, J., Eggeler, G., Dlouhy, A., Schmahl, W.W., Somsen, C.: On the influence of heterogeneous precipitation on martensitic transformations in a Ni-rich NiTi shape memory alloy. *Mater Sci Eng A*, 378, 148–51, 2004.
- [33] Kim, J. I., Liu, Y., Miyazaki, S.: Ageing-induced two-stage R-phase transformation in Ti-50.9 at% Ni. *Acta Mater*, 52, 487–99, 2004.
- [34] Mentz, J., et al.: Powder metallurgical processing of NiTi shape memory alloys with elevated transformation temperatures. *Materials Science and Engineering A*, 491, 270–278, 2008.
- [35] Khalil Allafi, J., Eggeler, G., Dlouhy, A.: Ni_4Ti_3 -precipitation during aging of NiTi shape memory alloys and its influence on martensitic phase transformations. *ActaMaterialia*, 50, 4255–4274, 2002.
- [36] Yoneyama, T., Miyazaki, S.: Shape memory alloys for biomedical applications, Woodhead Publishing Ltd, p. 352, 2008. SBN 978-1-84569-344-2.
- [37] Nurveren, K., Akdogan, A., Huang, W. M.: Evolution of transformation characteristics with heating/cooling rate in NiTi shape memory alloys, *Journal of Materials Processing Technology*, Issue 1, Vol. 193, pp 129-134, 2008.
- [38] Lagoudas, D.C.: Shape Memory Alloys, DOI: 10.1007/978-0-387-47685-8 6, © Springer Science and Business Media, LLC, 2008.

- [39] Elahinia, M. H., et al.: Manufacturing and processing of NiTi implants: A review. *Progress in Materials Science*, 57, 911–946, 2012.
- [40] Wu, M.H.: Fabrication of Nitinol Materials and Components. *Proceeding of the Internation Conference on Shape Memory and Superelastic Technology*, China, 285–292, 2001.
- [41] Saburi T. In: Otsuka K, Wayman CM, editors. Shape memory materials. Cambridge: Cambridge University Press; p. 49, 1998.
- [42] Saburi, T., Nenno, S., Fukuda, T.: Crystal structure and morphology of the metastable X-phases in shape memory Ti–Ni alloy. *Journal of Less Common Metals*, 125, 157–166, 1986.
- [43] Dlouhy A, Khalil-Allafi J, Eggeler G.: On the determination of the volume fraction of Ti_3Ni_4 precipitates in binary Ni-rich NiTi shape memory alloys. *Z Metallkd*, 95, 518–524, 2004.
- [44] Michutta, J., et al.: Elementary martensitic transformation processes in Ni-rich NiTi single crystals with Ni_4Ti_3 precipitates. *Acta Materialia*, 54, 3525–3542, 2006.
- [45] Tadaki T, Nakata Y, Shimizu K, Otsuka K.: Crystal structure, composition and morphology of a precipitate in an aged Ti-51 at% Ni shape memory alloy. *Trans JIM*, 27, 731–740, 1986.
- [46] Treppmann D, Hornbogen E, Wurzel D.: The effect of combined recrystallization and precipitation process on the functional and structural properties in NiTi Alloy. *J Phys IV*, C8, 569–574, 1995.
- [47] Frick, C. P., Ortega, A. M., Tyber, J., Gall, K., Maier, H. J.: Multiscale structure and properties of cast and deformation processed polycrystalline NiTi shape memory alloy. *Metall Mater Trans A*, 35, 2013–2025, 2004.
- [48] Tirry, W., Schryvers, D.: Quantitative determination of strain fields around Ni_4Ti_3 precipitates in NiTi. *Acta Mater*, 53, 1041–1049, 2005.
- [49] Shakeri, M. S., et al.: The influence of Ni_4Ti_3 precipitates orientation on two-way shape memory effect in a Ni-rich NiTi alloy. *Journal of Alloys and Compounds*, 485, 320–323, 2009.
- [50] Frenzel, J., et al.: Influence of Ni on martensitic phase transformations in NiTi shape memory alloys. *Acta Materialia*, 58, 3444–3458, 2010.

-
- [51] Carroll, M. C., Somsen, Ch., Eggeler, G.: Multiple-step martensitic transformations in Ni-rich NiTi shape memory alloys. *Scripta Materialia*, 50, 187–192, 2004.
- [52] Gollerthan, S., Young, M.L., Baruj, A., Frenzel, J., Schmahl, W.W., and Eggeler, G.: Fracture mechanics and microstructure in NiTi shape memory alloys. *Acta Materialia*, 57, 1015–1025, 2009.
- [53] Frenzel, J., et al.: High quality vacuum induction melting of small quantities of NiTi shape memory alloys in graphite crucibles. *Journal of Alloys and Compounds*, 385, 214–223, 2004.
- [54] Zhang, Z., et al.: Orientation relationship between TiC carbides and B2 phase in as-cast and heat-treated NiTi shape memory alloys. *Materials Science and Engineering A*, 438–440, 879–882, 2006.
- [55] Chen, F., et al.: Effect of graphite addition on martensitic transformation and damping behavior of NiTi shape memory alloy. *Materials Letters*, 65, 1073–1075, 2011.
- [56] Du, Y., Schuster, J.C.: Experimental investigation and thermodynamic modeling in the Ni-Ti-C system, *Z Metallkd* 89, 6, 399–410, 1998.
- [57] Zhang, Z., Frenzel, J., Neuking, K., and Eggeler, G.: On the reaction between NiTi melts and crucible graphite during vacuum induction melting of NiTi shape memory alloys. *Acta Materialia*, 53, 3971–3985, 2005. Influence of Ni on martensitic phase transformations in NiTi shape memory alloys
- [58] Chuprina, V. G., Shalya, I. M.: Reactions of TiNi with oxygen. *Powder Metallurgy and Metal Ceramics*, 41, 1–2, 2002.
- [59] Kuběnová, M.: Hodnocení homogeneity ingotů slitin Ni-Ti metodou DSC. Diploma thesis, 2009.
- [60] Mueller, M.H., Knott, H.W.: The crystal structures of Ti_2Cu , Ti_2Ni , Ti_4Ni_2O , and Ti_4Cu_2O . *Transactions of the Metallurgical Society of Aime*, 227, 674–678, 1963. ICSD 15809.
- [61] Fruchart, D., Soubeyroux, J. L., Miraglia, S., Obbade, S.: *Zeitschrift fur Physikalische Chemie*, 179, 225–236, 1993.
- [62] Soubeyroux, J. L., Fruchart, D., Lorthioir, G., Ochin, P., Colin, D.: *Journal of Alloys and Compounds*, 196, 127–132, 1993.

- [63] Pelton, B.L., Slater, Pelton, A.: Effect of hydrogen NiTi, Proceedings of 2nd Int. Conference on Shape Memory and Superelastic Technologies SMST, 1997, pp 395-400.
- [64] Tang, W.: Thermodynamic study of the low-temperature phase B19' and the martensitic transformation in near-equiatomic Ti-Ni shape memory alloys, Metall Mater Trans A, Vol 28, p. 537, 1997.
- [65] Runciman, A., Chen, K.C., Pelton, A.R., Trepanier, Ch.: Effect of hydrogen on the phases and transition temperatures of NiTi, Proceedings of the International Conference on Shape Memory and Superelastic Technologies. California, May 7-11, p 185-196, 2006.
- [66] Nishida, M., et al.: Experimental Consideration of Multistage Martensitic Transformation and Precipitation Behavior in Aged Ni-Rich Ti-Ni Shape Memory Alloys. *Materials Transactions*, 44 (12), 2631–2636, 2003.
- [67] Fujishima, K., et al.: Effect of heat treatment atmosphere on the multistage martensitic transformation in aged Ni-rich Ti-Ni alloys. *Materials Science and Engineering A*, 438–440, 489–494, 2006.
- [68] Karbakhsh Ravari, B., et al.: Quantitative microstructure analyses upon multistage martensitic transformation in an aged Ti-50.8 at% Ni alloy. *Journal of Alloys and Compounds*, xxx, xxx–xxx, 2012. Article in press.
- [69] Cao, S., et al.: Quantitative three-dimensional analysis of Ni₄Ti₃ precipitate morphology and distribution in polycrystalline Ni-Ti. *Acta Materialia*, 59, 1780–1789, 2011.
- [70] Rachbauer, R., et al.: Atom probe specimen preparation and 3D interfacial study of Ti-Al-N thin films. *Surface & Coatings Technology* 204, 1811–1816, 2010.
- [71] Felfer, P.J., et al.: A Reproducible method for damage-free site-specific preparation of atom probe tips from interfaces. *Microscopy research and technique*, 00, 000–000, 2011.
- [72] Zalešák, J.: Vliv tepelného zpracování na transformační vlastnosti slitin NiTi. Diploma thesis, 2012.
- [73] Kabiri, Y., Kermanpur, A., Foroozmehr, A.: Comparative study on microstructure and homogeneity of NiTi shape memory alloy produced by copper boat induction melting and conventional vacuum arc melting. *Vacuum* 86, 1073–1077, 2012.

-
- [74] Coda, S., Zilio, S., Norwich, D., Sczernie, F.: Characterization of inclusions in VIM/VAR NiTi alloys. *Materials and Engineering and Performance* 21, 2572–2577, December 2012.
- [75] Kuang, J.P., Harding, R.A., Campbell, J.: Investigation into refractories as crucible and mould materials for melting and casting γ -TiAl alloys. *Materials Science and Technology* 16, 1007–1016, 2000.
- [76] Kawabata, T., Tadano, M., Izumi, O.: Effect of Purity and Second Phase on Ductility of TiAl. *Scripta Metall.* 22, 1725–1730, 1998.
- [77] Dlouhy, A., Zemcik, L.: Investment Casting Technology Tailored to Near-Gamma TiAl Alloys. Proceedings of the first invited COST 526 Conference on Automatic Process Optimization in Material Technology. Switzerland, 30–31 May, 146–154, 2005.
- [78] Eustathopoulos, N., Drevet, B.: Interaction at non-reactive metal/ionocovalent oxide interfaces: physical or chemical? Proceeding of the Conference on High Temperature Capillarity. Poland, 29 June–2 July, 35–45, 1997.
- [79] Arróyave, R.: Thermodynamics and Kinetics of Ceramic/Metal Interfacial Interactions. Doctor thesis, Massachusetts Institute of Technology, 2004.
- [80] Luck, R., Arpshofen, I.: Calorimetric determination of the enthalpies of formation of liquids Ni-Ti alloys. *Thermochimica Acta*, 131, 171–181, 1988.
- [81] Kubaschewski, O.: The heats of formation in the system aluminium + nickel + titanium. *Transactions of the Faraday Society*, 54, 814–820, 1958.
- [82] Gachon, J.C., Notin, M., Hertz, J.: The enthalpy of mixing of the intermediate phases in the systems FeTi, CoTi, and NiTi by direct reaction calorimetry. *Thermochimica Acta*, 48, 155–164, 1981.
- [83] Totten, G., Howes, M., Inoue, T.: Handbook of Residual Stress and Deformation of Steel. March 2012. ISBN 0-87170-729-2.
- [84] ASTM F 2004–05: Standard test method for transformation temperature of nickel-titanium alloys by thermal analysis. Published in November 2005.
- [85] Davis, J., et al.: ASM Handbook, V2 Properties and Selection Nonferrous Alloys and Special Purpose Materials. ASM International, 897–902, 1990.
- [86] Xu, C.H., Ma, X.Q., Shi, S.Q., Woo, C.H.: Oxidation behavior of TiNi shape memory alloy at 450–750 °C. *Materil Sci and Eng A* 371, 45–50, 2004.

- [87] Stroz, D.: TEM studies of the R-phase transformation in NiTi shape memory alloy after thermo-mechanical treatment. *Material Chemistry and Physics* 81, 460–462, 2003.
- [88] Kroger, A., Dzaszyk, S., Frenzel, J., Somsen, Ch., Dlouhy, A., Eggeler, G.: Direct transmission electron microscopy observations of martensitic transformations in Ni-rich NiTi single crystals during in situ cooling and straining. *Material Sci and Eng A* 481–482, 452–456, 2008.
- [89] Li, H.X., Mao, S.C., Zang, K.T., Liu, Y., Guo, Z.X., Wang, S.B., Y.F., Zhang, Yin, X.Q.: An in situ TEM study of the size effect on the thermally induced martensitic transformation in nanoscale NiTi shape memory alloy. *Journal of Alloys and Compounds*, accepted Manuscript, 2013.
- [90] Nurveren, K., Akdogan, A., Huang, W.M.: Evolution of transformation characteristics with heating/cooling rate in NiTi shape memory alloys. *Journal of materials processing technology*, 196, 129–134, 2008.
- [91] Somsen, Ch., Ph.D. Thesis, Shaker Verlag, Aachen, 2002.
- [92] Tahara, M., Kim, H.Y., Inamura, T., Hosoda, H., Miyazaki, S.: *Acta Materialia* 59, 6208–6218, 2011.
- [93] Wang, D., Zhang, Z., Zhang, J., Zhou, Y., Wang, Y., Ding, X., Wang, Y., Ren, X.: *Acta Materialia* 58, 6206–6215, 2010.
- [94] Soubeyroux, J.L., Fruchart, D., Lorthioir, G., Ochin, P., Colin, D.: *Journal of Alloys and Compounds* 196, 127–132, 1993.
- [95] Tomita, M., Yokoyama, K., Asaoka, K., Sakai, J.: Hydrogen thermal desorption behavior of NiTi superelastic alloy subjected to tensile deformation after hydrogen charging. *Materials Science and Engineering A* 476, 308–315, 2008,.
- [96] Yokoyama, K., Tomita, M., Sakai, J.: Hydrogen embrittlement behavior induced by dynamic martensite transformation of Ni-Ti superelastic alloy. *Acta Materialia* 57, 1875–1885, 2009.
- [97] Numakura, H., Okamoto, N., Moriya, K., Koiwa, M.: Mechanical relaxation due to hydrogen? solute complexes in dilute Ni-Ti-H alloys. *Acta Metall. at Mater.* 43, 2807–2814, 1995.
- [98] Soubeyroux, J.L., Fruchart, D., Lorthioir, G., Ochin, P., Colin, D.: Structural study of the hydrides NiTiH_x (x = 1.0 and 1.4). *Journal of Alloys and Compounds* 196, 127–132, 1993.

- [99] Biscarini, A., Campanella, R., Coluzzi, B., Mazzolai, G., Trotta, L., Tuissi, A., Mazzolai, F.M.: Martensitic transitions and mechanical spectroscopy of $\text{Ni}_{50.8}\text{Ti}_{49.2}$ alloy containing hydrogen. *Acta Materialia* 47, 4525–4533, 1999.

LIST OF SYMBOLS, PHYSICAL CONSTANTS AND ABBREVIATIONS

SME Shape memory effect

PE Pseudo-elasticity

1WE One way effect

PTTs Phase transformation temperatures

$\Delta G_{T,p}$ Change in Gibbs free energy at constant pressure and temperature

G_i Gibbs free energy of initial state

G_f Gibbs free energy of final state

$\Delta H_{S,p}$ Change in enthalpy at constant entropy and pressure

$\Delta S_{H,p}$ Change in entropy at constant enthalpy and pressure

T_0 Equilibrium temperature

VIM Vacuum induction melting

VAR Vacuum arc remelting

SMA Shape memory alloys

M_s The martensite start temperature

M_f The martensite finish temperature

R_s The R-phase start temperature

R_f The R-phase finish temperature

A_s The austenite start temperature

R_f The austenite finish temperature

A Austenite

M^t Twinned martensite

M^d Detwinned martensite

ASTM American Society for Testing and Materials

- XRD X-ray diffraction
- TEM Transmission electron microscopy
- G.B. Grain boundaries
- G.I. Grain interior
- DSC Differential scanning calorimetry
- SEM Scanning electron microscopy
- EDS Energy-dispersive X-ray spectroscopy
- EBSD Electron backscatter diffraction
- TEM Transmission electron microscopy
- GIS Gas injection system
- ND Neutron diffraction
- AP Atom probe
- SAD Selected area diffraction
- APT Atom probe topography
- MMT Multistage martensitic transformation
- MEREDIT Medium resolution neutron powder diffractometer
- LEAP Local electrode atom probe
- FEG Field emission gun
- $K_d(T)$ Equilibrium constant for oxide dissolution reaction
- a_Y Chemical activity of yttrium
- a_O Chemical activity of oxygen
- γ_Y Chemical activity coefficient for yttrium
- γ_Y^∞ Chemical activity coefficient for yttrium at infinite dilution
- γ_O Chemical activity coefficient for oxygen
- γ_O^∞ Chemical activity coefficient for oxygen at infinite dilution

$\Delta_f G_{(Y_2O_3)}^0$ Standard Gibbs energy of formation for Y_2O_3

R Universal gas constant, $R = 8.314 \frac{J}{molK}$

T Temperature, K

ε_O^{Ti} Wagner first order interaction coefficient between Ti and O dissolved in solvent.

x_O Molar fraction of oxygen.

x_y Molar fraction of yttrium.

x_O^D Molar fraction of oxygen dissolved in the melt NiTi when oxide Y_2O_3 is in equilibrium with it

LIST OF APPENDICES

A Appendix	107
A.1 DSC analysis	107
B Appendix	111
B.1 Curriculum Vitae	111

A APPENDIX

A.1 DSC analysis

Tab. A.1: Enthalpy changes [J/g] associated with martensitic transformation $B2 \leftrightarrow B19'$ in the supplied and the re-molten $Ni_{50.8}Ti_{49.2}$ alloy at 1500 °C with holding time 2, 10 and 20 min, and at 1500 °C and 1450 °C with 20 min of holding time.

supplied alloy				
19.0				
1500 °C/2 min	1500 °C/10 min	1500 °C/20 min	1450 °C/20 min	1550 °C/20 min
18.3	18.6	9.0	11.8	11.5

Tab. A.2: Characteristic phase transformation temperatures [°C] and enthalpy changes [J/g] associated with martensitic transformations in the $Ni_{50.8}Ti_{49.2}$ samples heat treated in Regime I in air, argon and helium.

atmosphere	M_s	M_p	M_f	$\Delta H_{B2 \rightarrow B19'}$	A_s	A_p	A_f	$\Delta H_{B19' \rightarrow B2}$
air	-37	-49	-64	16.3	-33	-22	-12	-17.6
argon	-34	-47	-63	15.8	-35	-22	-11	-18.0
helium	-37	-54	-72	15.3	-39	-26	-14	-17.5

Tab. A.3: Characteristic phase transformation temperatures [$^{\circ}\text{C}$] and enthalpy changes [J/g] associated with martensitic transformations in the $\text{Ni}_{50.8}\text{Ti}_{49.2}$ samples heat treated in Regime II in air, argon and helium.

atmosphere	R_s	R_p	R_f	M_{s1}	M_{p1}	M_{f1}	M_{s2}	M_{p2}	M_{f2}	$\Delta H_{B2 \rightarrow B19'}$
air	32	26	20	6	-8	-30	38	-50	-59	21.1
argon	31	24	19	-42	-60	-72	-	-	-	14.0
helium	33	25	18	-49	-72	-85	-	-	-	12.8

atmosphere	A_s	A_{p1}	A_{p2}	A_f	$\Delta H_{B19' \rightarrow B2}$
air	20	31	34	39	-20.5
argon	17	23	32	37	-19.6
helium	14	20	33	39	-19.0

Tab. A.4: Characteristic phase transformation temperatures [$^{\circ}\text{C}$] and enthalpy changes [J/g] associated with martensitic transformations in the $\text{Ni}_{50.8}\text{Ti}_{49.2}$ samples heat treated in Regime I in oxygen, nitrogen, hydrogen, argon and helium.

atmosphere	M_s	M_p	M_f	$\Delta H_{B2 \rightarrow B19'}$	A_s	A_p	A_f	$\Delta H_{B19' \rightarrow B2}$
oxygen	-39	-52	-69	15.7	-38	-26	-17	-17.9
nitrogen	-36	-53	-71	15.1	-39	-26	-13	-18.2
hydrogen	-36	-	-	6.6	-48	-33	-3	-14.5
argon	-34	-47	-63	15.8	-35	-22	-11	-18.0
helium	-37	-54	-72	15.3	-39	-26	-14	-17.5

(-) unable to evaluate

Tab. A.5: Characteristic phase transformation temperatures [$^{\circ}\text{C}$] and enthalpy changes [J/g] associated with martensitic transformations in the $\text{Ni}_{50.8}\text{Ti}_{49.2}$ samples heat treated in Regime I in reference helium atmosphere, hydrogen-helium mixtures (H_2 partial pressure 20, 100, 500 and 700 mbar) and pure hydrogen.

atmosphere	M_s	M_p	M_f	$\Delta H_{B2 \rightarrow B19'}$	A_s	A_p	A_f	$\Delta H_{B19' \rightarrow B2}$
helium	-37	-54	-72	15.3	-39	-26	-14	-17.5
20 mbar	-47	-65	-82	15.0	-39	-25	-9	-14.7
100 mbar	-	-80	-97	8.6	-45	-30	-2	-14.7
300 mbar	-	-	-111	7.4	-49	-34	-11	-12.6
500 mbar	-	-	-	5.7	-50	-34	8	-14.9
700 mbar	-	-	-	6.5	-19	-34	-7	-13.1
hydrogen	-36	-	-	5.0	-48	-33	-3	-13.7

Tab. A.6: Characteristic phase transformation temperatures [$^{\circ}\text{C}$] and enthalpy changes [J/g] associated with martensitic transformation in the $\text{Ni}_{50.8}\text{Ti}_{49.2}$ samples heat treated in Regime II in reference helium atmosphere or hydrogen-helium mixtures (H_2 partial pressure 20, 100, 500 and 700 mbar).

atmosphere	R_s	R_p	R_f	$\Delta H_{B2 \rightarrow R}$	M_s	M_p	M_f	$\Delta H_{B2 \rightarrow B19'}$
helium	33	25	18	6.3	-49	-72	-85	6.5
20 mbar	32	25	-	6.4	-	-	-106	18.6
100 mbar	31	23	-	5.9	-	-	-	10.1
300 mbar	32	21	-	5.5	-	-	-	9.7
500 mbar	30	21	-	6.4	-	-	-	8.8
700 mbar	31	21	-	6.8	-	-	-	8.9

atmosphere	A_s	A_{p1}	A_{p2}	A_f	$\Delta H_{B19' \rightarrow B2}$
helium	14	20	33	39	-18.5
20 mbar	14	20	33	40	-17.9
100 mbar	14	21	31	37	-16.2
300 mbar	13	-	30	37	-11.8
500 mbar	13	22	30	35	-13.9
700 mbar	12	23	30	36	-13.5

B APPENDIX

B.1 Curriculum Vitae

Author of this thesis was born on 16th of April, 1985. In 2004 she applied for study at University of Technology in Brno and was admitted. She earned both bachelor's and master's degrees in Chemistry, Technology and Properties of Materials in 2007 and 2009. After graduating with her master's in 2009, she undertook her doctoral studies supervised by Prof. A. Dlouhý at Institute of Physics of Materials of the Academy of Sciences of the Czech Republic in Brno.

Conferences

- International Conference on Metallurgy and Materials METAL 2010, May 18–20. Presentation on An interplay between heat treatment conditions and B2 \leftrightarrow B19' transformation in Ni-Ti shape memory alloys, Rožnov pod Radhoštěm.
- International Conference on Metallurgy and Materials METAL 2011, May 18–20. Presentation on Impact of heat treatment environment on microstructure and transformation path in Ni-Ti shape memory alloys, Brno.
- International Conference on Martensitic Transformations ICOMAT 2011, September 2–9. Poster presented on Impact of hydrogen environment on microstructure and transformation path in a Ni-rich NiTi shape memory alloy, Osaka Japan.
- Proceedings of the International Conference on Shape Memory and Superelastic Technologies SMST 2013, May 12–16. Abstract of Hydrogen Pick-Up During Heat Treatments of Ni-rich NiTi shape memory alloys, Prague.

Short Stays

- Max Planck Institute for Metals Research in Stuttgart, Germany. Department Mittemeijer: Phase Transformation, 2010 June–December. ERASMUS Scientist Training agreement - assisted with local research on martensitic transformation in NiTi alloys under stress as a member of research group led by Dr. Mittemeijer.

Articles

- Kubenova, M., Zalesak, J., Cermak, J. and Dlouhy, A.: An interplay between heat treatment conditions and B2 \leftrightarrow B19' transformation in Ni-Ti shape memory alloys. METAL 2010: 19th International Metallurgy and Materials Conference, 877–882, 2010.

- Kubenova, M., Zalesak, J., Cermak, J. and Dlouhy, A.: Impact of heat treatment environment on microstructure and transformation path in Ni-Ti shape memory alloys. METAL 2011: 20th Anniversary International Metallurgy and Materials Conference, 1004–1009, 2011.
- Zalesak, J., Kubenova, M., Cermak, J. and Dlouhy, A.: Influence of heat treatment on microstructure and transformation characteristics of NiTi shape memory wires. METAL 2011: 20th Anniversary International Metallurgy and Materials Conference, 998–1003, 2011.
- Kubenova, M., Zalesak, J., Cermak, J. and Dlouhy, A.: Impact of hydrogen environment on microstructure and transformation path in a Ni-rich NiTi shape memory alloy. *Journal of Alloys and Compounds* 577, 287–290, Nov 15 2013.